EXPERIMENTAL EVALUATION OF BONE DRILLING USING ULTRASHORT PULSED LASER ABLATION

By:

BRENT J. EMIGH, B.Sc.

A Thesis

Submitted to the School of Graduate Studies

In Partial Fulfillment of the Requirements

for the Degree

Master of Science

McMaster University

MASTER OF SCIENCE (2011) McMaster University

(Medical Physics & Applied Radiation Sciences) Hamilton, ON

TITLE: Experimental evaluation of bone drilling using ultrashort pulsed laser ablation

AUTHOR: Brent J. Emigh, B.Sc. (McMaster University)

SUPERVISORS: Professor Qiyin Fang, Professor Joseph E. Hayward

NUMBER OF PAGES: xiii, 118

ABSTRACT

Mechanical oscillating drills and saws are commonly used in orthopaedic surgery to cut and re-shape bone as well as develop holes for the placement of screws; however, their high tissue removal efficiency also comes with negative side-effects. Friction between oscillating tools and bone can result in significant thermal damage. As well, the precision is limited by the finite blade or bit thickness. Ultrashort pulsed lasers appear well-suited to replace these traditional tools as they have the ability to efficiently remove bone tissue while causing only minimal collateral thermal damage. Laser ablation has additional advantages over mechanical tools, such as: (i) no mechanical vibration; (ii) minimal invasiveness; and (iii) the ability to focus to small spot sizes for precise tissue removal. In this thesis work, we experimentally investigated a few key aspects of ultrashort laser ablation of bone tissue and presented the results as well as conclusions.

First, the laser ablation threshold of unaltered bone tissue was determined using the D^2 technique. The threshold ranged from $1.66\ \mathrm{J/cm^2} \pm 0.87\ \mathrm{J/cm^2}$ to $2.37\ \mathrm{J/cm^2} \pm 0.78\ \mathrm{J/cm^2}$ depending upon the number of incident pulses. The reduction in ablation threshold with incident pulse number was an indication of the damage accumulation effect referred to as incubation. Using a power law model, the incubation coefficient, ζ, was measured to be 0.89 ± 0.03.

Specific laser parameters (pulse energy, pulse duration) and drilling protocols (scanning speed, beam focus position) were characterized. In an intra-species comparison, the removal rate (depth of removed tissue per pulse) was observed to be substantially larger in chicken bone compared to that in pigs. For ultrashort pulses (≤ 10 ps), the removal rate was found to be inversely related to the pulse duration; however, irradiation with 5 and 10 ps pulses were also shown to result in significant tissue removal. With a pulse repetition rate of 1 kHz, the removal rate was observed to be highest when ablating with 50-100 pulses per spot along the channel. A proof-of-concept investigation of oscillator-only bone ablation produced no discernable tissue removal.

The ability of ultrashort pulsed lasers to remove larger volumes (>1 mm^3) of bone tissue was examined by experimenting with different laser scanning procedures. A series of 40 concentric circles ablated in the surface of bone produced a structure ~2.4 mm deep; however, ablated side-lobes were present at oblique angles to the incident beam. A two-layer structure was machined by scanning concentric circles at two different beam focus planes separated by 150 μm and produced a ~2.2 mm deep cylindrical-structure without side-lobes. As a comparison, concentric circle scanning was also evaluated in trabecular bone samples. While it was possible to remove significant amounts of trabecular bone tissue, the ablative precision was less than that observed in cortical bone. To speed up machining times, helical drilling was attempted but did not produce discernable tissue removal under micro-CT. The laser parameters (pulse energy, duration, repetition rate, etc.) of the ultrafast laser system were adjusted to simulate the beam output of a typical Nd:YAG laser and cylinder drilling was performed. The ablated craters had maximum depths of ~0.15 mm deep, significantly less than those achieved using typical Ti:Sapphire beam parameters, largely due to the reduced amount of pulse overlap. The ability to drill large-scale holes using low average pulse energies and optimized laser scanning procedures will alleviate the stringent requirements for optical components in clinical practice.

ACKNOWLEDGMENTS

It would be only natural to first thank my supervisors, Dr. Qiyin Fang and Dr. Joseph Hayward. Their guidance, support, and friendship made my journey through graduate school not only successful but also a lot of fun. I was truly lucky to have such fantastic supervisors.

I would also like to thank Dr. Harold Haugen and the members of his laser lab, Eugene Hsu and Dr. Ran An, for their assistance from Day One of this project. Without them, I’d likely still be trying to figure out how to turn the laser on.

Dr. Greg Wohl provided insight on the physiological aspects of this project and was an invaluable resource for me, especially in the early stages. I also appreciate the patience and accommodation shown by his lab members, Cheryl Druchok and Aaron Muizelaar, who I had to bother anytime I needed to use the bone saw. A big ‘thank-you’ goes to Dr. Julius Pekar for all of his help with the micro-CT and to Rebecca Thorpe for her help during the revision process.

I want to thank my friends for being there for me; especially during these last few hectic months where I had become more often than not ‘No-Fun-Brent’. All of you have shaped me more than you know.

Lastly, I’d like to especially thank my parents, David and Kathy, and my sister, Hilary. My family has made a lot of sacrifices to allow me the opportunity to follow my dreams. They gave me the support I needed when work and life were at their heaviest and I can’t tell them enough how I much I appreciate it.

LIST OF FIGURES

LIST OF SYMBOLS AND ABBREVIATIONS

CW – continuous-wave
CPA - chirped pulse-amplifier
MEG – magnetoencephalography
MRI – magnetic resonance imaging
BMD – bone mineral density
μ_a – absorption coefficient
μ_s – scattering coefficient
μ_t – total attenuation coefficient
δ – optical penetration depth
Nd:YAG – neodymium:yttrium-aluminum-garnet
Er:YAG – erbium:yttrium-aluminum-garnet
Ti:Sapphire – Titanium:Sapphire
Nd:YLF - neodyminum:yttrium-lithium-fluoride
PDT – photo-dynamic therapy
Er:YSGG – erbium:yttrium-scandium-gallium-garnet
τ_r – thermal relaxation time
Ca – calcium
P – phosphorus
ν – frequency of longitudinal mode
L – laser cavity length
OD – optical density
CCD – charged-coupled device
τ – optical delay time
PBS – pellicle beam-splitter
H&E - hematoxylin and eosin
CT – computed tomography
OCT – optical coherence tomography
SEM – scanning electron microscopy
BK7 – type of high quality optical class
w_0 – laser beam radius ($1/e^2$)
D – diameter of ablated crater
ϕ – fluence (J/cm^2)
ϕ_{th} – ablation threshold fluence (J/cm^2)
ζ – incubation coefficient
HWP – half-wave plate
Nscan – incident pulse number per spot lying on scanned ablation line
f – objective lens focal length

1. INTRODUCTION

1.1. Introduction to laser hard tissue ablation

Lasers produce collimated, coherent and monochromatic light that allows precise and selective interactions with biological tissue [1]. At sufficient optical energy densities, material can be removed from the irradiated surface – referred to as laser ablation. The use of lasers for surface ablation has the added benefits of non-contact intervention and results in only minimal mechanical vibration within the target material.

The potential of lasers as biological and clinical tools has been explored since the invention of the first functional laser in 1960 [2]. In 1963, Campbell *et al.* [3] reported the first human patients treated for retinal tears with ruby laser photocoagulation. The first investigations of hard biological tissue ablation were in the field of dentistry [4, 5]. In the 1980s, experimental studies were conducted to test the capability of lasers for use in arthroscopic procedures [6-8], for the removal of herniated discs (discectomy) [9], and for the treatment of otosclerosis [10]. However, there has been a significant delay between the invention of the laser and its successful clinical application. Vogel and Venugopalan [11] have attributed this lag to a lack of understanding of the fundamental laser-tissue interactions at play during laser ablation. Many of the early hard tissue ablation modalities use collimated, continuous-wave (CW) or long-pulsed lasers in the infrared region. Their clinical applications were limited by the extent of tissue carbonization and fracturing produced adjacent to the irradiated regions [12-14].

Micromachining research has suggested that the ablation process depends principally on the laser irradiance instead of pulse energy [15]. High irradiances can be created from low average energy pulses when laser beams are focused to small spot sizes or when the energy is delivered in a very short time frame. With the invention of mode-locking and the subsequent improvements in pulse amplification, pulse durations of picoseconds or less – referred to as ultrashort laser pulses – can be achieved [16]. Ultrashort pulses are characterized by a high peak irradiance that usually leads to non-linear interactions in various materials. The extremely short pulse duration allows energy to be deposited into the material faster than thermal diffusion rate, therefore reducing the likelihood of thermal energy accumulation. As well, the non-linear interactions between ultrashort pulses and material tend to provide clean structural features after material removal [17].

As a result of their ablation capabilities, ultrashort pulsed lasers have shown potential in replacing mechanical cutting tools in orthopaedic and dental surgery. This thesis presents the results of an experimental evaluation of specific laser parameters and protocols for hard tissue laser ablation and their effect on the efficiency and accuracy of tissue removal.

1.2. Thesis outline

Chapter 2 of this thesis presents the background information for this project including the history of hard tissue laser ablation and the specific mechanisms involved. An in-depth look at the structure and composition of bone is also presented as well as how that structure ultimately influences the laser ablation process. Chapter 3 covers the experimental methods used in this study; specifically, the ultrafast laser micromachining system configuration, the specific bone samples used, and the various characterization techniques. Chapters 4, 5 and 6 provide the experimental results from three distinct areas of research. In Chapter 4, the ablation threshold of porcine cortical bone was determined at different incident pulse numbers. The change in threshold fluence with pulse number indicated that an incubation effect was present. The incubation coefficient for porcine cortical bone was also determined. Chapter 5 contains the characterization results of various ablation parameters, such as: pulse energy, pulse duration, and scanning speed. Chapter 6 covers the experimental results from large-scale tissue removal procedures. The protocols used in the experiments covered in this chapter were designed to result in tissue removal on the millimeter scale. Lastly, a summary of main study findings will be presented in the Conclusions section along with a re-iteration of the clinical significance of this work.

2. BACKGROUND

This chapter provides background information related to this thesis. The first part of this chapter discusses contemporary surgical procedures that utilize mechanical tools for cutting and drilling hard biological tissue. The complications associated with mechanical cutting tools are discussed which provides the motivation for this work. Following the clinical significance, an in-depth look at the macro- and microscopic structure of bone are presented. The hierarchical structure of cortical and trabecular bone as well as their composition are discussed in relation to the mechanical competence of tissue. The history and physical mechanisms of hard tissue laser ablation are presented in the second part of this chapter. The processes and dynamics of ablation using ultrashort laser pulses will be discussed in depth. Lastly, the specific goals of this project are presented along with some proposed future directions for this specific field of research.

2.1. Cutting/drilling in orthopaedic and dental surgery

2.1.1. Procedures

Mechanical saws and burr drills are used in a large variety of orthopaedic and dental procedures. Osteoid osteomas and osteoblastomas are benign lesions of the bone and often present with intense pain [18]. A common surgical removal technique (burr-down technique) uses a high-speed rotary drill to sweep across the reactive zone until the hypervascular nidus is encountered. After removing the nidus tissue with a curette, the surrounding sclerotic tissue is removed and the edges smoothed with the drill [19].

Burr drills are also used to help create pilot-holes into which pedicle screws are placed during spinal stabilization procedures. Pedicle screw fixation is used specifically to achieve solid bone fusion in patients suffering from scoliosis, fracture of the spine, spondylodiscistis, or tumours in the spine. The pedicle screws provide a means of gripping a spinal segment and acts as a firm anchor point that can be connected with an external rod (Fig. 1) [20, 21]. Traditionally, high-speed burr drills have been used to create the entry point for pedicle screw pilot holes, traversing through the cortical shell into the cancellous bone within the pedicle [22] while the remainder of the hole is created with a pedicle probe or an awl. For cases of screw insertion into vertebrae of the cervical spine, burr drills are have been used to develop the entire length of the pilot hole [23, 24].

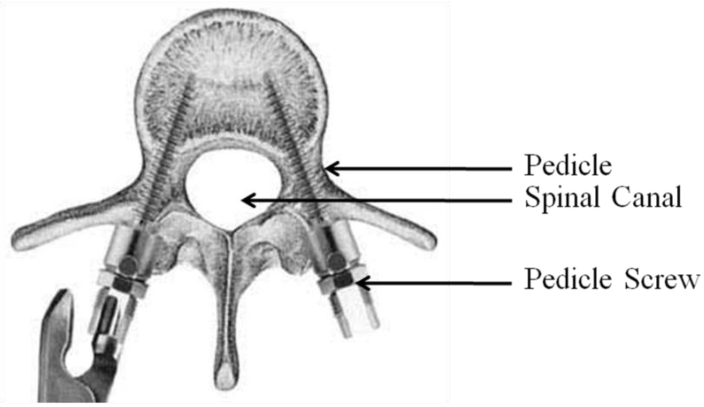

Fig. 1: Transverse cut-away of human vertebral bone with two pedicle screws inserted. Note the close proximity of the placed-screws (within the pedicles) to the spinal canal. Screws are typically 35-50 mm in length and 5-7 mm wide

Mechanical drills are used in a variety of other surgical procedures. Relatively large dime-sized holes are drilled in the skull to lessen inter-cranial pressure due to haemorrhaging following a severe subdural hematoma [25], while smaller (2-6 mm) drills are used during middle ear and mastoid microsurgery [26, 27]. In dentistry, burr drills are commonly used to remove dental caries.

Mechanical saws are used in numerous orthopaedic procedures, osteotomies and knee joint replacements for example. While the main benefit of mechanical bone saws is their high tissue removal rate, their precision is limited by the finite blade thickness (>0.25 mm) [28], which restricts their use to bone excision in regions with relatively large tissue margins.

2.1.2. Complications with mechanical saws/drills

The frequent use of mechanical drills and saws in surgical procedures is largely due to their efficiency; however, despite improvements in technology, many complications still arise from their use. The more complicated the anatomical location, the greater the risk of peripheral tissue damage, especially if there are adjacent neural or vascular structures.

The most obvious drawback to mechanical cutting tools is the heat resulting from the friction between tool and tissue surfaces. A previous investigation of the heat generation during a traditional osteotomy showed temperature rises of 15°C to 21°C (depending on initial bone temperature) at a distance of 1 mm from the cut line [29]. Localized increases in heat can result in tissue damage in the form of protein structural changes and alterations in enzyme activity [30]. Specifically, bone necrosis can occur at temperatures greater than 47°C after an exposure time of 1 minute [31, 32]. Visible thermal damage such as tissue carbonization and cracking has been observed following the use of mechanical cutting tools [33]. Thermal damage can lead to infection and other post-operative complications, such as those seen by Christie [34]; four patients treated for fractures of the tibia with stabilizing pins developed infections in the carbonized necrotic tissue surrounding the drilled pilot-hole. As well, the infection resulted in substantial bone weakening and all four patients suffered subsequent local fractures.

Mechanical saws and drills require contact between the device and the tissue. As a result, the performance of the surgical instrument is dependent on the condition of the cutting surface. Damage to the teeth of a saw-blade can affect the cleanliness of the cut, increase the necessary cutting force (and heat production), and also increase the likelihood of metal shavings being produced and deposited within the operated region [35, 36]. Along with having a negative influence on the subsequent healing processes, these metal shavings can distort post-operative diagnostic investigations i.e. magnetoencephalography (MEG) or magnetic resonance imaging (MRI) [37]. Initial contact between a rotary mechanical drill and smooth bone surfaces also tends to result in drill-bit wander [38] – sliding and misaligning of the bit – which likely contributes to the relatively high frequency of misplaced pedicle screws. Previous studies have found an incidence of 13-16% for ill-placed screws [39, 40].

Lastly, due to their inherent mechanical nature, oscillating saws and drills can result in significant vibrations in the surrounding target tissue [41, 42]. Thin and fragile bones such as segments of the maxilla and mandible are prone to fracture during traditional osteotomies in oral surgery because of the vibrations caused by mechanical instruments [36]. Vibrations in tissue can also result in pain and discomfort to the patient [41, 43] and, in more serious cases, the vibrations resulting from conventional high-speed cutting tools have resulted in severe haemorrhaging [44].

2.2. Bone histology

Bone fulfills three major functions in the body: mechanical support, protection of soft tissues and supply of blood cells and various minerals. Bone is both resilient and hard; its resilience due to the organic matter in its composition and the hardness due to inorganic materials. Bone tissue is a type of dense connective tissue and comes in a variety of shapes with a complex internal and external structure, both on the macroscopic and microscopic level. Several properties of bone are relevant to pulsed laser ablation. Tissue composition and morphology establish tissue optical properties and determine the internal optical energy distribution while structure and mechanical properties mediate the thermo-mechanical response of bone to laser irradiation.

2.2.1. Macroscopic structure

Bone in human and mammalian bodies can be generally classified into two types: cortical bone, also known as compact bone, and trabecular bone, also known as cancellous or spongy bone. Cortical bone contributes about 80% of the total skeletal mass within the human body while trabecular bone contributes the other 20% [45]. These two types are classified on the basis of porosity and unit microstructure. Cortical bone is much denser than trabecular bone with a porosity ranging between 5% and 10% compared to 50%-90% for trabecular bone [45]. As a result of this increased porosity, trabecular bone has significantly larger surface area in the body compared to cortical bone.

As its name implies, cortical bone tissue forms the cortex (outer shell) of most bones. Owing to its porosity, cortical tissue gives bone its smooth, white and solid outer appearance and is much harder and stronger than trabecular bone. Located within the interior of bones, trabecular bone exists in a reticular structure consisting of irregularly-shaped sheets and spikes of bone (trabeculae). This network is highly vascular and frequently contains red bone marrow where hematopoiesis – the production of blood cells – occurs. Cortical and trabecular bone are found in specific locations. In long bones, such as the femur, most of the shaft thickness is made of cortical bone with a small amount of trabecular bone within the marrow cavity. The ends of long bones, however, consist largely of trabecular bone covered with a thin shell of compact bone [46]. Trabecular bone is also found within the vertebral body in the spinal column.

Trabecular and cortical bone tissue are biologically identical [47] and their compositions can be broken down into two categories: organic and inorganic. It is the interplay between these two sub-groups that give bone its characteristic strength and brittleness while also having a significant degree of elasticity. The organic phase consists mainly of collagen (20% of total bone mass) and other proteins (1-2%). The inorganic phase is responsible for the hardness of bone and consists of a complex structure of crystalline hydroxyapatite ($Ca_{10}(PO_4)_6(OH)_2$) (50% of bone mass), water (15-20%), carbonates (5%) and phosphates (1%) [15].

2.2.2. Microscopic structure

As with all biological tissues, bone is extremely hierarchical in nature [48, 49]. Both cortical and trabecular bone contain many different structures that exist on multiple levels of scale. The first unit of structure in cortical bone is the osteon while the basic first level of structure in trabecular bone is the trabeculae.

Osteons make up the first level structure of cortical bone. Osteons, also known as Haversian systems, consist of blood vessels surrounded by concentric rings of bone tissue and are typically several millimetres long and up to 0.5 mm in diameter [47]. The layers of tissue surrounding each Haversian canal are referred to as lamellae. Within each lamellae, collagen fibres are predominantly parallel to one another; however, the orientation of these fibres can change up to 90° in adjacent lamellae [50]. Histologically, the variable collagen fibre orientations will cause different layers of bone to contrast with one another under polarized light.

A histological structural organization of cortical bone is shown in Fig. 2. Woven, or non-lamellar bone, is a type of cortical bone that does not contain osteons. Instead, woven bone consists of loose and disorganized collagen fibres, is mechanically weak (compared to lamellar bone) and is often found in adolescent skeletons (<5 years) or in adult skeletons following trauma or disease.

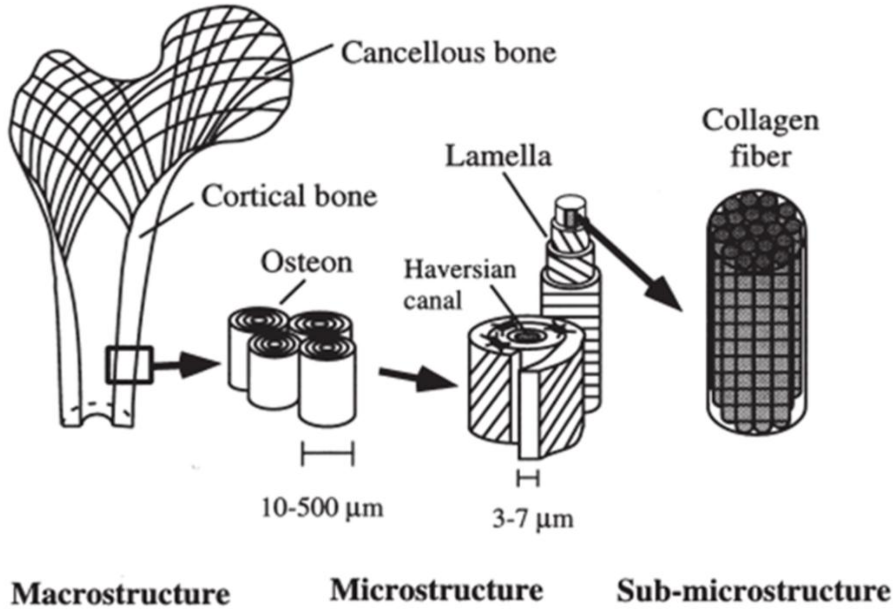

Fig. 2: Hierarchical structural organization of cortical bone showing the osteon sub-unit complete with Haversian canals and lamella on the micro scale, as well as collagen fibers on the sub-micro scale [32]

Unlike osteons, the basic structural unit of trabecular bone (trabeculae) does not have a central canal with a blood vessel. Trabeculae are most often characterized as having a rod- or plate-like structure and are generally no greater than 200 μm in thickness and about 1 mm long. At a second structural level, trabecular bone consists of the same entities as cortical bone such as lamellae;

however, in trabecular bone, lamellae are not arranged concentrically as in cortical bone but rather longitudinally along the length of the trabeculae [51].

The mechanical competence of bone is largely determined by its microstructure and intrinsic material properties, such as bone mineral density (BMD), cortical porosity, and size and distribution of mineral crystals. During everyday activity, bone has to withstand both compressive and tensile stresses as well as bending and torsional moments. The varied orientation of the collagen fibrils between adjacent lamellae make bone resistant to strains resulting from bending. The mineral constituent in bone resists compression forces effectively; however, it has a relatively poor ability to withstand tensile loads [52]. The specific collagen and mineral orientation in individual lamella results in bone tissue having a stiffness that varies with direction i.e. an anisotropic nature [53]. BMD refers to the amount of mineral content per cubic centimeter of bone and serves as a direct measure of an individual’s fracture risk – a decreased BMD results in an increased fracture risk [54]. The porosity of cortical bone also has a significant effect on its mechanical competence. An increased porosity reduces the available area for the propagation of microcracks [55] – short splits in cortical bone resulting from the disruption of intermolecular bonds – resulting in a decreased resistance to fracturing. Microcracks occur through everyday activities, are regularly found throughout the skeleton at load-bearing sites and have been shown to negatively affect the stiffness and strength of bone tissue [56]. Lastly, the mechanical properties of bone tissue depend on the size and distribution of mineral crystals [57]. The size of individual crystals can increase through the accumulation of free ions and by aggregation, referred to as 'secondary nucleation'. As the number of large crystals increases, bone becomes more brittle and is prone to fracturing [52].

Throughout an individual's life, the skeleton continuously remodels itself; mature bone tissue is removed (resorption) and new bone tissue is formed (ossification). The purposes of this turnover are to: regulate calcium homeostasis in the body, repair microcracks and shape the skeleton during growth. The cells responsible for bone metabolism are the osteoclasts, which break bone down, and osteoblasts which secrete new bone. The actions of both cell types are governed by complex signalling pathways which include the actions of several hormones, such as calcitonin, parathyroid hormone and growth hormone [58].

As an individual ages, the osteoblast activity decreases and the rate of bone regrowth slows. Each osteonal remodelling event fails to replace all of the bone previously removed and results in an increase in cortical bone porosity, decrease in BMD, and an accumulation of microcracks. As well, the collagen network experiences up to a 50% loss in its capability to absorb energy likely due to an increase in the percentage of denatured collagen [59], which also results in the increased formation of microcracks. Energy absorption, fracture toughness and ultimate tensile strain show age-related changes of about 5-10% per decade [60].

2.3. Laser ablation of hard tissues

Laser ablation, in its broadest sense, is the removal of material from a surface using laser irradiation. The process of laser ablation is a complex interplay of optical interactions, thermal and mechanical transients and ablation plume dynamics. Laser ablation is currently used for a variety of material processing applications involving metals and semiconductors; however, the knowledge gained from these technical applications cannot be directly transferred to living composite biological materials. Bone tissue, in particular, combines properties such as high mechanical strength and inhomogeneous nature which are useful for the living being but unfavourable for laser machining [61]. As well, bone cells can be irreparably damaged by thermal energy produced during laser-tissue interactions.

2.3.1. Previous work

Since laser ablation of the tooth was first reported in 1964 [4], various types of continuous-wave (CW) (CO_2, Nd:YAG, Argon) and pulsed (Er:YAG, excimer, CO_2) lasers have been considered for the removal of dental tissue [62-64]. The first attempted use of laser ablation in orthopaedic surgery was reported in 1973 [65]. Early investigations that followed fixated on the healing properties of bone in response to laser-induced damage [66-69]. With advances in laser technology, thermal damage to tissues was reduced and by the 1990s, investigators were experimenting with specific laser parameters (i.e. wavelength, pulse duration) and protocols (i.e. with/without water flushing) to find optimal tissue removal rates [43, 70-73]. Previous investigations with specific lasers will be presented in Section 2.3.3 when discussing the individual ablation mechanisms.

2.3.2. Laser-hard tissue interactions

The spatial distribution of volumetric energy density generated by laser irradiation drives all laser ablation processes [11]. This distribution is controlled by the incident radiation exposure and a variety of laser-tissue interactions, such as: reflection and refraction at the interface, absorption and scattering. The degree to which each interaction affects the energy distribution is primarily dependent on the type of material and the incident wavelength [15].

Reflection is defined as the change in direction of electromagnetic radiation at an interface so that the radiation returns into the medium from which it originated. Depending on the nature of the interface, reflection can be either specular (directions of the incident and reflected ray make the same angle with respect to the surface normal) or diffuse (reflected at many angles). Specular reflection tends to occur when light reflects off a smooth surface, with surface irregularities being small compared to the wavelength of radiation. In contrast, diffuse reflection occurs when the roughness of the reflecting surface is comparable to or larger than the wavelength of light. Diffuse reflectance is a common phenomenon of all biological tissues. Examples of specular and diffuse reflection are shown in Fig. 3.

Also included in Fig. 3 is an example of a liquid coating over a rough surface which results in a reduction of diffusively-reflected light.

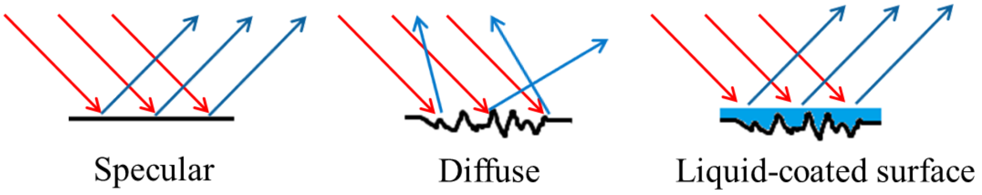

Fig. 3: Specular and diffuse reflection off smooth and rough surfaces. A liquid-coating on a rough surface acts as the reflection surface and can reduce the occurrence of diffuse reflected light

When a photon of light is absorbed by a molecule it can raise that molecule to an excited state. There are a number of mechanisms through which an excited molecule can decay back to its ground state such as the emission of a photon or through de-excitation processes such as molecular vibrations which results in thermal energy. The ability of a medium to absorb electromagnetic radiation depends on a number of factors: the electron constitution of its atoms and molecules, the wavelength of incident light, the thickness of the absorbing layer and various internal parameters, such as temperature [15]. In biological tissues, absorption is mainly caused by water molecules or macromolecules such as proteins. In bone, the main absorbers are water (strong absorption peaks at 2.94 and 6.1 μm) [74] and collagen fibrils (peaks at 6.0, 6.5, and 7.9 μm) [75]. The calcium and phosphate apatite in bone mineral also have a variety of minor absorption peaks from 3.1 to 11.1 μm [76-78].

The third significant laser-tissue interaction is scattering, where the initial direction of a photon changes due to the interaction with a scattering object. Elastic scattering occurs when light is scattered without a change in the incident photon energy. Inelastic scattering involves a transfer of energy between the translational mode of the photon and the rotational and vibrational modes of the scattering particle. A special type of elastic scattering called Rayleigh scattering occurs when the scattering particles are smaller than the wavelength of the incident light. The amount of light that is Rayleigh scattered is proportional to λ^{-4} [15]; therefore, longer wavelengths are able to penetrate deeper into materials before being scattered.

The likelihood of a photon being absorbed or scattered as it traverses a medium is described by the absorption and scattering coefficients, μ_a and μ_s respectively. The sum of the absorption and scattering coefficients is called the total attenuation coefficient, μ_t. The intensity, I, of a collimated beam within a medium will exponentially decrease with distance as:

$$I = I_o e^{-\mu_t d} \tag{1}$$

where I_o is the initial intensity and d is the distance travelled. The inverse of μ_t is referred to as the optical penetration length, δ, which describes the depth at which the intensity has decayed to $1/e$ of its initial value [79]. At wavelengths ranging from 674 to 849 nm, the absorption and scattering coefficients of bone are 0.5 cm^{-1} ± 0.2 cm^{-1} and 9 cm^{-1} ± 1 cm^{-1}, respectively [80]. From these values, the optical penetration depth can be calculated to be approximately 105 μm.

The optical parameters of biological tissue (i.e. scattering and absorption coefficients) can change significantly during laser exposure [81, 82]. Tissue carbonization, in particular, leads to increased absorption. The change in local temperature during ablation can also change the tissue absorption and scattering [15]. For example, the absorption peak of water at λ = 2.94 μm shifts towards shorter wavelengths as temperature increases due to the weakening of hydrogen bonds between adjacent water molecules [83]. It should also be noted that tissue preparation (sectioning, drying, freezing, soaking in saline, etc.) can also have a significant influence on optical properties [84]. As a result of these possible alterations, caution needs to be taken when transferring experimental findings and conclusions determined *in vitro* to *in vivo* applications.

2.3.3. Ablation mechanisms

Laser systems can be classified as continuous-wave (CW) or pulsed. Whereas most gas lasers and some solid-state lasers belong to the first group, the family of pulsed lasers includes solid-state, excimer, and certain dye lasers. The duration of exposure primarily characterizes the type of interaction with biological tissue [15]; therefore, the interactions between CW and longer-pulsed lasers are distinctly different from those that occur when using shorter laser pulses.

The most common interaction mechanisms for therapeutic and surgical applications can be divided into five broad classes: photochemical interactions, thermal interactions, photo-ablation, plasma-induced ablation and photodisruption. It has been shown that all of these interaction types can be achieved with energy densities between 1 and 1000 J/cm^2 – a relatively small range compared to the 15 orders of magnitude of potential pulse durations [15]. A map of the five specific laser-tissue interactions is shown in Fig. 4. It should be noted that even though they appear to be distinctly separated in Fig. 4, interaction types can overlap. For example, thermal effects may also play an important role in photochemical interactions. Ultrashort pulses ($\leq$10 ps [85]) – each of them having no thermal effect – may add up to a measurable increase in temperature if applied at sufficiently high repetition rates. Thermal and plasma-mediated ablation have shown the most promise for hard tissue ablation so these two mechanisms will be discussed separately later in this section.

Photochemical interactions occur at very low power densities ($\leq$1 W/cm^2) and long exposure times (seconds to CW). At this irradiance, absorbing molecules in the target material can become excited and are more likely to undergo chemical reactions. The excited molecules can also undergo bond-breaking, leading to an ablative photochemical decomposition [86]. Material is ablated above a certain threshold irradiance that provides a bond dissociation rate that exceeds the recombination rate [87]. The photochemical mechanism is utilized primarily for therapeutic applications such as photo-dynamic therapy (PDT) or bio-stimulation and has little usefulness for hard biological tissue ablation.

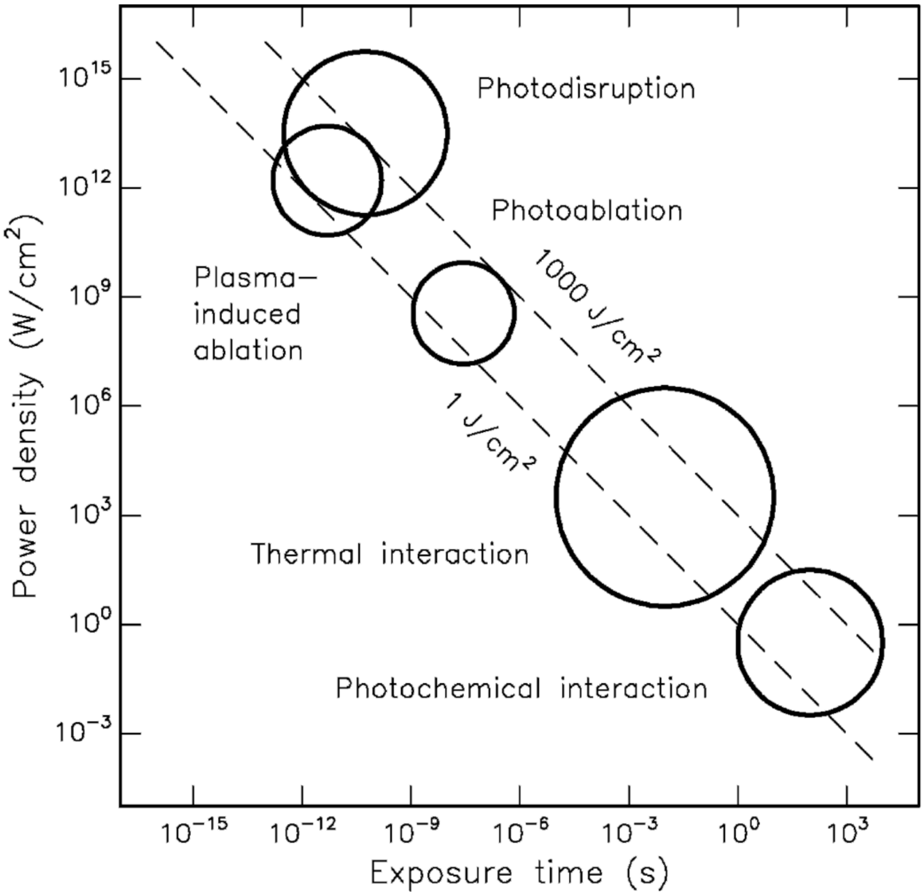

Fig. 4: Map of five specific laser-tissue interactions. The circles represent the approximate power densities and exposure times at which the interaction mechanism is observed. The 1 J/cm^2 and 1000 J/cm^2 energy density lines are included to show the characteristic energy density range in which all five laser-tissue interactions can occur. Reprinted with permission from [15]

Thermal interactions consist of a large sub-group of interaction types where the increase in local temperature is the significant parameter change in the tissue. Thermal interactions can be induced by CW or pulsed laser radiation. Due to the versatility and efficiency of thermally-mediated ablation, investigations with hard biological tissues have been underway since the 1970s [69, 88-91]. An extensive review of thermal interactions is given in section 2.3.3.1.

At power densities greater than that for thermal-interactions (10^7 – 10^{10} W/cm^2), tissue is removed in a very clean and exact ‘etching’ manner – the result of an ablation mechanism referred to as photoablation [15]. First identified by Srinivasan & Mayne-Banton in 1982 [92], photoablation describes the decomposition of target material as a result of high intensity laser irradiation. At sufficient power densities, molecular sub-units that are originally held together by strong intra-molecular attractive forces are broken apart and ejected from the material surface, resulting in the precise removal of tissue with only minimum alteration to the surrounding unaffected tissue [93, 94]. High photon energies are required in order to disassociate these bonds; therefore, photoablation typically requires the use of ultra-violet (UV) light from excimer lasers [95-97]. Due to the cytotoxicity of UV radiation and the risk of mutagenic effects within cells, photoablation is not a feasible mechanism for biological hard tissue ablation.

At sufficiently high power densities ($>10^{10}$ W/cm^2) [15], a phenomenon called optical breakdown occurs and plasma is generated. This plasma can undergo rapid expansion, resulting in shockwaves propagating into the target material and removal – referred to as plasma-mediated ablation. An extensive discussion of the complex interactions involved in plasma-mediated ablation is presented in Section 2.3.3.2.

Lastly, at power densities significantly greater than the optical breakdown threshold (10^{11} – 10^{16} W/cm^2) [15], target materials can undergo a secondary effect of higher plasma energies called photodisruption. During photodisruption, the target material is split by mechanical forces by shockwaves and cavitation similar to plasma-mediated ablation. However, unlike plasma-mediated ablation which is limited to the breakdown region, photodisruption involves the propagation of mechanical effects into adjacent target material and the removal of tissue at a distance from the interaction zone. This propagation can lead to uncontrolled and imprecise tissue removal, making photodisruption an unappealing ablation mechanism for use with hard biological tissue.

2.3.3.1. Thermal effects

Temperature is the governing parameter of all thermal laser-interactions. The basic origins of thermally-mediated ablation are: heat generation, heat transport, heat effects and tissue damage.

Heat generation is regulated by the laser and tissue optical parameters. As discussed previously, hard biological tissue primarily consists of water, collagen proteins, and crystalline minerals, each with their own specific absorption spectra. To generate thermal energy within tissue, the wavelength of incident light must be preferentially absorbed by a tissue constituent. As a result, lasers typically used for thermally-mediated ablation are specifically chosen or tuned to coincide with high absorption peaks i.e. the family of erbium-doped lasers is preferentially absorbed by water (Er:YAG at 2.94 μm, Er:YLF at 2.8 μm, and Er:YSGG at 2.79 μm). At the microscopic level, thermal effects have their origin in bulk absorption followed by non-radiative decay: absorption of a photon promotes a molecule to the excited state, inelastic collisions with molecules in the surrounding medium leads to a deactivation of the excited molecule and a simultaneous increase in kinetic energy (and temperature) of the surrounding medium.

The transport of heat within biological hard tissue is governed by its thermal tissue properties such as heat capacity and thermal relaxation time. The local temperature rise at the irradiated location is directly related to the local volumetric energy density and the specific heat capacity [11]. Once the energy is absorbed, it is subject to spatial redistribution by thermal diffusion. The thermal relaxation time, τ_r, of a heated region of tissue is the time required for the local peak temperature to decrease to 37% of the total rise and is a common measure of a material's thermal susceptibility [98]. For laser pulse durations less than τ_r, thermal energy does not diffuse to the distance given by the optical penetration depth and, as a result, thermal damage to the surrounding tissue is negligible. For pulse durations greater than τ_r, heat can diffuse beyond the optical penetration depth and thermal damage to adjacent tissue is possible. Previous solutions for the thermal relaxation time of water at different absorbing wavelengths found the shortest τ_r to be approximately 1 μs [99]; therefore, it can be presumed that laser pulse durations shorter than 1 μs are not associated with collateral thermal damage. A high repetition rate of the laser pulses can also evoke an additional increase in temperature if the rate of heat transport is less than the rate of heat generation [100]. At low repetition rates, the energy deposited by each laser pulse diffuses out of the focal volume before the next pulse arrives and the irradiated region can return to a moderate temperature before the next pulse arrives. Consequently, the structural changes and removed material as a result of the thermal interactions are confined to the focal volume, regardless of the number of incident pulses. At high repetition rates, the energy from successive pulses accumulates in and around the focal volume, producing structural changes at distal locations [101]. An example of this 'thermal build-up' effect caused by high repetition rates is shown in Fig. 5.

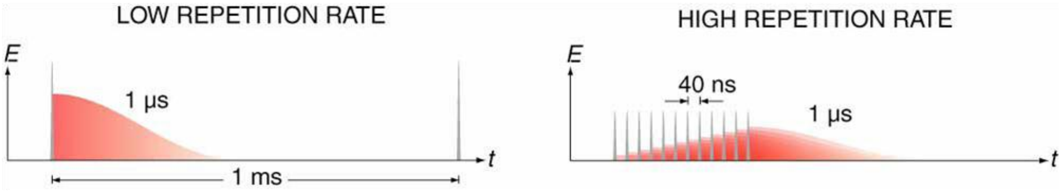

Fig. 5: Deposited energy accumulation as the result of high repetition rates (right) compared to low repetition rates (left) for fused silica. Grey: laser pulses; red: deposited energy. Reprinted with permission from [101].

The specific heat effects in biological hard tissue are determined by the peak temperature achieved and duration of time for which the high temperature was sustained. The structural effects of heat can be vapourization, carbonization or melting. In tissue, vapourization of water leads to rapid increases in pressure and micro-explosions resulting in the ejection of material. Vapourization also creates recoil momentum which then forces out liquid material in a secondary ejection [43]. The thermo-mechanical removal of tissue through explosive vapourization has been a prominent method for hard tissue laser ablation and has been shown to produce efficient tissue removal [37, 69, 102-104]. Carbonization is another specific tissue effect that can occur as temperatures exceed 100°C and after all of the water within the tissue has been vapourized. Lastly, melting of hydroxyapatite can occur as temperatures reach a few hundred degrees (°C). Melting and resolidification can result in fractures and gas bubbles [15].

As mentioned previously, past studies of thermally-mediated laser ablation of hard biological tissue resulted in relatively high removal rates; however, due to the longer pulse durations and multiple absorption bands by different tissue constituents [28], most experimental results have suffered collateral damage due to the lack of thermal and stress confinement. Er:YAG (λ=2.94 μm) lasers have been suggested for use in orthopaedic and dental procedures [105]; however, their use has been shown to result in tissue charring [37, 91, 102, 106-108]. The change in temperature has also been shown to cause changes to the relative calcium (Ca) and phosphorus (P) levels in the adjacent tissue and the stress propagation can cause micro-cracks (Fig. 6); both which would result in delayed tissue healing [109]. CO_2 (λ=10.6 μm) lasers targeting the bone mineral have also been shown to result in severe tissue charring and fracturing [106, 110, 111]. Recently, efforts have been made to reduce the extent of thermal damage through the use of water-cooling with promising results [73, 104]; however, since bone tissue can be denatured at temperatures much lower than is necessary for carbonization [31, 32], the lack of tissue charring does not eliminate the possibility of thermal damage.

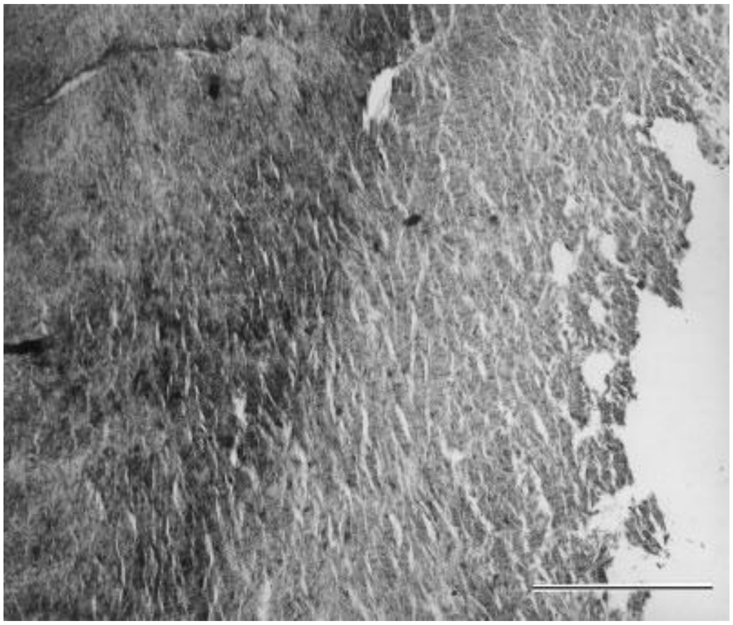

Fig. 6: Transmission electron microscopy (TEM) image of parietal bone of Wistar rats tissue following Er:YAG irradiation. Micro-cracks were caused by stress propagations caused by the explosive vapourization ablation mechanism. (Scale bar = 5 µm). Reprinted with permission from [109].

2.3.3.2. Plasma-mediated ablation

Biological tissue can generally be considered to be a wide band-gap dielectric material [43]; therefore, if able to absorb sufficient energy, its' bound electrons can be excited into their quasi-free state. With extremely high laser power densities (>10^{11} W/cm^2), photons are simultaneously absorbed by bound electrons and excited into the conduction band – a phenomenon referred to as multiphoton ionization. In water, the number of simultaneous photons needed to cross the band gap with a wavelength of 800 nm is five and the process occurs on a time scale of a few femtoseconds [11].

Once in their free state, these electrons act as the "seeds" for the avalanche ionization process. These seed electrons can absorb incoming photons and accelerate – in the presence of an atom, this process is referred to as inverse bremsstrahlung [11]. Free electrons continue to gain kinetic energy until the electron exceeds the band gap energy and can then produce another free electron as a result of a collision (impact ionization). The result is now two free electrons that can then be accelerated. This recurring process of accelerating and impact ionization results in the accumulation of free electrons and ions. A schematic of these two processes: multiphoton ionization and avalanche ionization is shown in Fig 7. At sufficiently high free electron densities (>10^{21} electrons/cm^2), dielectric breakdown occurs and a dense, hot surface plasma forms [112].

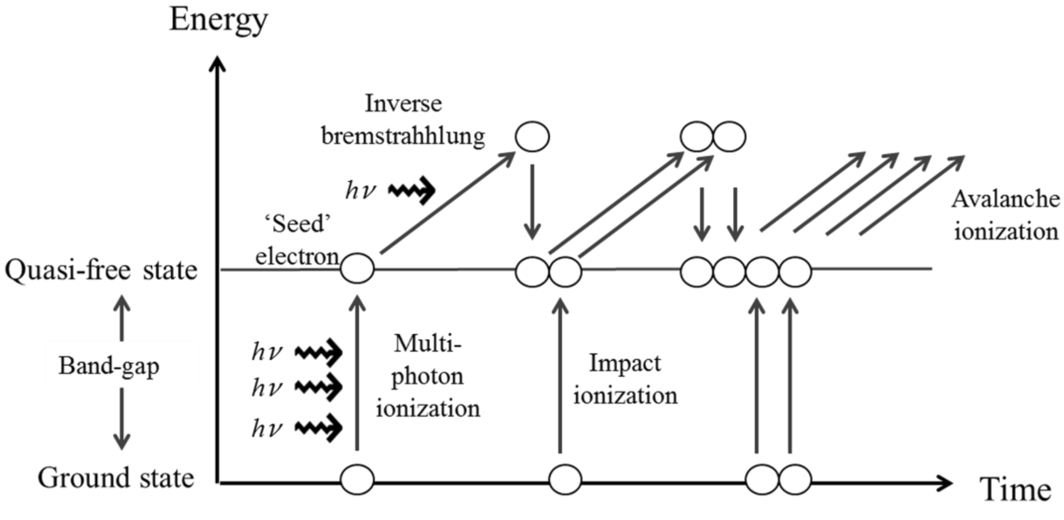

Fig 7: Multiphoton ionization of bound electrons to quasi-free state. Avalanche ionization consists of inverse Bremsstrahlung absorption and impact ionization which eventually produces a highly dense free electron cloud (plasma)

At this point, the volumetric plasma energy density is extremely high, with temperatures of several thousand Kelvin at threshold radiant exposures [113]. As a result of this extreme energy, the plasma undergoes rapid and explosive expansion that results in shockwave emission, cavitation bubble formation, and jet formation upon bubble collapse [11, 114]. The transfer of laser to mechanical energy for plasma-mediated ablation is extremely efficient; a previous study by Vogel *et al.* in bulk water found that the transduction of laser energy to mechanical energy was as high as 90% -- more than for any other laser-tissue interaction [113, 115]. Along with the hydrodynamic expansion of the plasma plume and its subsequent shockwaves, ablation is also caused by thermal degradation due to the extremely high temperatures within the plasma [11]. Collateral mechanical effects are much less severe when the plasma is produced on the tissue surface as opposed to within tissue where the plasma expansion is mechanically confined [116].

As discussed, laser-induced optical breakdown starts with multiphoton absorption, which has a strong nonlinear dependence on laser intensity [115, 117]. The multiphoton ionization rate is proportional to I^k, where I is the laser irradiance and k is the number of photons required for ionization [11] and, as a result, there is a sharp delineation in the plasma plume boundary as you move spatially from the center of a Gaussian-shaped laser beam to the periphery. This non-linearity results in the highly-localized deposition of energy during plasma-mediated ablation which allows for very concise and well-defined tissue removal. The volume in which energy deposition occurs can also be easily controlled by focusing the laser radiation. Due to the mechanism of optical breakdown and the increased absorption coefficient resultant from the high density of free electrons in plasma capable of absorbing laser photons, plasma-mediated ablation can even be used for biological tissues that are normally transparent or weakly absorbing [11, 15, 118].

While plasma-mediated ablation has been shown to produce highly efficient ablation in biological hard tissues [28, 43, 44, 119-123], the increased absorption coefficient of the induced plasma can act as a shield for succeeding laser photons [15] – a phenomenon referred to as plasma shielding. As a result, the ablation efficiency tends to decrease over time as photons are absorbed by the dense electrons and ions in plasma. In a previous study by Siegel *et al.* using surface reflectivity, the peak surface plasma density was observed ~1.5 ps following the pump pulse [112]. This would presumably correspond to the point in time at which plasma shielding would be most significant.

2.4. Ultrashort pulsed lasers

Ultrashort laser pulses are generally considered to be pulses with durations shorter than the thermal vibration period of molecules (around tens of picoseconds (10^{-12} s)) [85]. As a result of this extremely short pulse duration, an ultrashort laser pulse can achieve very high instantaneous power while sustaining a low overall average power. As a result, non-linear absorption and optical breakdown can occur even with a low thermal load [124]. As well, ultrashort laser pulses can deposit energy into material faster than the electron-phonon interaction time and thermal energy diffusion rate, and are therefore able to efficiently ablate without resulting in a significant temperature rise in the surrounding tissue [15].

2.4.1. Generation of ultrashort laser pulses

With the first lasers, the overall pulse durations were largely determined by the lifetime of the excited state of the laser transition. With the invention of Q-switching in 1962 by McClung & Hellwarth [125], a mechanical or optical device could be placed within a laser cavity to act as a variable attenuator, resulting in significantly shorter pulse durations (>50 ns) and higher peak energies. For the specific case of solid-state lasers, two milestones in the development of ultrashort laser pulses were reached with the invention of the mode-locking technique [126] and the development of novel laser media with extremely large bandwidths.

Mode-locking occurs within the laser cavity and begins with the formation of standing waves in the cavity; all satisfying the relationship:

$$\nu = \frac{nc}{2L} \tag{2}$$

where L is the cavity length, and n is an integer ($n \geq 1$). Any frequency, ν, that satisfies this relationship will oscillate independently within the cavity (referred to as a longitudinal mode) while all other frequencies of light are suppressed by destructive interference. With many modes (>1000), their interference leads to a near constant output intensity (CW operation). However, if a constant phase difference is introduced between modes, they will periodically constructively interfere – forming an intense pulse of short duration. This phase relationship can be implemented using active or passive mode-locking. Active mode-locking uses an external signal to induce modulation of the intra-cavity light, and can be accomplished using a mechanical shutter tuned to the cavity round-trip time or electro-optic crystals which can up-shift or down-shift the frequency of the passing CW light. Passive mode-locking uses an element placed within the laser cavity to cause self-modulation of light. A commonly used passive mode-locking device is a Kerr-lens – which focuses high- and low-intensity light differently – to selectively amplify the high-intensity pulses as they pass through an aperture [17].

The greater the number of interfering modes, the shorter the duration of the high-intensity pulse after mode-locking. Therefore, laser media with wide optical bandwidths are needed to create ultrashort mode-locked pulses. Bulky dye lasers with large emission bandwidths were first used in the 1970s to obtain pulses as short as a few hundreds of femtoseconds (10^{-15} s) timescale [127, 128]. In the 1980s, dye lasers could be used to generate pulses with durations below 10 femtoseconds [129]; however, the field of ultrashort pulsed laser ablation didn't take off until the invention of the Ti:Sapphire Kerr-lens mode-locked laser [130, 131]. The large Kerr effect and broad emission bandwidth of the Ti:Sapphire laser and diode-pumped solid-state lasers [132] greatly simplified the set-up needed to generate ultrashort pulses and promptly replaced the traditional dye lasers.

2.4.2. Current usages and advantages

Laser pulse widths greater than 1 nanosecond are longer in duration than both the electron cooling time (≈1 ps) and the lattice heating time (>>1 ps). As a result, electron-absorbed laser energy has enough time to transfer to the lattice which then reaches thermal equilibrium or results in material removal via thermal ablation [133, 134]. However, when ultrashort pulses are used, excited electrons transfer their energy to the positive lattice ions in approximately 1 ps. If the energy intensity is high enough, the bonds of the lattice structure break without having time to transfer their energy to neighbouring lattice ions. A direct solid-vapour and plasma transition occurs with negligible heat conduction in the target material [133].

For pulses on the nanosecond scale or shorter, as the pulse duration decreases, so does the optical breakdown threshold in biological tissues [116, 135]. The extremely high peak intensities of ultrashort pulses induce plasma generation, even though the average pulse energy is still relatively low. In the femtosecond regime, the threshold for plasma generation is so low that photo-disruptive effects, such as those caused by mechanical shockwaves, can be avoided [136].

Lastly, the use of ultrashort laser pulses minimizes the negative effects of plasma shielding as the laser pulse is too short to allow the formation of a plasma plume during irradiation. In contrast to longer pulses, the impact of the ultrashort pulse energy on the sample has ceased before the breakdown of the gas above the sample. As a result, no laser energy is directly dissipated in the plasma [114].

As a result of their cutting mechanism, minimal thermal and mechanical collateral damage and insignificant plasma-shielding, ultrashort pulsed lasers have been previously used for investigations into biological hard tissue ablation [28, 43, 44, 119-122, 137-141]. Previous studies have found minimal thermally-induced modifications in bone [43, 119, 138] following ultrashort laser ablation and a particular histological study showed significantly reduced temperatures in adjacent bone when using femtosecond pulses compared to nanosecond pulses [28]. Photo-acoustic and mechanical stresses during ultrashort pulse ablation of bone have been examined using piezoelectric fluoropolymer film transducers and found to be negligible [140]. Femtosecond pulses have also been shown to maintain the relative contents of P and Ca in bone at the ablation site – an attribute crucial for surgical applications because a change in P/Ca ratio can lead to a localized change in pH which results in delayed tissue healing [138, 142].

2.5. Thesis objectives

The long-term objective of this project is to perform image-guided laser bone drilling with the assistance of an integrated robotic system. In order to accomplish this, a number of multidisciplinary research tasks will need to be addressed: an investigation of issues related to the integration of a laser end-effector with robotic control systems, the development of real-time imaging, sensing, and feedback modalities, and an investigation of bone ablation laser parameters and protocols.

With appropriate positioning and positional feedback, a robotic control system will have significantly higher positional accuracy compared to a laser irradiation tool held manually by an operator. The control system will have both autonomous (relying on image-registration) and master/slave approaches (operator haptic feedback) for the laser end-effector.

Real-time imaging, sensing and feedback modalities will allow the drilling process to rapidly adjust to changing conditions. Patient motion (i.e. respiratory) is one of the most important sources of errors in any image-guided interventions and could be compensated for with the use of accelerometer sensors. Optical sensors, coupled with feedback mechanisms, could also be used to detect changes in the drilling path (i.e. pedicle cortical breach) or to correct for bone inhomogeneities.

The tasks addressed specifically in this thesis involve the bone ablation laser parameters and protocols. Using a bench-top testing platform, the ablation threshold of unaltered bone was first investigated in order to find the irradiance requirements for future applications using *in vivo* samples. Secondly, a characterization of specific drilling parameters was performed to investigate their effect on the ablation of hard tissue. Once the range of capabilities of the various laser parameters have been established, the knowledge can be used to devise strategies to control ablative precision, optimize drilling efficiency and minimize thermal and mechanical injury. The final objective of this thesis is the investigation of large-scale ablation scanning procedures. It is generally difficult to produce large diameter (≥1 mm) holes using laser ablation. Using a large laser spot size will require extremely high pulse energies in order to have the fluence throughout the focused spot above the ablation threshold. Therefore, a high power laser system will be required which poses significant problems with respect to cost, light delivery through fibres, and safety to users. Much lower fluences are needed if the spot size is kept small and scanning procedures are used instead to create larger-diameter holes. The ability to drill large-scale holes using low average pulse energies will alleviate the stringent requirements for the optical components.

3. METHODS

This chapter will primarily cover the general experimental set-up used for the various investigations outlined in the remainder of this thesis. Specific laser parameters and ablation protocols unique to each study will be presented with their respective results in the Chapters 4, 5 and 6. Common to all studies was the ultrashort laser setup; therefore, the different components of the laser system will be discussed along with the specific beam diagnostic procedures performed before each ablation procedure. The bone sample preparation will also be discussed, along with the closed drilling vials in which all ablation procedures took place. Lastly, four different characterization methods used to analyze ablated samples will be discussed: histology, reflected-light microscopy, micro-computed tomography (micro-CT) and hand-held digital microscopy.

3.1. Laser system

The ultrafast laser system is operated by the group of Dr. Harold Haugen at McMaster University. The following sub-section provides an overview of the laser system and a description of the specific beam diagnostic procedures.

3.1.1. Typical experimental set-up

All ablation experiments presented in this thesis were performed using a customized ultrafast laser machining system; the schematic of which is shown in

Fig. 8. A continuous-wave, frequency-doubled neodymium doped yttrium orthvanadate (Nd:YVO_4) laser (Millenia V, Spectra Physics) with a wavelength of 532 nm was used to pump a Titanium:Sapphire mode-locked oscillator laser (Tsunami, Spectra Physics). The Tsunami oscillator produced 90 fs pulses [full-width half-maximum (FWHM)] at a rate of 82 MHz (corresponding to the oscillator cavity round-trip time). The oscillator had a stable output of ~780 mW; therefore, the individual pulse energy was found to be ~9.5 nJ. Ti:Sapphire crystals have a peak absorption between 400 and 600 nm and an emission band centered around 800 nm. The emitted pulses have a FWHM bandwidth of ~10 nm. The output of the oscillator was used as seed pulses in a Ti:Sapphire chirped-pulse amplifier (CPA) (Spitfire, Spectra Physics), which was pumped by a 527 nm, frequency-doubled diode-pumped Nd:yttrium-lithium-fluoride (Nd:YLF) laser source (Evolution X, Spectra Physics) operating at 1 kHz.

Within the CPA, the incoming pulse was first “stretched” in time by creating a temporal offset of the spectrum (a “chirp”) through the use of dispersive optics. The stretched pulses were then amplified in a regenerative amplifier and subsequently recompressed through a compressor to generate amplified pulses at the output. After exiting the amplifier, the pulses were typically ~180 fs in duration with energies of ~325 μJ. The central wavelength was 800 nm and the repetition rate was 1 kHz. The beam from the CPA was initially ~10 mm in diameter and was immediately reduced in size by a beam condenser, constructed from an f = 50 cm achromatic doublet and an f = -20 cm plano-concave singlet lens, to a diameter of ~4 mm. Reducing the beam size eliminated the likelihood of clipping the beam on spinning wave plates or other small-aperture optical equipment. The beam had a near-Gaussian intensity profile (example profile shown in Section 3.1.2.3.

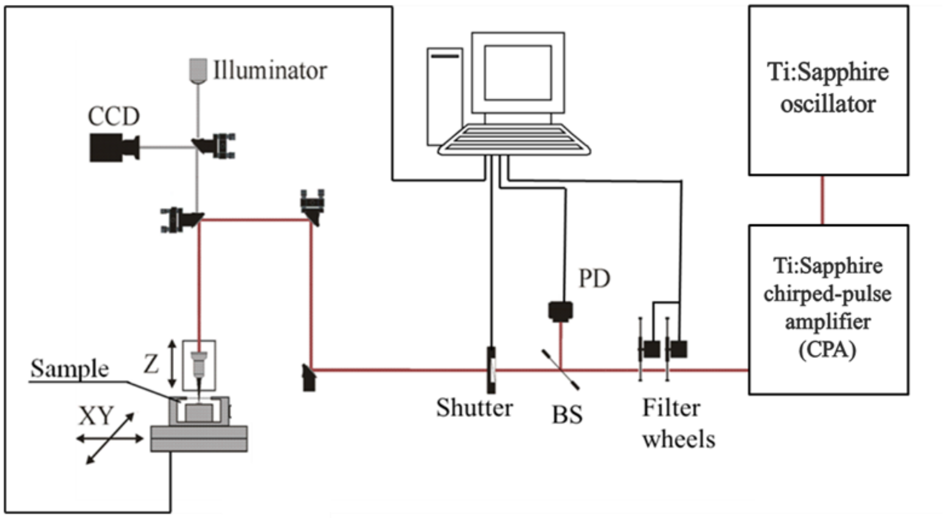

Fig. 8: Simplified schematic of the ultrafast laser system. After exiting the oscillator, the laser pulses were stretched, amplified, and compressed in the chirped-pulse amplifier. The beam energy was adjusted using two computer-controlled filter wheels. A beam-splitter (BS) picking off a portion of the beam and directed it onto a calibrated photo-diode (PD). The computer-controlled mechanical shutter was used to vary the sample exposure time. A CCD camera and illuminator monitored the ablation process to ensure laser-sample alignment.

The pulse energy was lowered from its maximum of ~325 μJ using both a zero order half wave plate (0RP44-3, Newport) and a thin film polarizer (11B00UP.26, Newport), and then directed into a set of 1 mm thick, reflective, neutral density filters (Model 5249, New Focus) mounted in computerized filter wheel houses. With different optical densities (OD) in each filter, the combination of two filter wheels allowed pulse energies to be adjusted in OD steps of 0.1 (OD = log (I/I_0) where I is the laser intensity) by the computer during drilling experiments. The laser exposure time (i.e. number of pulses delivered to the sample) was adjusted with a computer-controlled mechanical shutter (VS25S2S1, Uniblitz). The shutter required more than 1 ms to switch from fully open to closed; therefore, a mechanical chopper (not shown in Fig. 8) was used if a precise number of incident pulses was required.

The beam was then directed into the focusing optic, consisting of a plano-convex lens (f = 125 mm, BK7), which focused the collimated beam down to a $1/e^2$ spot size radius, w_0, of 15.1 μm. Assuming Gaussian beam propagation (Fig. 9), the confocal parameter, b, for an 800 nm beam was calculated to be 1.8 mm. The confocal parameter, also referred to as the depth of focus, is the distance along the propagation direction of a beam between the two points in which the cross-sectional area of the beam is twice that at the beam waist ($2w_0$). The focusing objective was mounted on a Z translation stage (M-MFN25PP, Newport) that was used to adjust the Z-position of the laser focal point.

For ablation experiments, bone samples were placed within a custom-machined, steel drilling chamber which was mounted on a computer-controlled X-Y translational stage (UTM100PP.1, Newport). During ultrafast laser irradiation, plasma electrons can penetrate into the solid target material because of the charge separation potential and produce x-rays via K-shell ionization and bremsstrahlung [143]. Additional metal shielding (1/4” thick copper) was placed around the micromachining chamber to attenuate any x-rays that may have leaked out of the primary chamber. A hand-held Geiger counter was used to monitor x-ray production. A confocal monochrome charged-couple device (CCD) camera and white LED illuminator were used to monitor the machining process and the sample alignment during the course of the experiments.

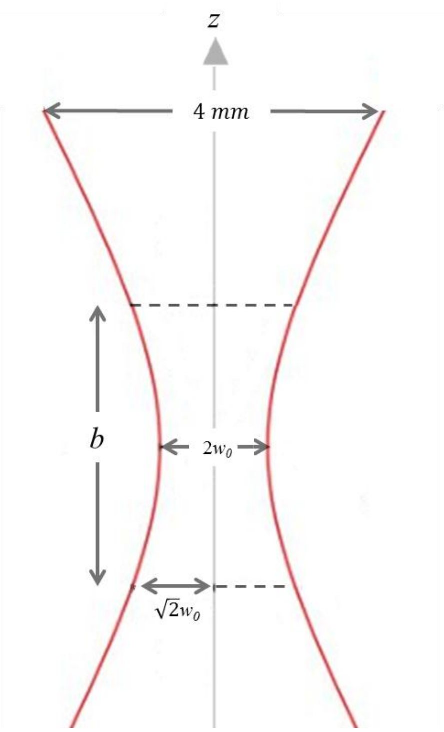

Fig. 9: Gaussian beam propagation in free space. The beam diameter before focusing was 4 mm. The minimum spot diameter, or beam waist ($2w_0$), was calculated to be 30.2 µm. The distance between the two points of the beam where the area of the cross-section is twice that of the beam waist is referred to as the confocal parameter, *b*.

3.1.2. Beam diagnostic procedures

To prevent any damage to optical instruments, such as the beam profiler or spectrometer, minimal laser powers are used whenever possible during beam diagnostic procedures. This was most easily accomplished by ejecting a late pulse out of the CPA.

3.1.2.1. Pulse duration

The pulse duration was measured prior to each drilling experiment with the use of a second-order non-collinear autocorrelator. Based on a Michelson interferometer configuration (Fig. 10), pulses were divided into two separate paths through the use of a beam-splitter, one path of which included an adjustable optical delay, τ, created by a mirror on a motorized translational stage. The two beams were then superimposed and focused on a nonlinear frequency-doubling BBO crystal. The intensity of the frequency-doubled photons, which is a function of the amount of "overlap" of the two pulses, was recorded using a photodetector. By adjusting the optical delay line, one pulse is effectively "shifted" through the other and the pulse duration can eventually be deduced. In experiments that required a variety of pulse durations, the autocorrelation procedure was performed after each adjustment of the CPA compressors.

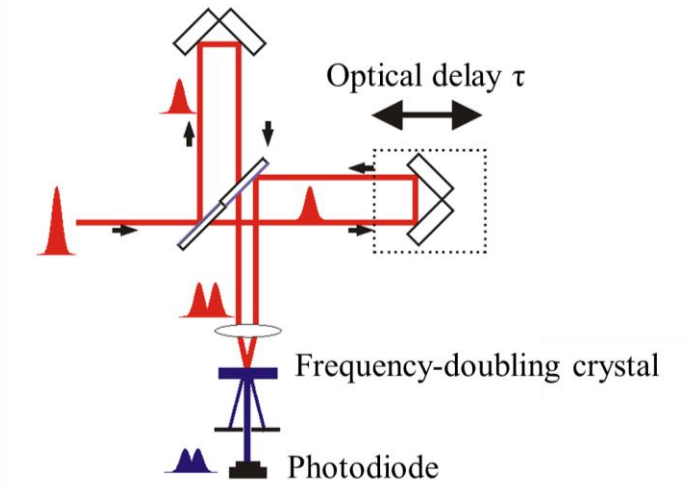

Fig. 10: Schematic of intensity autocorrelator geometry based on a Michelson interferometry configuration. The input beam was split into two replicas by a broadband 3 mm thick beam-splitter. One beam passed through an arm with an adjustable optical delay line. The two parallel beams were directed onto a focusing lens which focused the beams onto a non-linear frequency-doubling crystal. The signal from the photodetector was acquired with a box-car integrator (SR250, SRS).

3.1.2.2. Peak wavelength

Before the seed pulses entered the CPA, the peak wavelength of the laser beam was measured using a fibre-coupled spectrometer (PC200, Ocean Optics). A lens tissue was placed in front of the optical fibre input to scatter light onto the fibre for measurement.

3.1.2.3. Beam profile

The beam profile has approximately a Gaussian intensity distribution and was verified using a silicon CCD beam profiler (Beamstar, Ophir Optronics) during the beam alignment process. To ensure alignment, the CCD profiler was placed behind each aperture and a circular beam profile concentric with each alignment iris served as an indication of a suitable configuration. An example of a beam profile measured prior to an ablation procedure is shown in Fig. 11. Note the presence of minor fluctuations and irregularities in both the overall beam profile, as well as the vertical and horizontal profiles, which was likely due to the presence of dust on the optics or the result of damaged optical elements.

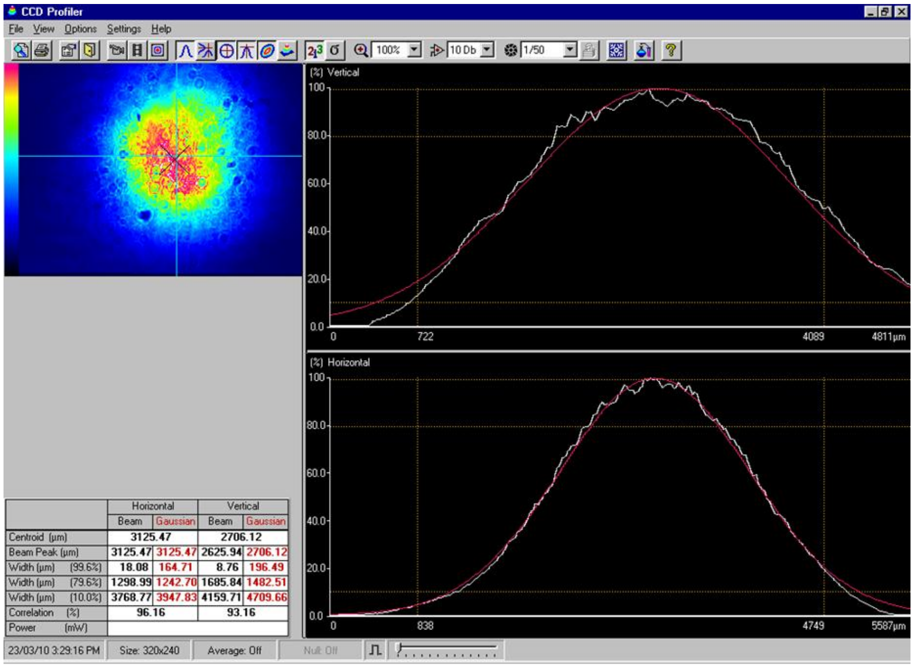

	Horizontal		Vertical	
	Beam	Gaussian	Beam	Gaussian
Centroid (µm)	3125.47		2706.12	
Beam Peak (µm)	3125.47	3125.47	2625.94	2706.12
Width (µm) (99.6%)	18.08	164.71	8.76	196.49
Width (µm) (79.6%)	1298.99	1242.70	1685.84	1482.51
Width (µm) (10.0%)	3768.77	3947.83	4159.71	4709.66
Correlation (%)	96.16		93.16	
Power (mW)				

Fig. 11: Example of beam profile measured using CCD beam profiler prior to the experiments conducted in Section 5.2 of this thesis. (Upper left) Overall beam profile showing a near circular beam shape with some evidence of dust or debris. (Right) Line traces of the actual beam intensity in the vertical (top) and horizontal (bottom) directions, overlaid with a theoretical Gaussian curve (red line).

3.1.2.4. Power calibration

Power calibration was performed as the last step of the beam diagnostic procedures, after the pulse-width, spectrum, beam profile measurements and optical alignment had been performed. After passing through the neutral density filters, a small portion of the laser beam was reflected onto a photodiode (DET210, Thorlabs) using a pellicle beam-splitter (PBS). To calibrate the photodiode, an optical powermeter was placed in the beam path after the focusing objective to measure the laser power after passing through all the optical instrumentation. The powermeter was placed as close to the objective lens as possible to capture the entire beam well before it comes into focus to prevent permanent damage to the detector as a result of high intensities. Bone samples were drilled in a sealed vial with a quartz viewing window; therefore, a chamber window was placed on the powermeter to account for Fresnel losses as the beam passed through. After calibrating the photodiode with the powermeter, the powermeter was removed and the laser power incident on the bone surface could be determined from the photodiode reading.

3.1.2.5. Laser-sample surface alignment

To align the laser beam focal plane with the sample surface for drilling experiments, a calibration was first performed using a piece of silicon. The laser was used to ablate a flat region on the surface of the silicon. The telescopic lens of the collinear CCD camera was then adjusted until the ablated surface on the camera display appeared in sharp focus. At this point, the laser focusing plane was aligned with the CCD imaging plane and the laser could be presumed to be focused on the bone surface when the camera display showed the surface in sharp focus. When using the 125 mm focusing lens, there exists a 200 μm range in which the sharpness of the silicon surface appeared to remain at a maximum. Assuming Gaussian beam propagation, a translational uncertainty of 200 μm in locating the laser focus on the sample in the viewing camera and a $1/e^2$ spot size diameter of 30.2 μm, a theoretical beam waist deviation of up to 0.74 μm could result. This variability in the beam waist would subsequently give rise to uncertainty in the fluence.

3.2. Bone samples

3.2.1. Specimens

The use of food-grade animal tissue was approved by the McMaster Animal Research Ethics Board. Bone samples were harvested from skeletally immature pigs obtained from a local butcher in Hamilton, Ontario. Samples were obtained primarily from rib, vertebral, or scapular bones. In cases where samples were required from different pigs, bone was obtained from three different local grocers. For an intra-species comparison (discussed in Section 5.2), bone samples were obtained from the humerus of food-grade chickens.

3.2.2. Preparation and work-up

After harvesting, the attached soft tissue and periosteum were removed from the surface of the bones using tweezers and individual drilling samples were cut from the bone using a handsaw. Samples were obtained from locations in the bone that had relatively flat surfaces. Typical bone samples were approximately 1 cm in length and width and approximately ½ cm in height. Samples were cut to include both the outer cortical layer (thicknesses 1-3 mm) as well as cancellous bone (~5 mm). The bottom surface of each bone surface was smoothed using 60-grit sandpaper to ensure flatness. The drilling surface of each bone sample was left unaltered to mimic real-life conditions.

After sectioning, the bone samples were stored in the freezer and labelled with their date of harvest and anatomical location. Samples were removed from the freezer and allowed to thaw in the fridge for approximately 12 hours prior to drilling experiments. Moisture on the bone surface was gently removed using Kimwipes® before each drilling trial. Following ablation, all samples were fixed in 10% formalin and stored in saline pending further characterizations.

3.3. Drilling vials

In the ultrafast laser lab, a vacuum system and filter are used to remove airborne particulates produced during the micromachining of materials. However, to prevent a build-up of biological residue in the lines of the evacuation system or fume hood, all bone samples were ablated within sealed drilling vials. The vials were constructed from 63 mm tall glass containers with flat bottoms and plastic lids. A side- and top-view of one drilled sample within a vial is shown in Fig. 12. A ~20 mm diameter hole was made in the plastic lid and a 25 mm circular quartz cover glass slide (0.13-0.17 mm thick) was used to cover the hole and act as a window for the laser. The tallest-possible containers were used to construct the drilling vials in order to maximize the distance between the viewing window and bone surface and prevent the laser from ablating the quartz slide. The slide was attached to the container and sealed using a commercially-available transparent epoxy adhesive. Samples were attached to the bottom of the drilling vial using paraffin wax. After the completion of drilling, the vials were opened in a fume hood to remove the bone sample and the chambers were then discarded.

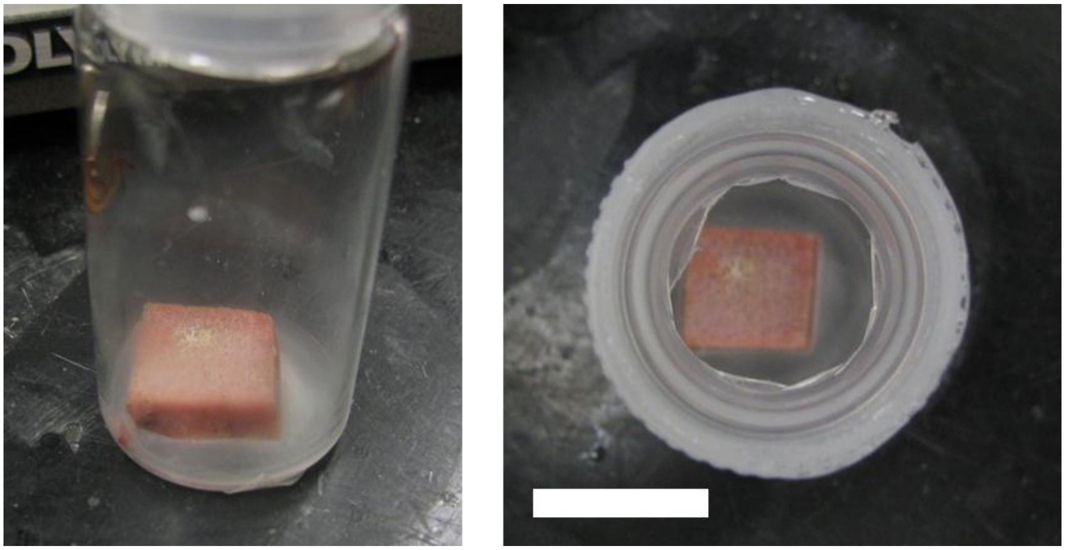

Fig. 12: Side- (left) and top-view (right) images of a sealed drilling vial, with a bone sample within, following an ablation experiment. The laser beam was directed onto the surface of the cortical layer through the viewing window on top of the chamber. The bone sample was held in place with paraffin wax. The vial is attached to the stage using double-sided tape. (Scale bar width is 10 mm)

3.4. Characterization methods

A variety of different techniques were used to characterize the results of the ablation experiments presented in this thesis. This sub-section briefly describes the four primary techniques that were used.

3.4.1. Histology

To examine ablation depths and removal rates, linearly-scanned ablation was used in order to create channels in the surface of bone samples. These samples were then cut cross-sectional to the channels using a slow-rotation, diamond-blade precision sectioning saw (IsoMet, Buehler). The sawblade was a continuous rim diamond wafering blade with a thickness of 0.3 mm. During sectioning, ethanol was used to cool the blade. Using the built-in micrometer, slices were cut with thicknesses ranging from 600 to 750 μm. Histological slices less than 600 μm thick would tear during the cutting process. Slices were mounted on microscope slides and covered with cover slip glass. Histological slides were imaged using a wide-field deconvolution microscope (DMI 6000B, Leica) in the McMaster Biophotonics Facility. The microscope was operated without the use of the deconvolution mode.

To further reduce the incidence of tearing, some ablation samples were embedded in methyl methacrylate before being sectioned. This embedding process consisted of sample dehydration with the use of ethanol and embedment with methyl methacrylate, dibutyl phthalate and benzoyl peroxide. The entire embedding process (dehydration, curing) required 11 days to complete.

While not utilized in the work presented in this thesis, hematoxylin and eosin (H&E) stain and toluidine blue have both been used to detect laser-induced defects in ablated bone [69, 109, 144]. Staining for alkaline phosphatase and intracellular enzymatic activity have also been previously performed on laser-ablated bone samples [28]. Alkaline phosphatase is a membrane-bound protein present on the surface of osteoblasts and can be used as a marker of heat deposition since it denatures around 55° C [145]. Fast Blue (Sigma-Aldrich) was used to determine alkaline phosphatase activity and has a fluorescence excitation/emission spectrum at 360 nm/420 nm, respectively. Calcein AM and ethidium homodimer stains were used to detect the incidence of cellular membrane and nuclear membrane degradation, respectively [28].

3.4.2. Reflected-light microscopy

Spot ablation experiments could not be thin-sectioned due to the small size of the individual surface craters; therefore, a reflected-light microscope (Axioplan 2, Zeiss) in the Canadian Centre for Electron Microscopy at McMaster University was used to examine the surfaces of intact bone samples. Surface structures, such as crater diameters, were measured and analyzed using image analysis software (Northern Eclipse™).

3.4.3. Micro-CT

Large-scale ablation procedures were imaged using an in-house cone-beam computed tomography (CT) scanner optimized for small animal imaging. The bench-top micro-CT is based on a large area flat panel x-ray detector coupled with a gadolinium oxysulfide scintillator, a microfocus x-ray source, and a high precision rotation stage. The flat panel x-ray detector includes a 2D photodiode array with a detection area of 98.6 mm × 49.2 mm and contains 1024 × 2048 pixels, corresponding to a 48 μm pixel pitch. The data acquisition mode used was a “step and shoot” method, where the rotation stage was kept stationary during irradiation and was rotated between projections. Image reconstruction was handled by commercially available reconstruction software

(COBRA, Exxim Computing Corp.). A sample image of a sagittally-cut porcine vertebra scanned in the micro-CT is shown in Fig. 13 to demonstrate the imaging capabilities of the system. 3D volume rendering was performed using the non-proprietary software 3D Slicer^{TM} (www.slicer.org).

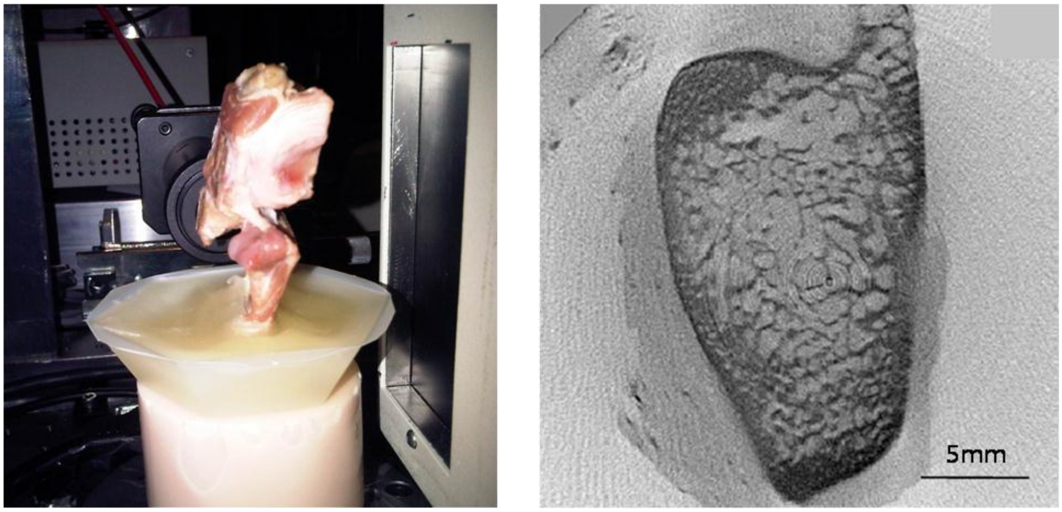

Fig. 13: (Left) Sagittally-cut porcine vertebra inside micro-CT scanner. The bone was embedded in a base of wax to hold it upright throughout the scanning procedure. (Right) CT cross-section of the vertebra. Individual trabeculae can be observed within the inner bone structure. Image taken with permission from the PhD thesis of Dr. Julius Pekar [146]

3.4.4. Hand-held digital microscope

Overhead images of bone samples were taken with a hand-held digital microscope (AM413MT, Dino-Lite). The microscope includes a 1.3 megapixel image sensor and could magnify up to 200×. This digital microscope connects to a computer via a USB connection and was used immediately following the completion of drilling experiments for the initial examination of drilled structures.

4. EXPERIMENT: ULTRASHORT PULSED LASER ABLATION THRESHOLD IN PORCINE CORTICAL BONE

4.1. Introduction

Due to the requirement of simultaneous absorption, multiphoton ionization is achievable only during high peak irradiation intensities. As well, in order to achieve optical breakdown, the irradiation must be intense enough to cause rapid ionization so that losses (due to inelastic collisions and diffusion of free electrons [147]) do not quench the electron avalanche [15]. Above a certain laser fluence threshold, the density of free conduction-band electrons reaches a sufficiently high density creating electrostatic forces which are strong enough to break down and eject target material. The minimum laser fluence below which ablation cannot be initiated is defined as the ablation threshold [148].

An understanding of the bone ablation threshold is crucial for the potential application of lasers in orthopaedic drilling procedures. Not only does the ablation threshold provide the minimum energy requirement for bone removal, but the drilling efficiency has been shown to decrease as a function of pulse energy at fluences significantly greater than the ablation threshold [43]. More specifically, Oraevsky *et al.* found crater depths and diameters to be at a maximum when using laser fluence two times the ablation threshold and ablation efficiency to have a distinct maximum at six times the threshold [118].

4.1.1. Previous methods for threshold determination

Different methodologies have been used for the determination of the ablation threshold in biological tissues; all of which involve the irradiation of material with pulses of decreasing energy until ablation has been deemed to have terminated. Due to the fundamental mechanics involved, the ablation threshold fluence for materials can differ significantly depending on the specific mechanism of ablation. When using sufficiently high irradiances for plasma-mediated ablation, the threshold has been found to only slightly depend on the tissue type and condition [43].

One method used for determining the ablation threshold involves measuring the volume or crater depth following ablation with different fluences. The crater volume/depth is evaluated as a function of fluence and the data is extrapolated to find the fluence at which the volume/depth is equal to zero. An optical microscope coupled with a micro-positioning depth gauge has previously been used to measure craters by focusing the objective lens on the crater rim and then refocusing on the crater floor [43, 123, 149]; however the high aspect-ratio of typical crater shapes can make measurements difficult [150]. Other studies have measured crater depths using optical profilometers or estimated volumes using optical coherence tomography (OCT) [104, 151].

Scanning electron microscopes (SEM) and optical microscopes have also been used to determine the ablation threshold of hard tissue by visualizing surface modifications following irradiation [28, 121, 152]. In these previous studies, the fluence below which no surface modifications were observed had been described as the ablation threshold; however, a more appropriate definition may be the effective damage threshold [122]. Surface damage can be characterized as a sudden observation of irreversible modification; however, the means of observation (e.g. optical or electron microscopy) differ strongly in sensitivity for different types of modifications. In addition, the damage threshold can depend significantly on the subjective impression of the individual studying the target [122]. Detecting surface modifications resulting from small laser fluence also requires material surfaces to be smooth and uniformly flat so previous investigators polished their bone samples prior to irradiation [28, 121, 152].

4.2. Determination of ablation threshold

4.2.1. Methods

Bone samples were harvested from the scapulae of pigs and left unpolished to mimic real-life conditions. The ablation threshold was investigated by irradiating bone surfaces with 1,000 laser pulses per spot with a range of 30 fluence levels from 0.1 to 13.0 J/cm^2. The effect of pulse number on the ablation threshold was examined by repeating the process using 25, 50, 75, 100, 300 and 500 incident pulses. The entire procedure was repeated three times on bone samples from the scapulae of three different pigs. The craters were viewed using reflected-light microscopy (Axioplan 2, Zeiss) and crater diameters were measured using image analysis software (Northern Eclipse, Empix Imaging). The crater diameter was defined as the maximum diameter of the region of removed tissue.

Based on the Gaussian intensity profile approximation, the D^2 method employs the relationship between the diameter of an ablated crater, the material-dependent ablation threshold fluence, the Gaussian beam radius, and the peak fluence of the beam [153]. For a Gaussian beam profile with a $1/e^2$ beam radius w_0, the radial distribution of the laser fluence is given as:

$$\phi(r) = \phi_0 e^{-\frac{2r^2}{{w_0}^2}} \tag{3}$$

where $\phi(r)$ is the fluence at a radial distance r and ϕ_0 is the peak fluence. Assuming that a defined material-dependent ablation threshold exists and that material surface perforation occurs when this threshold is exceeded, equation (3) can be rearranged to:

$$D^2 = 2{w_0}^2 \ln\left(\frac{\phi_0}{\phi_{th}}\right) \tag{4}$$

where D is the diameter of the removed tissue and ϕ_{th} is the threshold fluence for the sample. Fig. 14 demonstrates all these correlations. From a semi-log plot of D^2 versus peak fluence, ϕ_0, the ablation threshold was determined from the x-intercept.

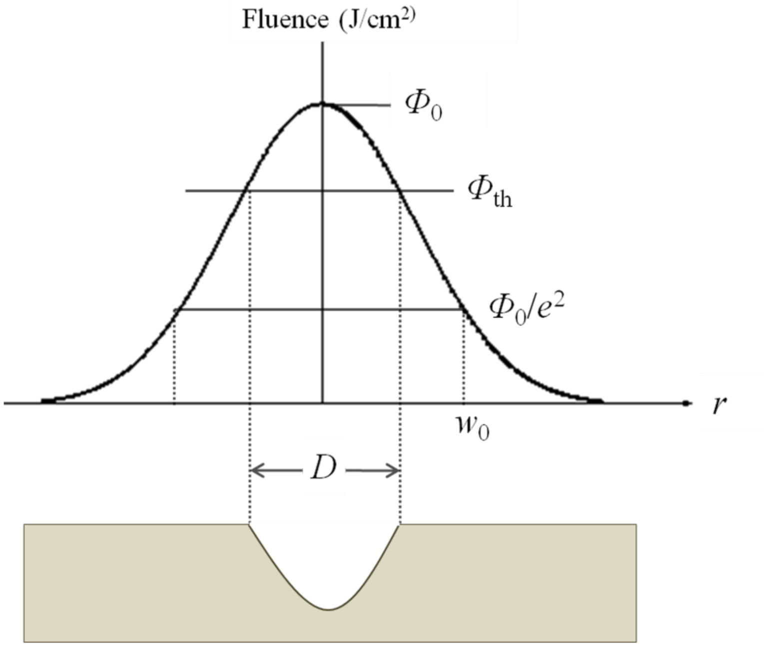

Fig. 14: Ablation with a Gaussian beam profile demonstrating the dependence of the ablation crater diameter, *D*, on the threshold fluence, ϕ_{th}

4.2.2. Results & Discussion

An example of ablation craters in unpolished cortical bone is shown in Fig. 15. There was no visual evidence of thermal damage or cracking in the surrounding material under 20× microscope viewing. The crater diameter was measured to be the span of the darkened region. The craters appear to have rims of discoloured tissue surrounding them. Due to their lightened colour, the rims were presumed not to be charred tissue, but instead, the result of ablation debris or the result of pressure-driven flow of molten bone tissue from the centre to the edge of the crater followed by re-solidification at the rim [148]. This resolidification of the melt after ablation also likely caused the asymmetries or irregular shapes in some craters [154].

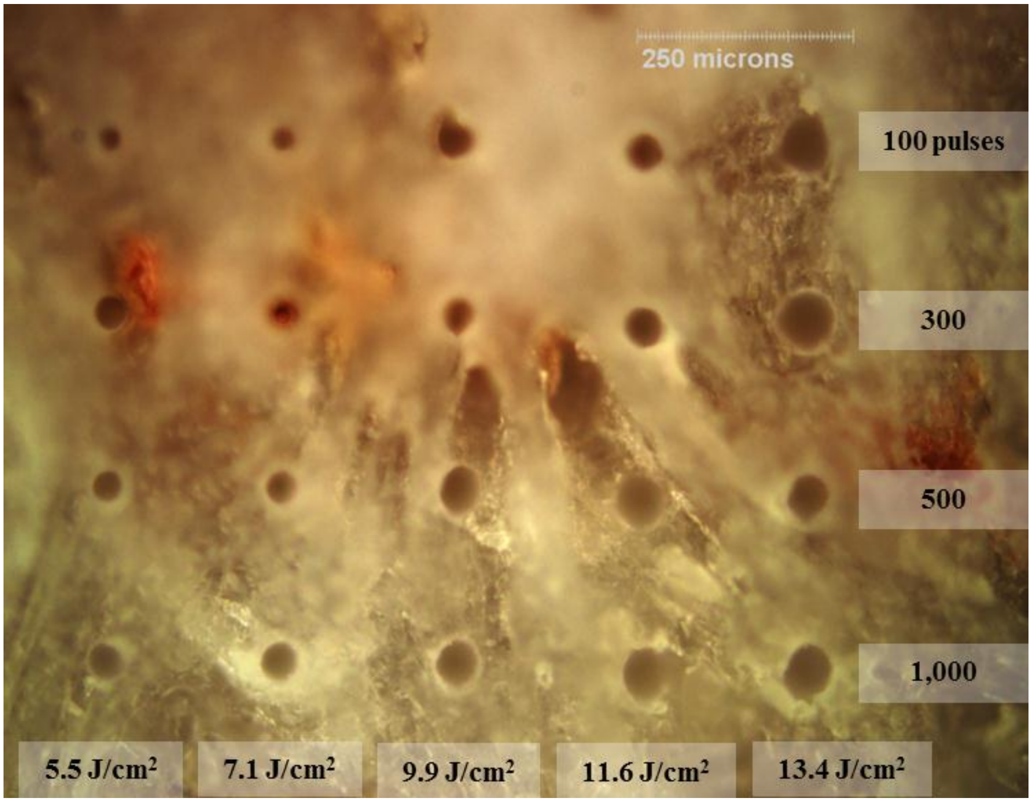

Fig. 15: Ablation craters cut into the surface of unpolished porcine cortical bone with 100, 300, 500, and 1,000 pulses per spot at energy fluences 5.5, 7.1, 9.9, 11.6, and 13.4 J/cm^2. Imaged using the reflected-light microscope and 20× objective. Due to the uneven bone surface, not all craters could be simultaneously in-focus i.e. the objective lens was re-focused during the diameter measurement of the 100 pulses/spot craters. The crater diameter was measured as the span of the darkened region.

Due to the asymmetry, orthogonal measurements of the diameter were carried out and the geometric average diameter was used. Squared diameter (D^2) vs. log of the peak fluence plots were created for all incident pulse numbers and are shown in Fig. 16. The results from all three scapulae are plotted in the same figure as Trial #1, #2, and #3.

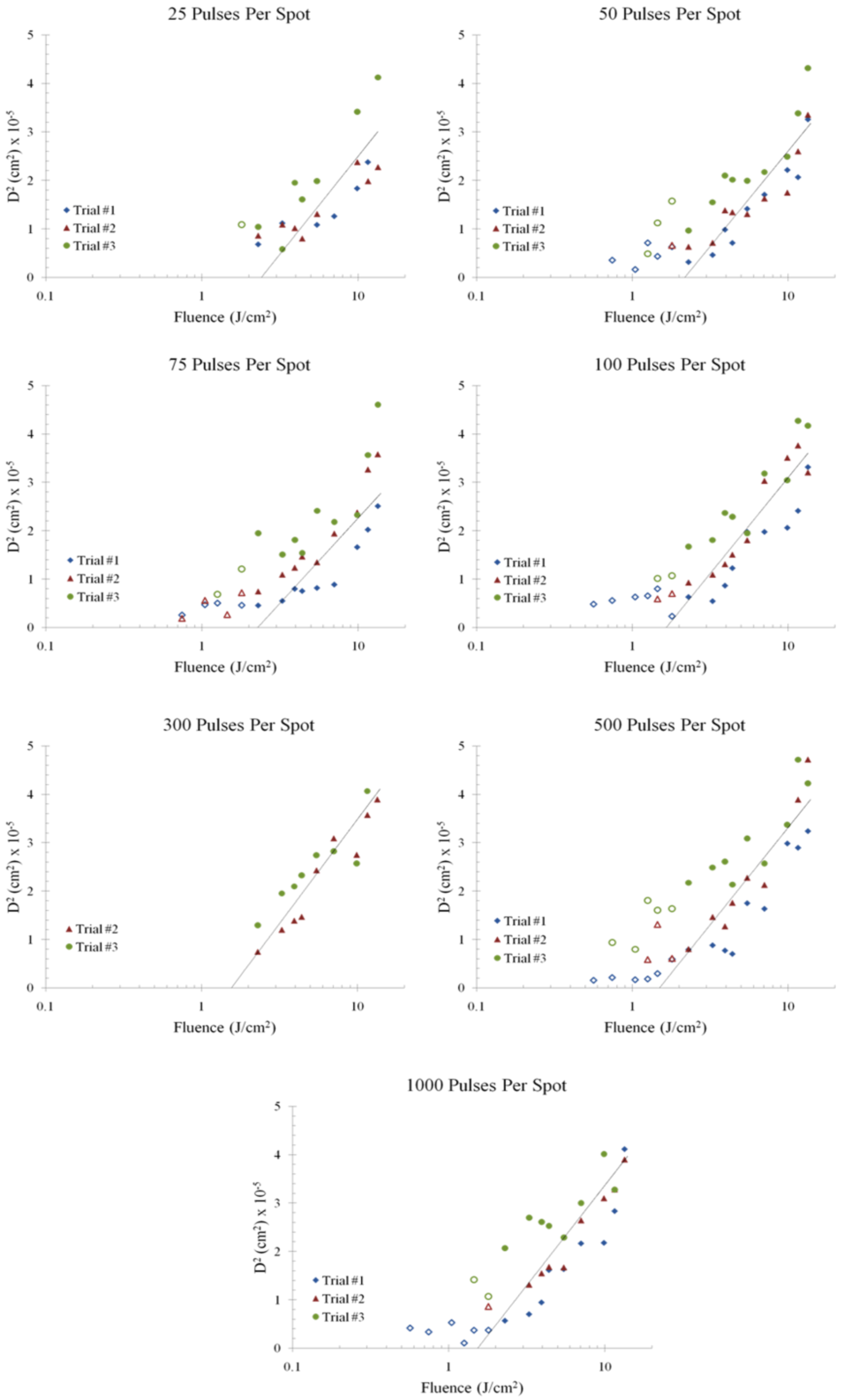

Fig. 16: Squared diameter (D^2) of ablated craters versus the peak fluence in porcine cortical bone ablated by multiple pulses per spot. Samples were irradiated with λ = 800 nm, τ = 180 fs pulses at a repetition rate of 1 kHz. Hollow points indicate ablation craters that were comparable in scale to bone surface irregularities and were not included in the calculation of the line of best fit. The slope and intercept of the plotted trend-lines were obtained from the weighted-average slope and intercept of the three individual least-square lines.

Each trial was fit using a linear least-squares algorithm (not shown) and the weighted-average slope and y-intercept were calculated from the three trials and used to construct the trend lines shown in Fig. 16. From these lines, the energy fluence ablation thresholds ϕ_{th} were obtained for each incident pulse number and are shown in Table 1. The irregularities in crater diameter seen in Fig. 16 were likely due to the irregular surface of the sample or the uncertainty in the laser focusing scheme.

Table 1: Fluence ablation threshold at different incident pulse numbers as measured using the D^2 method[a]

Incident Pulse Number (N)	Fluence Ablation Threshold (J/cm^2)
25	2.37 ± 0.78
50	2.36 ± 0.87
75	2.28 ± 0.76
100	1.72 ± 0.93
300	1.66 ± 0.87
500	1.69 ± 0.65
1000	1.75 ± 0.55

[a] Uncertainties were obtained from the standard errors in the fits from each trial

The ablation threshold in unpolished porcine cortical bone was found to decrease from a maximum of 2.37 J/cm^2 ± 0.78 J/cm^2 with only 25 pulses per spot to a minimum of 1.66 J/cm^2 ± 0.87 J/cm^2 with 300 pulses per spot. The measured ablation threshold at 1,000 pulses per spot differs significantly from that found by Girard *et al.* with the same number of pulses (0.69 J/cm^2) and similar laser parameters using bovine bone [28]. Some of the likely causes of this discrepancy may be due to differences in the definition of ablation or surface preparation. In the Girard study, ablation was deemed to occur when visual inspection of polished bone SEM images showed laser-induced damage. Lim *et al.* conducted single-pulse and linear scanned ablation tests with porcine cortical bone and used the D^2 method to calculate the threshold at multiple pulse numbers. The threshold at 1,000 pulses observed in this study was greater than that found by Lim *et al.* (1.22 J/cm^2 ± 0.29 J/cm^2), but there was good agreement at 100 pulses per spot (1.56 J/cm^2 ± 0.09 J/cm^2) [141]. The increased ablation threshold found in this study, compared those reported by Girard *et al.* [28] and Lim *et al.* [141] is likely the result of using unaltered bone in the current study versus polished bone in the others. Laser ablation strongly depends on the compositions and properties of the material. In the context of investigating ablation thresholds, a polished bone surface may be considerably different from the natural cortical bone surface. Sanding the bone can increase specular reflection, while surface corrugations can change the local field intensity and affect the threshold fluence [122].

As seen in Fig. 16, there appears to be different trends for D^2 through the range of fluence. Above ~2 J/cm^2, the crater area appears to increase logarithmically with fluence; however, at lower fluences, the crater area is less deterministic as a function of laser fluence. It has been suggested that this indicates a change in the ablation mechanism, from a soft/gentle ablation at fluences <2 J/cm^2 to a hard/strong ablation at >2 J/cm^2 [141]. Soft ablation results in a low rate of material removal and relatively smooth material surfaces while hard ablation results in a higher rate of removal and rougher surfaces [155]. Z-slices were obtained of the soft ablation craters by lowering the microscope objective 10 μm between successive image captures. In the example shown in Fig.

17, surface features in focus when the lens was fixated on the crater rim are still in focus as the lens was lowered by 10 and 20 μm. These features went out of focus as the lens fixated on the crater floor; 30 μm below the rim. These findings show the depths of the craters created with fluences <2 J/cm^2 to be comparable in size to the bone surface irregularities (ridges, pits) and could not be considered to constitute meaningful tissue removal. As a result, our least-square lines were fit using only the data points above 2 J/cm^2, denoted as solid points in Fig. 16.

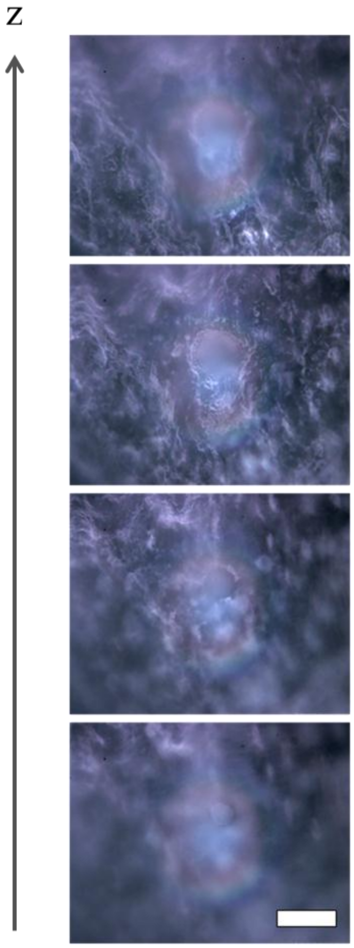

Fig. 17: Z-slices of soft ablation crater irradiated by 1,000 pulses with fluence of 1.0 J/cm^2. 10 μm between successive slices. (Top) Objective lens focused on the rim of the crater). (Bottom) Lens focused on crater floor. Note the surrounding features start to go out of focus as the lens is focused on the crater. (Scale bar width is 50 μm)

4.3. Investigation of incubation effect

4.3.1. Introduction

The reduction in ablation threshold with incident pulse number seen in Table 1 has been observed previously in metals [156, 157], semiconductors [158], polymers [159], and dental tissue [122]. Using scanning ablation, Lim *et al.* also observed a damage accumulation effect with higher pulse numbers and a subsequent increase in ablated channel width in bone [141]. This phenomenon is referred to as the incubation effect. Described using a power law model [160], the incubation coefficient, ζ, characterizes the degree of this effect and is an intrinsic property of the material. Lim *et al.* found the incubation coefficient for unpolished bovine cortical bone to be 0.89 ± 0.03 [141].

In metals, cumulative effects have been attributed to the accumulation of plastic deformations resulting from thermal stresses caused by incident pulses with fluences below the ablation threshold [161]. As a result of these deformations, the metal is then successfully ablated by pulses with energy fluences less than the single-pulse ablation threshold. In the case of semiconductors and insulators, laser-induced alterations such as defects of modifications in chemical properties are believed to be the primary cause for incubation effects [158, 162].

Laser machining of bone during surgical procedures will require a large number of laser pulses. Therefore, incubation will play an important role in the determination of an appropriate laser fluence that will avoid excessive energy deposition and resultant tissue damage. In this section, the data presented in Table 1 and the power law model was used to quantify the incubation effect in unpolished cortical bone through the measurement of the incubation coefficient. As well, the incubation model also allows for the extrapolation of the single-pulse ablation threshold of unpolished bone, which was not possible to determine experimentally due to the inherent roughness of the sample.

4.3.2. Methods

The incubation effect follows a power law equation [160] that was originally developed for metals under nanosecond pulse irradiations, but has been adopted for semiconductors [158] and insulators [162] with the use of femtosecond laser pulses. The fluence threshold for N pulses, $\phi_{th}(N)$, is related to the single-pulse ablation threshold, $\phi_{th}(1)$ by:

$$\phi_{th}(N) = \phi_{th}(1) \times N^{\zeta - 1} \qquad (5)$$

where ζ is the incubation coefficient. The incubation coefficient characterizes the degree of incubation - the change in the ablation threshold with pulse number. A rearrangement yields a logarithmic relationship between the accumulated fluence, $N \times \phi_{th}(N)$, and N, with the proportionality constant equal to ζ. A log-log plot of the accumulated fluence versus the incident pulse number will have a slope equal to the incubation coefficient and a y-intercept equal to the single-pulse ablation threshold.

4.3.3. Results & Discussion

The results for the accumulated fluence, $N \times \phi_{th}(N)$, versus incident pulse number, *N*, are shown in Fig. 18. The data was fit with a power function and the R^2 value was 0.988. From the equation of the best fit line, the incubation coefficient, ζ, was found to be 0.89 ± 0.03. From extrapolation (shown as the dotted line in Fig. 18), the single-pulse ablation threshold, $\phi_{th}(1)$, was found to be 3.29 J/cm^2 ± 0.14 J/cm^2. The incubation coefficient in unpolished porcine bone found in these experiments is within the same range as that found for polished bovine bone [141]. However, the single-pulse ablation threshold with a femtosecond laser source was higher than that found by Lim *et al.* [141] (2.70 J/cm^2 ± 0.16 J/cm^2) using a comparable wavelength and pulse duration.

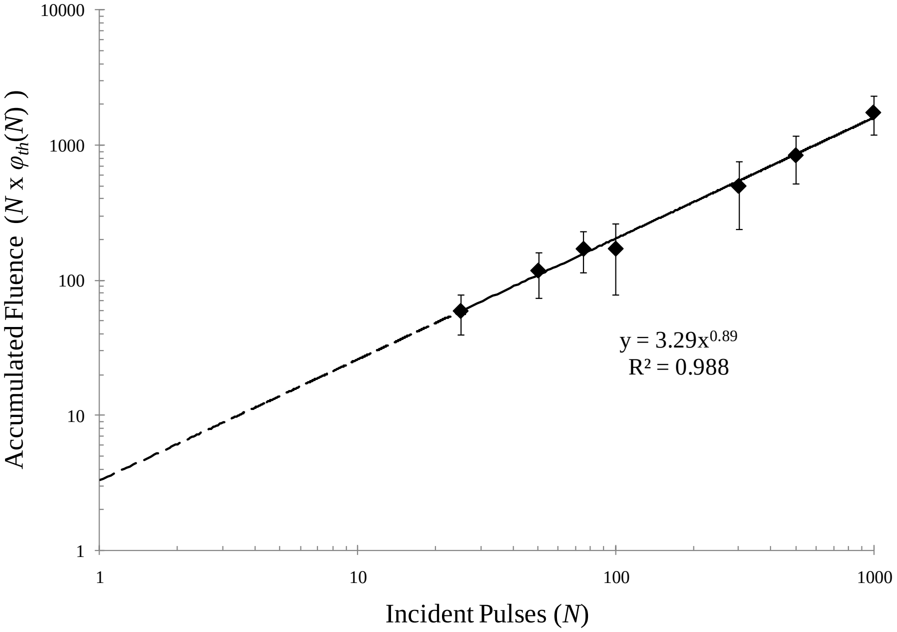

Fig. 18: Incubation power law for porcine cortical bone irradiated with λ = 800 nm, τ = 180 fs pulses. The data was fit with a power function with R^2 = 0.988. The incubation coefficient, ξ, was 0.89 ± 0.03 and the single-pulse ablation threshold fluence was 3.29 J/cm^2 ± 0.14 J/cm^2. Error bars were derived from the ablation threshold uncertainties reported in Table 1.

Incubation effects in real tissue are likely the result of linear absorption of fluences even below the damage threshold. At high pulse numbers and repetition rates, heat accumulation can cause material to be thermally-modified, which in turn changes the dielectric constants of the tissue and the local electric field. As a result, the ablation threshold can be altered. Additionally, electronic defects can be created in the band gap even at minimal temperature increases, which can also increase absorption [122]. The identical incubation coefficients found in this study and by Lim *et al.* [141] suggest similar thermal modifications and other laser-induced defect formations in both polished and un-polished bone. The higher single-pulse threshold measured in porcine bone compared to bovine [141] suggests that porcine bone requires more energy to remove bone tissue with laser ablation than bovine. This increase in fluence could also be attributed to the rough surface of the bone samples used in this investigation. While similar incubation effects occur in porcine and bovine cortical bone, the greater similarity between the bones of humans and pigs on the microscopic level and the use of unaltered bone allows for the application of the data presented in this study to human subjects.

5. EXPERIMENT: CHARACTERIZATION OF DRILLING PARAMETERS

5.1. Introduction

The application of lasers for hard tissue ablation in orthopaedic procedures will require high drilling efficiencies (short drilling times), precise machining, and minimal collateral damage. Previous investigations have already demonstrated the capability of ultrashort pulsed lasers to ablate bone tissue in a precise manner with significantly reduced thermal damage compared to other lasers [28, 44, 121, 122, 140]. However, the tissue removal rate for ultrashort pulsed lasers have also been shown to be less than that of longer-pulsed infrared lasers [43, 119, 136] and also significantly less than the removal rate of mechanical cutting tools [163]. As a result, ultrashort pulsed lasers still have limited clinical utility.

The objective of the experiments presented in this chapter was to evaluate and characterize various laser parameters, such as pulse energy and duration, as well as drilling protocols, such as the depth of the laser beam focal-plane. With an understanding of the different laser and drilling parameters and their effects on hard tissue ablation, it becomes possible to devise specific laser configurations and drilling strategies to optimize drilling efficiency and reduce procedure times. The adjustable nature of the bench-top Ti:Sapphire laser system allowed specific parameters to be analyzed with relative ease.

5.2. Removal rate versus fluence: intra-species comparison

5.2.1. Methods

Pig radius/ulna bone samples were linearly-ablated with 170 fs pulses with a wavelength of 800 nm at a repetition rate of 1 kHz to investigate the removal rate (ablation depth per pulse) as a function of laser fluence. The focal-plane of the beam was aligned with the bone surface. With the 125 mm objective lens and quartz viewing window in place, the laser power was adjusted to 180 mW. 15 lines were ablated in the surface of the samples with decreasing fluence. During this experiment, a half-wave plate (HWP) was used to adjust the laser power instead of the filter wheels. The lines were 5000 μm long with 200 μm between each line and were ablated with a translational speed of 250 μm/s. The number of pulses incident on each spot lying on the scanned line was calculated from [141]:

$$N_{scan} = \frac{d}{s} * f \tag{6}$$

where d is the diameter of the beam spot, s is the scanning speed, and f is the pulse repetition rate. Assuming a spot size of 30.2 μm, the number of pulses per spot, N_{scan}, was calculated to be 121. After successfully drilling 5 lines, a gap of 400 μm was created between the next set of 5. This was done to better distinguish the ablated channels when viewing under the microscope. After fixation, samples were cut cross-sectional to the channels using the diamond-blade sectioning saw and mounted on microscope slides.

The tissue removal rate was also investigated in a chicken humerus bone. The same drilling protocol as for the porcine bone was followed; however, the traditional filter wheels were used to adjust the laser fluence rather than the HWP.

5.2.2. Results & Discussion

An example of a cross-sectional histology slice showing a side-profile of ablated lines in porcine cortical bone is shown in Fig. 19. The five channels shown in Fig. 19 were ablated with the five highest peak fluence levels.

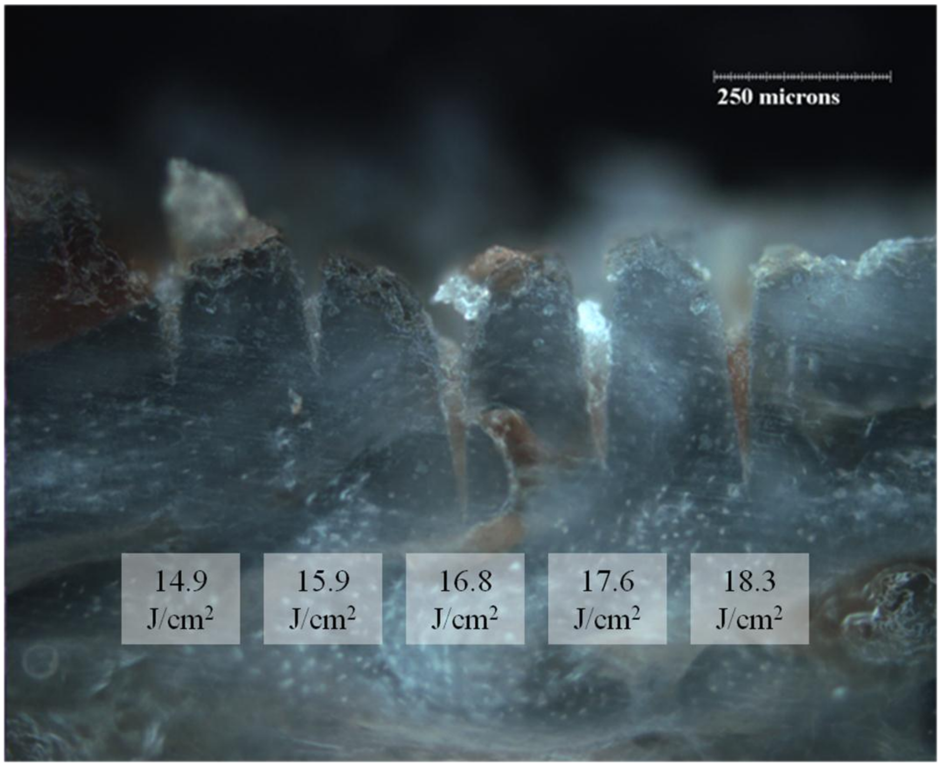

Fig. 19: Ablated channel cross-sections viewed with 20× objective reflected-light microscope. The channels were cut in order from highest fluence to lowest (right-most channel ablated first).

The removal rate was calculated by dividing the measured depth of the channel by the number of incident pulses. Over the first few ablated channels, the removal rate decreased considerably with peak fluence (18.3 to 16.8 J/cm^2). The rapid decline in removal rate with fluence slowed after the first three channels and appeared to level off at fluences <15 J/cm^2 (Fig. 20). The rapid drop-off in removal rate was presumably due to a build-up of condensation on the viewing window of the drilling vial which formed readily during the ablation of porcine bone. Water on the viewing window would absorb incoming laser energy and lower the effective power. The same "fogging" effect was not seen after the ablation of chicken bone and the removal rate was considerably higher than for porcine bone.

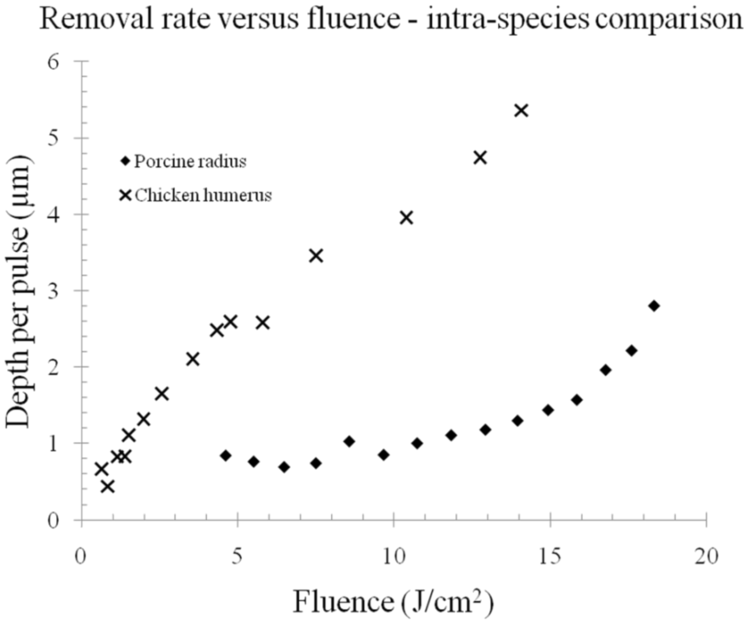

Fig. 20: Removal rate of porcine and chicken cortical bone at various peak laser fluence. Porcine bone had a rapid decline in tissue removal rate presumably from a build-up of condensation on the drilling vial window. The same shielding effect wasn't seen in chicken bone. The laser fluences used differ between the porcine and chicken samples due to the use of the HWP versus filter wheels

While the influence of “fogging” makes it difficult to compare the results of the removal rates for chicken and pig cortical bones, at first glance, it appears that material is removed much more readily from the chicken bone than porcine. This result is likely due to the differences in bone composition between pig and chicken. Since pigs have been found to best match humans in their degree of mineralization, composition, and mechanical competence [164], further studies with porcine bone are needed in order to fully understand the relationship of laser fluence to removal rate. These studies will likely need to incorporate a vacuum-suction system to remove bone debris and water vapour during ablation. Previous studies of hard tissue removal using ultrashort laser pulses have reported bovine cortical bone removal rates of 1.5-2 μm/pulse at fluences of 5 J/cm^2 [139].

From the sample cross-sections, the depths of ablated channels were measured from the bone surface to the deepest point of visible deformation. However, as can be seen in Fig. 19, there appears to be bone material still remaining within the channel. This material could either be bone debris that has been caught in the channel during the ablation process, or the result of using a rotary saw to section the sample. As bone tissue is removed by the saw, the rotation of the saw blade can push the material into the ablated channels. Thinner cross-sections (<500 μm) might reduce the amount of material build-up within the channels; however results presented here were limited by precision of the saw.

5.3. Removal rate with different incident pulse numbers

5.3.1. Methods

During scanning ablation procedures, the translational speed determines the number of pulses incident on the sample. To investigate the influence of pulse number on removal rate, porcine samples harvested from scapular bone were linearly-ablated with 10 different translational speeds (100-1000 μm/s). For this experiment, the laser power was adjusted to 59 mW using a filter wheel combination OD of 0.5 and the pulses were 170 fs in duration. The laser fluence was 8.2 J/cm^2. The ablated lines were 10,000 μm long with 200 μm spacing between each line. To prevent a build-up of condensation in the drilling vial, bone samples were air-dried for two hours prior to ablation. From Equation (6), the pulses per spot for each scanning speed are shown in Table 2.

Table 2: Pulses per spot at various scanning speeds with a pulse repetition rate of 1 kHz. The crater diameter was assumed to be 30.2 μm.

Scanning Speed (μm/s)	Pulses Per Spot
100	302
200	151
300	101
400	76
500	60
600	50
700	43
800	38
900	34
1000	30

5.3.2. Results & Discussion

After ablation, bone debris was visible on the walls of the drilling chamber but only traces of condensation were seen on the viewing-window. A top-view image of the ten ablated channels was obtained with the hand-held digital microscope and is shown in Fig. 21 along with a cross-sectional image of five channels ablated with translational speeds of 500, 400, 300, 200, and 100 μm/s (left to right).

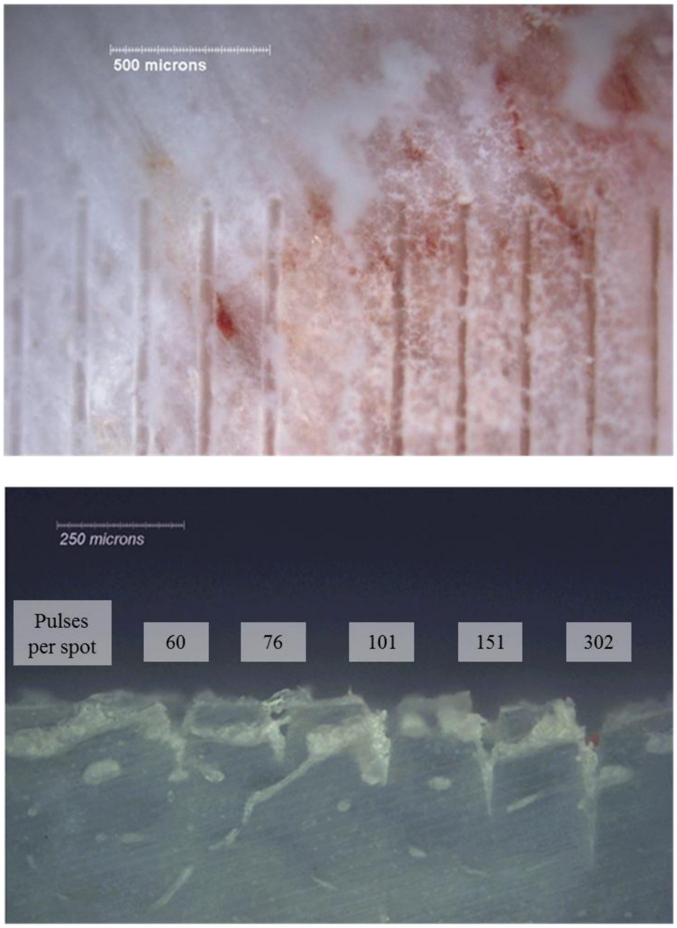

Fig. 21: (Top) Digital microscope top-view of ten ablation channels made with different scanning speeds and different incident pulse numbers. The scanning speed decreases from left to right. (Bottom) Cross-sectional histology slice of five ablation channels under 10× objective of reflected-light microscope.

The channel depths were measured and the total channel depth and removal rate versus incident pulse number are both shown in Fig. 22. The highest pulse number (302) resulted in the greatest channel depth (317.7 μm). However, the depth of removed tissue per pulse appeared to be greatest when ablating with 50 to 100 pulses incident at each spot along the length of the channel.

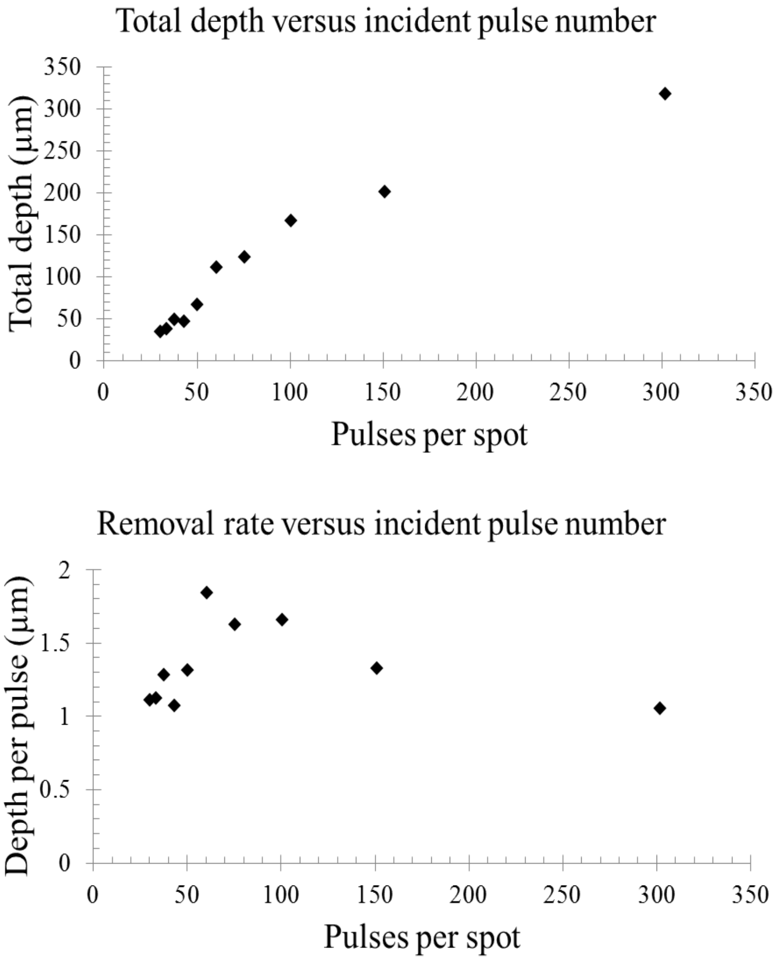

Fig. 22: Graphs of (top) total channel depth versus incident pulse number and (bottom) removal rate versus pulse number in porcine cortical bone. With a 1 kHz pulse repetition rate, a maximum removal rate of 1.8 μm/pulse occurred when linearly-scanning the bone surface at 500 μm/s which translated to 60 pulses per spot along the ablated channel.

More energy is deposited in the tissue volume when ablating with a higher number of incident pulses per spot and, as a result, the total crater depth is increased. However, a greater crater depth has been shown to decrease the rate of subsequent ablation [121, 165, 166]. Bone debris is more likely to collect in the bottom of deep craters which can shield the surface of the bone and lower the removal rate of succeeding pulses. The effective intensity of the beam also decreases as a crater increases in depth due to Gaussian beam divergence [167]. Lastly, the increase of the crater depth with pulse number leads to the increase of the inclination of the irradiated area relative to the original target surface. As a result, the effective laser fluence on the walls of the crater decreased [165].

The removal rate was found to be greatest at pulse numbers between 50 and 100. As the scanning speed was increased further and the number of pulses per spot declined, the removal rate also decreased. It is hypothesized that at lower pulse numbers (<50), the cumulative effects of multi-shot ablation are negligible. At low pulse numbers, there is minimal heat build-up or accumulation of other laser-induced defects [168] which have been previously shown to lower the ablation threshold (Section 4.3).

Successful medical applications will require many laser pulses to achieve deep cuts in bone. From the results of this investigation using a 1 kHz pulse repetition rate, the tissue removal rate was observed to be highest when ablating with 60 incident pulses per spot. To achieve deeper cuts with comparable removal rates, additional measures would have to be taken to offset the suspected causes of inefficiency i.e. flushing of bone debris, lowering the laser beam focal-plane after successive passes.

5.4. Removal rate versus pulse duration

Clinical use of sub-picosecond pulses in tissue ablation is not practical at this stage due to the high cost of sub-picosecond lasers compared to longer pulse lasers. Also, due to group velocity dispersion and issues with fibre damage due to self-focusing, it is difficult to use standard optical fibres for ultrashort laser pulse delivery [121]. However if laser pulses in the range of 1-10 ps showed similar characteristics as femtosecond pulses, the cost and delivery problems might be alleviated.

5.4.1. Methods

The removal rate in porcine scapular bone was evaluated using pulses of four different durations: 150 fs, 500 fs, 5 ps and 10 ps. The pulse duration was adjusted using the optical gratings in the amplifier – the amount of pulse compression is determined by the grating pair separation. The pulse durations were measured using the autocorrelator. The laser power was adjusted to a maximum of 102.3 mW. The average energy fluence was kept constant while four channels were ablated with the various pulse durations. To compare the effect of pulse duration at different energies, the drilling procedure was repeated at a total of five different fluences – all of which were greater than the ablation threshold values presented in Section 4.2. Each channel was 6 mm in length, had 200 μm line spacing, and was ablated with a 250 μm/s scanning speed. The channel depths were measured from cross-sectional histology slides and the removal rates were calculated. To establish a measurement uncertainty, crater depths were measured from multiple cross-sections obtained from the same ablated sample.

5.4.2. *Results & Discussion*

The removal rates of different pulse durations are shown in Fig. 23. At all fluences examined, the removal rate was inversely related to the pulse duration. It should be noted that the differences between the removal rates of 150 fs and 500 fs were not always significant.

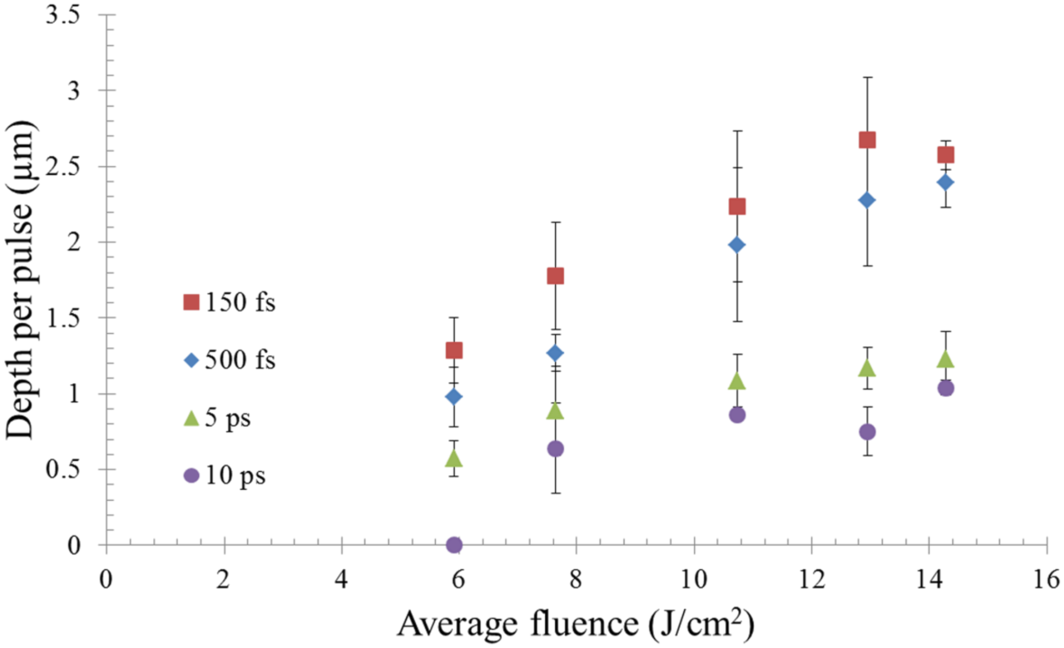

Fig. 23: Comparison of ablation rates at different pulse durations over a range of fluence. Uncertainty in the depth per pulse was calculated from the variation in channel depths between different cross-sections obtained from the same sample.

Pulse duration is an essential physical parameter of laser light that determines its interaction with matter [15]. As the pulse duration decreases at a fixed energy level, the peak laser intensity increases. Higher peak intensities result in stronger multiphoton absorption which results in optical breakdown occurring at lower average energies. Previous studies using both inorganic targets [169, 170] and various biological tissues [116, 135] have indicated a relationship between the plasma-mediated ablation threshold fluence ϕ_{th} and pulse duration τ of the form $\phi_{th} \sim \sqrt{\tau}$ for pulses between 4 ps and 8 μs [15]. Another study in biological soft tissue shows a plateau in the ablation threshold between 100 fs and 1 ps which could explain the similarities in the ablation rates of 150 fs and 500 fs laser pulses as seen in Fig. 23.

The observed increase in removal rate with shorter pulse duration can also be explained by the effect of plasma shielding [171]. By examining the temporal evolution of surface reflectivity during optical breakdown, Siegel *et al.* reported a weak reflectivity increase due to the production of surface plasma starting 100 fs after the ablation pulse. The plasma reflectivity continued to increase until it reached a maximum at t = 1.5 ps [112]. From these findings, it is likely that plasma shielding became more significant as the pulse duration increased and resulted in the reduction in efficiency seen in Fig. 23.

Even with reduced efficiencies due to factors inherent in optical breakdown and plasma shielding, the removal rates for 5 and 10 ps pulses were not insignificant. At fluences greater than 10 J/cm^2, the removal rates for these pulse durations were between 0.8 and 1.2 μm/pulse. Since lasers producing 1-10 ps pulses will likely cost less than femtosecond lasers and be less prone to fibre damage and dispersion during pulse delivery, future investigations should focus on this pulse regime.

5.5. Ablation depth with multiple passes at variable focus depths

5.5.1. Methods

As suggested in Section 5.3, variable focus depths could be used as a drilling strategy to offset the reduction in tissue removal rate as crater depths increase. In this experiment, the focal plane of the beam was progressively lowered between successive passes of the laser.

The laser power was adjusted to 239 mW and had a wavelength of 800 nm. The pulse duration as measured by the autocorrelator was 170-189 fs. Long scans showed a small presence (~0.002%) of satellite pulses that were 26 ps in duration. 8 mm long channels were ablated with a 250 μm/s scanning speed. An OD of 0.0 was used to achieve maximum pulse energy, resulting in a laser fluence of 33.4 J/cm^2. The first ablation channel was created with the beam focal plane aligned with the sample surface. For the second channel, the surface was ablated with the focal plane aligned with the surface; then the beam focus was lowered by 150 μm and a second pass along the channel was made. Similarly, the third channel had the same two cuts as previously plus an additional pass with the beam focus now 300 μm below the sample surface. Successive layers were chosen to be

150 μm apart since this value slightly exceeded the optical penetration depth (~105 μm); therefore, preventing deeper layers from accumulating radiation-induced effects. A sample diagram of all five channels is shown in Fig. 24. Multiple cross-sections were obtained from the same ablated sample and viewed under the wide-field deconvolution microscope.

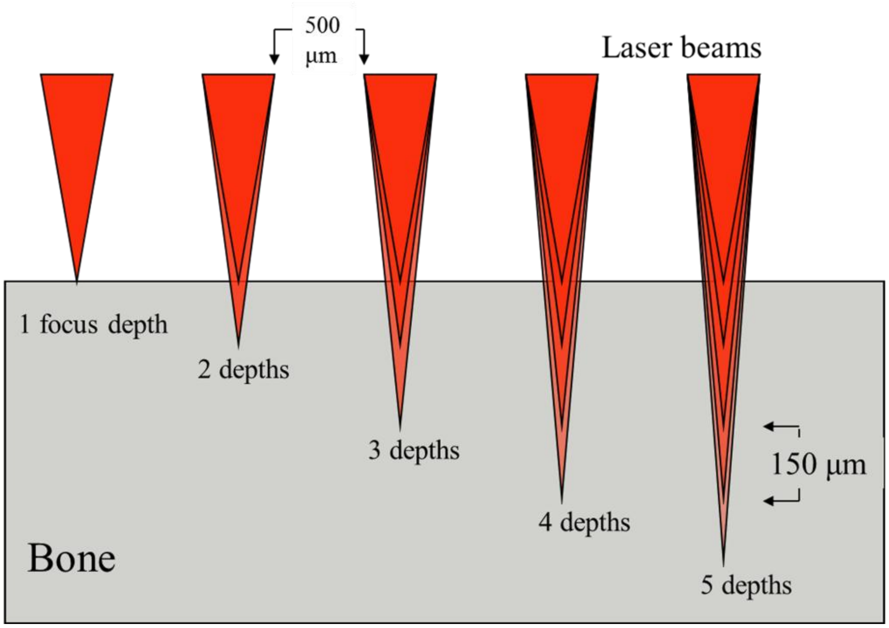

Fig. 24: Schematic of the variable beam focus drilling strategy. The beam focus was lowered 150 μm in the Z-direction (into the bone) for each successive pass. This procedure was designed to offset the reduction in drilling efficiency as craters deepen. 500 μm of space was left between each channel.

5.5.2. Results & Discussion

A plot showing the total crater depths of all five channels is shown in Fig. 25. The total crater depth increased as additional passes were made with the laser focal plane lowered in the Z-direction. The difference between crater depths was taken to find the increase as a result of the variable beam focus. From these results, the average increase in total crater depth after lowering the beam focus by 150 µm was found to be 138.9 µm ± 56.2 µm.

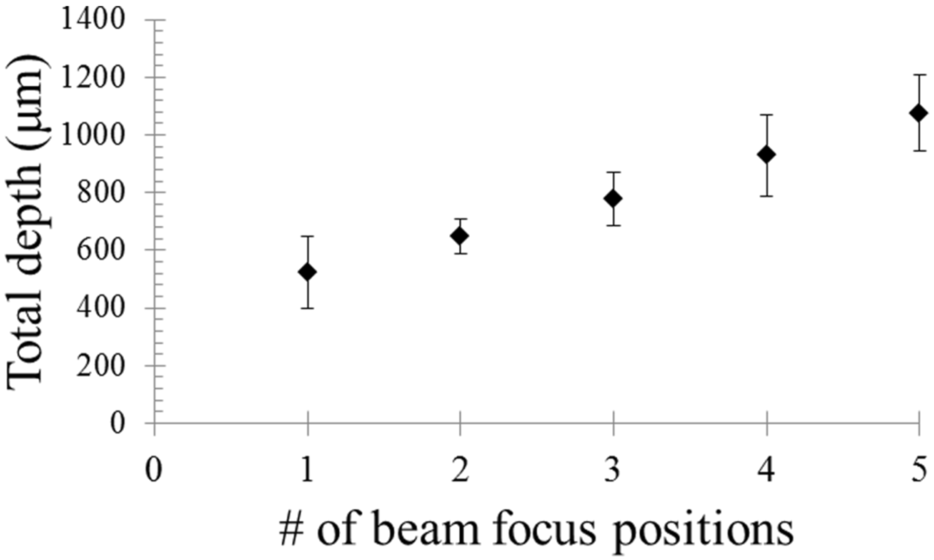

Fig. 25: Total crater depth after ablating porcine bone with multiple beam focus positions. 1 beam focus positions means the laser was scanned along the surface with the beam focal-plane aligned with the surface. The distance between successive beam focus positions was 150 µm (Z-direction). Uncertainty came from multiple crater depth measurements obtained from different cross-sectional slices taken from the same irradiated sample

It should be noted that the incident pulse number was not normalized between channels for this investigation – the channel ablated with only 1 beam focus position had half as many incident pulses as the channel ablated with 2 focus positions. To fully understand the relationship between ablated depth and beam focus positions, the same incident pulses should be used for all channels. It is likely that the rate of increase in total depth would slow due to the increased difficulty in clearing bone debris from deeper craters. The 're-focusing' technique appears to have future potential in the drilling of deeper cuts or large-scale structures. At first glance, a change in focal-plane position by 150 μm appears to be relatively small when compared to the total Rayleigh length (z_R=895 μm) for this focusing objective. At a distance of 150 μm from the beam waist ($2w_0$) along the direction of propagation, the diameter of the Gaussian beam can be calculated from [117]:

$$2w(z) = M^2\left(2w_0\sqrt{1+\left(\frac{z}{z_R}\right)^2}\right) \tag{7}$$

where M^2 is a measure of the laser beam quality and can be calculated from the beam waist and divergence. Although the M^2 factor hadn't been experimentally measured in a long period of time, the factory specifications of the laser system quoted an M^2 of <1.5. As a result, when using the 125 mm focusing lens, the beam waist can increase to as much as 46 μm at a distance of only 150 μm from the focal plane. Since optical breakdown has a strong non-linear relationship with intensity [15] and plasma-mediated ablation is well-localized, it was important to adjust the beam focal-plane by only a small amount before each pass.

Fig. 26 (a) contains sample images of three channel cross-sections as observed under 10× objective viewing. The right-most and centre channels ablated with 3 and 4 beam focus positions, respectively, both appear simply as darkened regions, likely due to the presence of bone tissue being pushed into the channel during sectioning. However, the channel ablated with 5 beam positions (left of image) appears to contain a distinct region of cleared tissue. When the laser beam focus was shifted down in the Z-direction for machining subsequent layers, the defocused laser fluence applied to the top surface and crater side-walls resulted in further ablation. As seen in Fig. 26 (b), when the focal-plane was lowered a total of 600 μm, the beam diameter at the bone surface was <54 μm (as calculated by Equation (7), which is substantially wider than the beam waist of 30.2 μm. This increased beam width results in an overall increase in crater diameter, primarily at the crater opening.

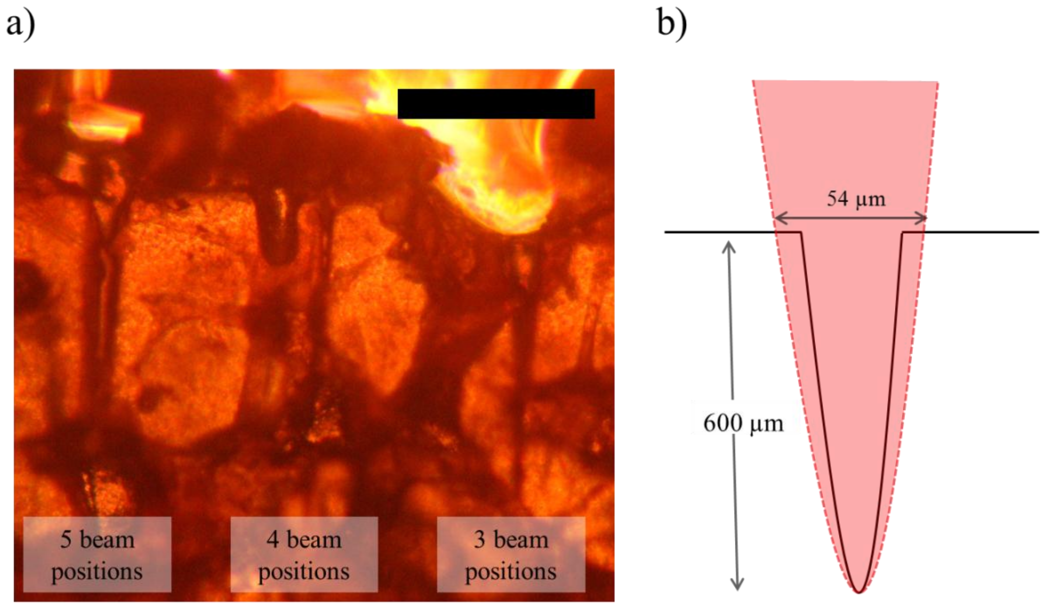

Fig. 26: (a) Sample cross-sectional image of three channels ablated with (L to R) 5, 4, and 3 beam positions. The channel ablated with 5 beam positions appeared to be significantly wider and free of debris unlike the 4 or 3 beam position channels. (Scale bar width is 500 μm) (b) Diagram of laser beam width at the bone surface when the focal-plane was positioned 600 μm into the tissue (as in the 5-beam channel). Diagram not drawn to scale.

Along with a defined region of removed tissue, the 5-beam-position channel in Fig. 26 also has a region of darkened tissue surrounding it, presumably the result of thermal damage. These undesired effects were likely the result of using maximum laser power for this investigation (239 mW) which would be avoided during clinical applications.

5.6. Drilling without pulse amplification

In 2007, Lee *et al.* reported the first experimental demonstration of laser osteotomy directly using a low-cost mode-locked extended cavity oscillator [137]. A mode-locked laser oscillator has a much higher pulse rate (10-100 MHz) and a much lower peak power (10-100 kW) than laser systems that incorporate the use of amplifiers, which tend to be fairly complex and expensive. Lee *et al.* found that the high pulse rate introduced Joule heating to the ablated bone tissue while the kW peak power in the ultrashort pulse was still effective in introducing multiphoton absorption and avalanche ionization [137]. This sub-section will briefly describe our attempts to ablate bone using the Ti:Sapphire oscillator.

5.6.1. Methods

The Ti:Sapphire oscillator (Tsunami) was used to generate pulses with energy of 7.5 nJ and a duration of 90 fs at a repetition rate of 82 MHz. In preparation for the experiments, the oscillator output beam was re-routed into the focusing objective. After passing through the optical equipment, the stable laser power at the sample surface was 360 mW which corresponded to 4.4 nJ per pulse. To increase the laser fluence, an f = 75 mm focusing objective was used to obtain a smaller ablation spot. The peak power was 48 kW.

Since this was a proof-of-concept investigation, a large box pattern was raster scanned on the surface of a porcine cortical bone to determine if bone tissue could be removed using pulses directly from a mode-locked oscillator. The box pattern consisted of 200 lines spaced 5 μm apart. Each line was 1 mm in length and the scanning speed was 250 μm/s.

5.6.2. Results & Discussion

Even though a relatively large (1 mm × 1 mm) pattern was ablated in the surface of the bone tissue, no visible debris was present in the drilling chamber upon inspection with a hand microscope and LED light source. Later, the sample was viewed under the reflected-light microscope and no visible surface damage was observed.

Oscillator-only micromachining is fundamentally different than micromachining with an amplified laser system [101]. The time interval between the pulses emitted by a femtosecond laser oscillator is on the order of tens of nanoseconds, which is significantly shorter than the time required for heat to diffuse out of the focal volume (see Fig. 5). Over time, the energy from successive pulses accumulates around the focal volume and produces structural changes. A common use of oscillator micromachining is for the manufacturing of integrated optical components, such as wave guides, in transparent materials [101, 172].

Lee *et al.* proposed a hybrid ablation mechanism when ablating bone with a mode-locked Nd:$YVO_{4.}$ The average laser power would first carbonize the osseous tissue, as a result of the extremely high repetition rate and then the peak laser power of the ultrashort pulses would subsequently remove the carbonized material [137]. The average laser power used in this investigation (360 mW) exceeded that used by Lee *et al.* (160-280 mW) [137], however, the extended-cavity oscillator laser used by Lee *et al.* was able to generate higher energy pulses than was possible in this study, even at a lower average power [173]. The specific pulse energy used in the aforementioned study was not reported in the literature [137].

A high numerical aperture (NA) objective lens is required for oscillator-only drilling in order to generate the peak intensities needed for optical breakdown [172]. The beam spot used in our investigation was not measured; however, can be roughly approximated from a generalized law for Gaussian beam propagation through a lens of focal length f [174]:

$$2w_0 = M^2 \frac{4\lambda}{\pi} \frac{f}{D} \tag{8}$$

where D is the oscillator beam output diameter. From factory specifications, the beam diameter is <2 mm ($1/e^2$). Using the $f = 75$ mm objective lens, the beam spot diameter was approximated to be >38.2 μm (without correcting for beam divergence) which would yield a peak intensity <1.0 GW/cm^2. In comparison, Lee *et al.* ablated bone with a peak intensity of 1.3 GW/cm^2 [137].

While only the unsuccessful results of a brief proof-of-concept experiment are presented here, the promising results of Lee *et al.* (<60 s for laser osteotomy of pig femur) [137] provide a possible direction for future experiments in ultrashort pulse bone ablation.

6. EXPERIMENT: LARGE-SCALE TISSUE REMOVAL

6.1. Introduction

To successfully replace mechanical cutting and drilling tools in orthopaedic surgery, ultrashort pulsed lasers will require the ability to remove relatively large volumes of bone tissue in appropriate operating times. Pedicle screw pilot-holes are typically 3 mm in diameter and ~30 mm deep depending on the anatomical location [22, 175]. During prosthetic implant procedures, such as knee or hip replacements, bone reshaping is typically performed using mechanical saws to create flat, millimetre-scale regions that are required for prosthetic fixation [176]. To be used for osteotomies, lasers must be capable of cutting through millimetres, or even centimetres, of bone.

In Chapter 5, the effects of different laser parameters, such as scanning speed and pulse duration, on the removal rate of bone tissue were investigated. However, even with optimized laser parameters, the final crater depth is ultimately limited by beam-scattering off the crater walls and the accumulation of ablation debris at the site of incidence [122, 167]. In this chapter, we investigate different drilling strategies specifically designed to alleviate the aforementioned limitations and allow for large-scale (>1 mm^3) bone tissue removal.

Circular scanning has been previously used by Girard *et al.* to remove 1 mm diameter cores of bone tissue from 200 μm thick bone samples [28]. Lim *et al.* was able to fabricate micro-pillars in the surface of bone using concentric circular beam scanning with a fs pulsed laser [141]. The innermost circle had a diameter equal to the programmed diameter of the pillar (5, 10, 30 or 100 μm) and the surrounding material was removed in 45 concentric circular passes. The beam focus was also lowered in the Z-direction to ablate subsequent layers of tissue and create taller micro-pillars. The beam focus location was lowered 10 μm for each subsequent layer, yielding a maximum micropillar height of ~100 μm after 9 successive layers. McCaughey *et al.* utilized a spiral scanning technique to ablate 3 mm diameter structures in the surface of bone from the human optic capsule; however, did not adjust the beam focus and only removed tissue up to a depth of 90 μm [140].

The objective of the experiments presented in this chapter was to further develop the aforementioned large-scale tissue removal strategies. Concentric circle and helical scanning were both incorporated with adjustable beam focus techniques in order to achieve precise fabrication of structures on a millimetre scale. Since bone tissue laser ablation in a clinical setting could also include the removal of trabecular bone, an investigation into large-scale removal of trabecular bone was performed. Lastly, due to its potential use in future hard tissue ablation studies, the laser parameters of the ultrafast system were configured in such a manner that the final beam characteristics resembled those of a Nd:YAG laser (8 ps pulse duration, 130 μJ per pulse, 200 Hz repetition rate). The capability of an Nd:YAG laser to remove bone tissue on the millimetre scale through the use of concentric circle scanning was evaluated.

6.2. Concentric circle and variable beam focuses

6.2.1. Methods

The bone sample used for this investigation was harvested from pig tibia. The pulse duration measured with the autocorrelator was 170 fs. With the $f = 125$ mm lens in place, the laser power was adjusted to a maximum of 239 mW.

For Structure #1, 40 concentric circles were scanned with the beam focus aligned with the sample surface. The initial circle radius was 0 μm and each successive circle had a radius increase of 25 μm. This particular increment was chosen as it was ~5 μm less than the $1/e^2$ beam spot diameter (30.2 μm) and it ensured sufficient beam overlap between passes. Theoretically, 40 concentric circles increasing 25 μm radially each pass should result in an ablated structure ~2 mm in diameter. From the centre of Structure #1, the laser was moved 4 mm down the length of the bone and a second scanning procedure was performed. For Structure #2, the 1st layer consisted of 30 concentric circles scanned with the laser focus aligned with the sample surface. The beam was lowered 150 μm in the Z-direction and 20 concentric circles were scanned in the 2nd layer. Both circles in the 1st and 2nd layer were centered on the same point. The theoretical diameter of the 1st layer is ~1.5 mm while the 2nd layer is ~1 mm. Diagrams of the two ablation patterns are shown in Fig. 27. Both Structure #1 and Structure #2 were ablated on the same bone sample with maximum laser energy; corresponding to an average fluence of 33.4 J/cm^2. The laser scanning speed was 250 μm/s. The processing time was 8.2 min for Structure #1 and 6.5 min for Structure #2.

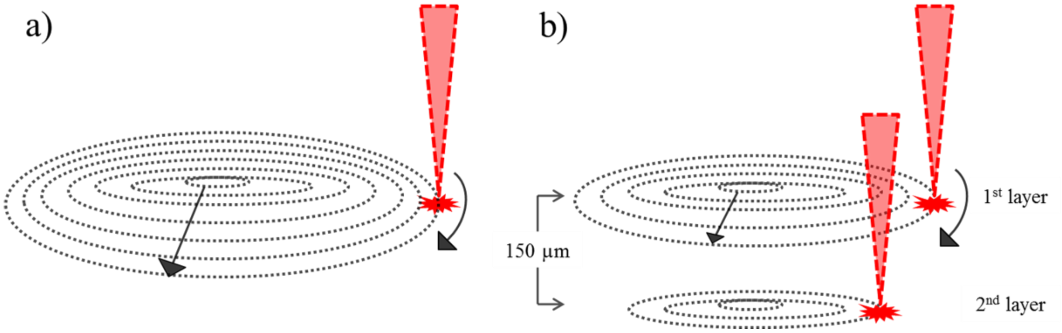

Fig. 27: Concentric circle scanning procedure for large-scale tissue removal. (a) 40 concentric circles ablated with the beam focus aligned with the sample surface – referred to as Structure #1. (b) 30 concentric circles ablated on the sample surface (1st layer) and 20 concentric circles ablated with the beam focus lowered by 150 µm (2nd layer) – Structure #2.

After completion of drilling, top-view images of the two drilling patterns were obtained using the digital hand-held microscope at 141× magnification and the bone samples were scanned in micro-CT. 3D surface reconstructions were performed on the CT slice data.

6.2.2. Discussion & Results

Top-view images taken of Structure #1 and Structure #2 with the digital hand-held microscope are shown in Fig. 28. Using the accompanying image-analysis software (DinoCapture 2.0, Dino-Lite), the outer diameter of Structure #1 was measured to be 2.12 mm. The diameter of the 1st layer in Structure #2 was measured to be 1.59 mm, while the diameter of the 2nd layer was 1.08 mm. The measured diameters of all three layers slightly exceeded their theoretical dimensions (2, 1.5, and 1 mm, respectively) likely due to the fact that the radial increase for each pass was less than the measured beam waist (30.2 µm). As well, when ablating with pulse energies that exceed the threshold for optical breakdown, the plasma formed can be characterized by a growth from the beam waist towards the incoming beam – referred to as the “moving breakdown” model [177, 178]. Based on the assumption that optical breakdown occurs at all locations where the irradiance exceeds the breakdown threshold, the width of the plasma plume resulting from sufficiently high energies would exceed the diameter of the focused beam waist as it grows into the cone angle of the incoming beam -- resulting in a region of tissue removal larger than the beam waist.

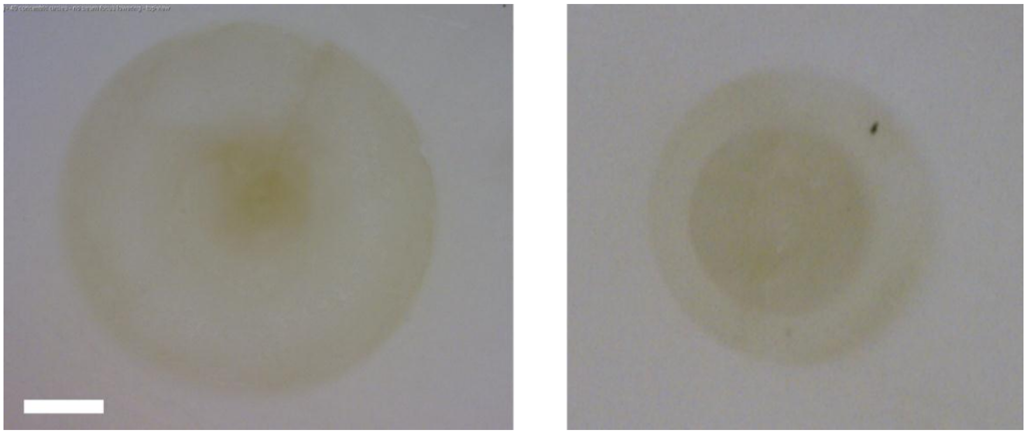

Fig. 28: Top-view screen-captures of concentric circle drilling patterns. (Left) 40 concentric circles with scanning beam in one layer – Structure #1. (Right) 30 concentric circles in 1st layer and 20 circles in 2nd layer (Δz=150 µm) – Structure #2. Images are screen-captures from digital hand-held microscope (141× magnification). (Scale bar width is 0.4 mm)

The intact bone sample containing Structures #1 and #2 was scanned in the micro-CT using the ‘step-and-shoot’ data acquisition mode. The x-ray source tube voltage was 40 kVp and current was 0.150 mA. A total of 360 input projections were obtained during scanning procedure and, after 3D image reconstruction was performed, a 512 × 512 × 512 volume of 1024 × 2048 pixels each, was created. Volume rendering was performed to create a 3D reconstruction of the drilled bone sample (Fig. 29).

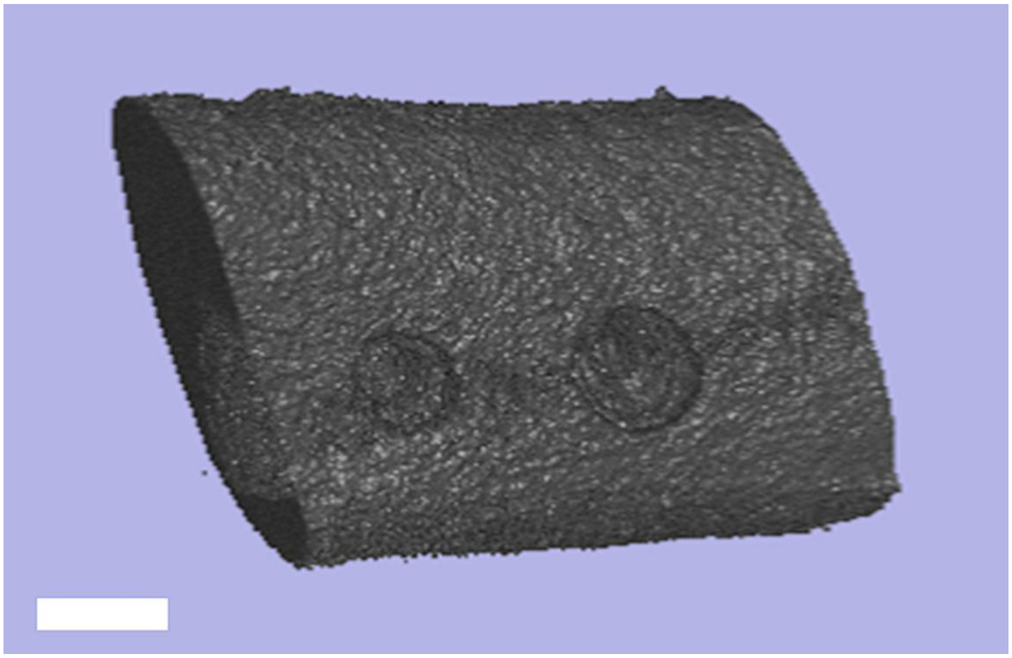

Fig. 29: 3D volume rendering of micro-CT slice data showing a porcine bone sample with concentric circle scanning Structures #1 (right) and #2 (left). Volume rendering was performed using 3DSlicer^{tm}. (Scale bar width is 2 mm).

Fig. 30 contains two side-view images of the large-scale ablated structures. For the top image in Fig. 30, the bone surface transparency was increased to allow the intact crater side-wall structures to be viewed. The bottom image in Fig. 30 is a cross-section through the centre of both craters; revealing significantly different side-profiles of the two structures. Structure #2 – with its two layers of concentric circles – appears to be somewhat cylindrical in shape. Measured using the rendering software, the total crater depth was ~2.2 mm. The crater entrance diameter (measured previously) was 1.59 mm and the diameter at the crater floor was found to be ~0.7 mm.

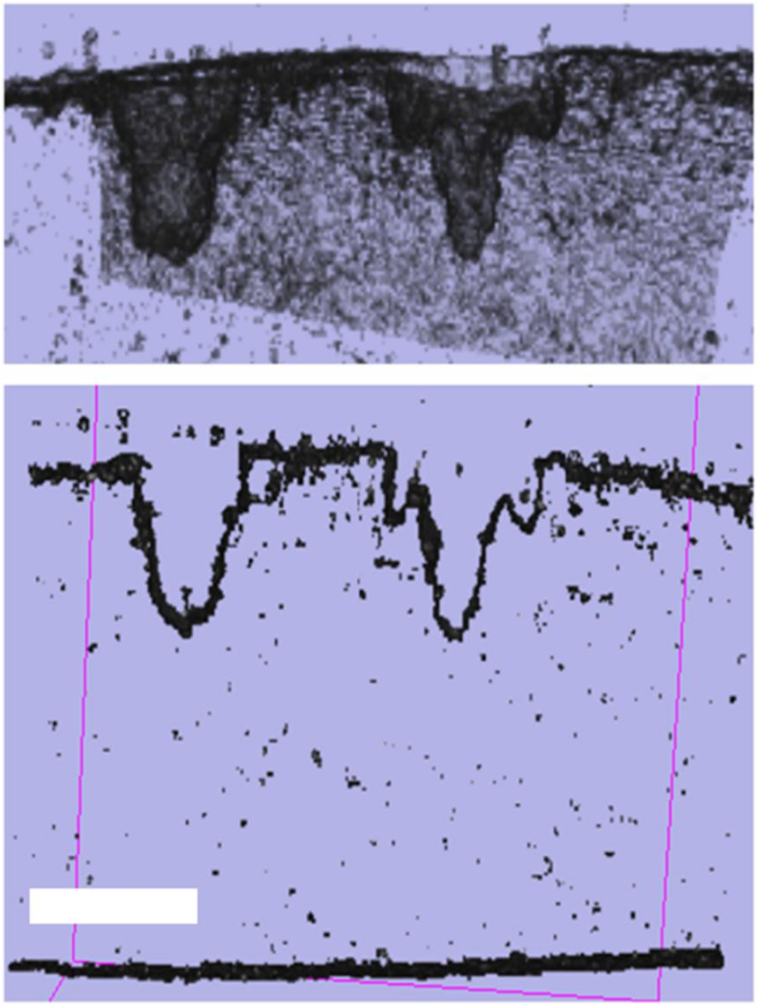

Fig. 30: Side-profiles of 3D rendered concentric-circle drilled bone sample showing Structure #1 (right crater) and Structure #2 (left crater). (Top) Partially transparent side-profile of bone sample showing side-walls of ablated structures. (Bottom) Cross-section through centre of both ablated structures. The majority of noise was removed from reconstruction images through the use of thresholding. (Scale bar width is 2 mm)

In contrast, the side-profile of Structure #1 – ablated with only one layer of concentric circles – revealed a much more complicated form. The total crater depth of ~2.4 mm was comparable to Structure #2; however, the side-walls of the single-layer structure contained peculiar side-lobes that radiated at oblique angles to the incident beam. The side-lobes can be seen in the top-view image (Fig. 28) of Structure #1 as a darkened region along the circumference of the crater. The cause of these side-lobes is unknown; especially since they were not present in the Structure #2. This fact likely eliminated the possibility of a stray beam scattered from the laser objective lens or a deviation in the spatial beam profile being responsible for the unexpected results. It is possible that the any side-lobes created during the ablation of the 1st layer in Structure #2 were removed after the scanning ablation in the 2nd layer.

Another observable difference in the two structures was the rapid change in crater width as Structure #1 increased in depth. While Structure #2 had a near columnar shape, Structure #1decreased from a measured entrance width of 2.12 mm to a width of ~1 mm at a crater depth of only ~ 0.5 mm. It is hypothesized that this structural feature was the result of beam scattering during the machining process. As seen in Fig. 31, a beam scanning along the perimeter of a large-scale structure will be scattered by the side-wall inwards towards the centre of the crater [179]. The final cylindrical shape of Structure #2 was likely the result of ablating the 2nd layer with a lesser number of concentric circles than the 1st layer and thus, minimizing the number of interactions between the beam and upper side-wall during the scanning ablation of the lower layer.

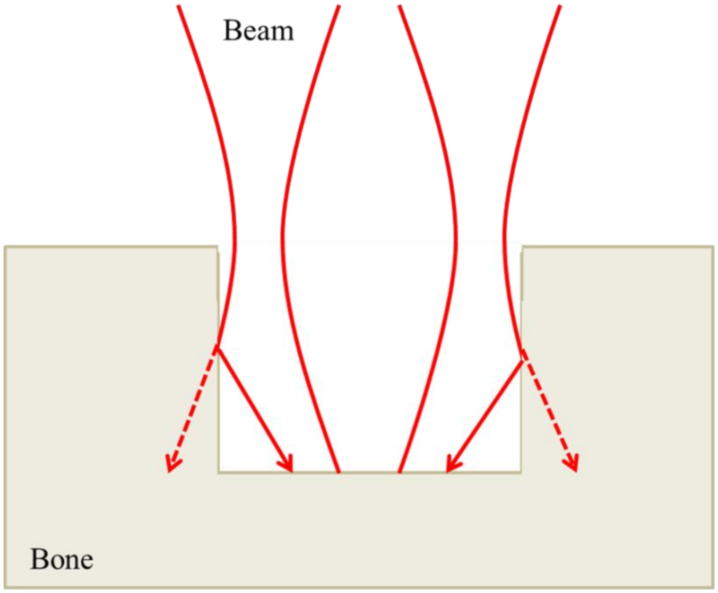

Fig. 31: Sketch of beam scattering from the crater side-wall during large-scale tissue removal. Since concentric circle structures were ablated outwards from the origin, scattering from the outer crater side-wall would cause an increase in intensity at the structure centre.

While the lowered beam focus and 2nd scanned layer did appear to have a significant effect on the final ablated structure profile, it can be concluded that a 150 μm change in beam focus position during concentric circle scanning ablation had an insignificant effect on the final crater depth. Future investigations in circular scanning will increase the separation between successive layers to possibly further increase the volume of removed tissue.

Using a 1 kHz repetition rate, the machining times for the two large-scale craters were 8.2 min and 6.5 min – presumably too long for clinical applications. With recent advances in fibre amplification technology, compact and high energy fibre lasers with pulse repetition rates >1 MHz are currently commercially available and could be used to significantly reduce the procedural time during scanned drilling.

6.3. Helical scanning

Helical drilling processes, where the laser beam circular path diameter is constant and the beam focal plane is continuously moved further into the material, has been previously utilized to remove cores from thin metals [179, 180] and semiconductors [181]. In contrast to concentric circle drilling which requires beam scanning at all interior points, helical drilling only requires scanning along the circumference of the ablation region and requires less machining time.

In clinical cases, it is not always possible to drill through the entire length of bone. In these cases, helical drilling could be used to produce a micro-pillar bone structure (Fig. 32). To be a useful drilling protocol for large-scale tissue removal, it must be possible to eventually separate these micro-pillars from the bone. It is hypothesized that the shock-waves produced during plasma-mediated ablation, combined with the characteristic brittleness of bone tissue, will result in the formation of a fracture spanning the micro-pillar. In this investigation, we experimented with helical scanning at different circular path diameters to see if micro-pillars could be produced and whether or not they could be removed.

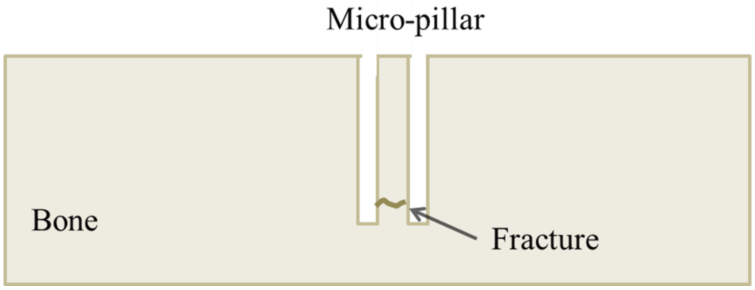

Fig. 32: Micro-pillar of bone tissue created by helical drilling. Also shown is the ideal location of a fracture spanning the micro-pillar necessary for its removal.

6.3.1. Methods

Helical scanning ablation was investigated on a cortical sample harvested from pig scapular bone. The pulse duration was stretched from 150 fs to 5 ps using the compressor optical gratings. 5 ps was used for this experiment to further explore the possibility of using 5-10 ps laser pulses in future studies (discussed in section 5.4.2). The laser power incident on the bone surface was lowered to 40 mW with the HWP– corresponding to a peak fluence of 11.2 J/cm^2.

Three separate helices with diameters of 300, 500 and 1000 μm were ablated in the bone sample at a scanning speed of 250 μm/s with a pulse repetition rate of 1 kHz. 15 full passes were made in each helix and the separation between successive passes, Δz, was 100 μm (Fig. 33). The machining times for the 300, 500 and 1000 μm helices were 0.9, 1.6 and 3.2 min, respectively.

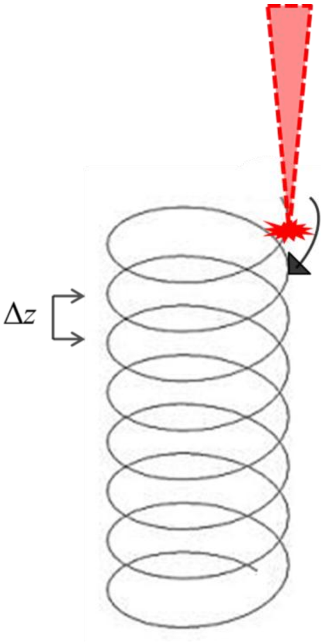

Fig. 33: Schematic of helical drilling scanning path. The helix diameters were 300, 500 and 1000μm. The separation between successive passes, Δ*z*, was 100 μm. The machining time for the three diameters ranged from 0.9-3.2 min.

6.3.2. Results & Discussion

After removing the drilling vial from the translational stage, it was noted that bone debris was absent from the chamber. Under visual inspection with white LED illumination, only the outline of the 1000 μm diameter helical scanning pattern could be faintly seen on the bone surface.

No discernable laser damage was observed on the micro-CT scans or 3D volume rendering. It should be noted that one of the limits of the scanner resolution is the 48 μm detector pitch. Since only a single continuous helix was scanned for each structure, the width of the ablated region surrounding each micro-pillar was likely comparable to the diameter of the beam waist (≈30 μm) and thus, couldn't be distinguished easily on CT slice images. Since processing times were relatively short (<4 min), a possible solution could be the re-scanning of the same helical pattern with an overall pattern diameter increase by one beam waist. Enlarging the region of cleared tissue would allow the micro-pillar margins to be viewed under CT scanning and also assist in the ejection of ablation debris.

The 1000 μm diameter micro-pillar could not be removed from the bone surface. Because ablation debris was not found in the drilling chamber, it was likely that the ablated region surrounding the micro-pillar was not fully cleared of tissue. Slowing down the scanning speed (and increasing the incident pulse number) would increase the likelihood that the micro-pillar margins were void of bone tissue.

6.4. Large-scale trabecular bone drilling

6.4.1. Methods

Concentric circle drilling was performed on a porcine trabecular bone sample harvested from the scapular bone. Care was taken to preserve the condition of the marrow and other soft tissue present within the trabecular bone during harvesting of the sample. Prior to drilling, the bone surface was lightly rinsed with water to remove blood and patted dry with paper towels.

The pulse duration was stretched with the compressor optical gratings and measured to be 5.2 ps by the autocorrelator. The laser energy was set to maximum and measured to be 150mW after focusing with the f = 125 mm objective lens. The pulse repetition rate was 1 kHz and the peak fluence was calculated to be 20.9 J/cm^2.

Three separate concentric circle structures were scanned in the surface of trabecular bone. For each pattern, the scanned circle radius was increased by 20 μm (<beam waist) after each pass. Structure #1 consisted of a single layer of 30 concentric circles with the laser focal plane aligned with the sample surface. Structure #2 consisted of two layers; both consisting of 30 concentric circles. The first layer was scanned with the beam aligned with the sample surface and the second was scanned after the beam focus was lowered 200 μm into the sample. Structure #3 had the same overall pattern as Structure #2 but was scanned with 40 concentric circles in both layers.

6.4.2. Results & Discussion

Micro-CT cross-sectional slices of the three scanned structures are shown in Fig. 34. Crater depths and diameters were measured using image analysis software (ImageJ, NIH). Due to the diffuse nature of trabecular bone, the crater sidewalls and margins were difficult to distinguish and, as a result, measurements are only approximates. The results are listed in Table 3.

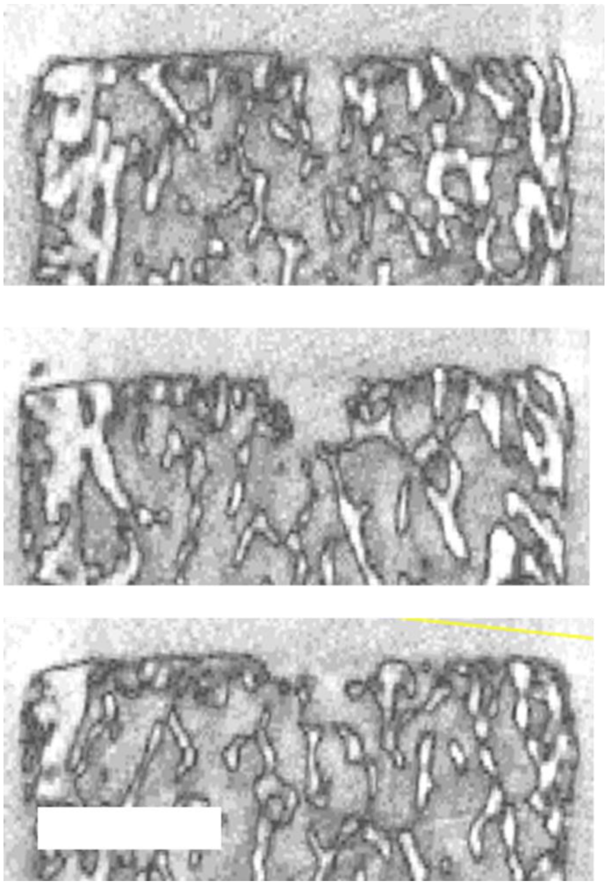

Fig. 34: Micro-CT cross-sectional slices of trabecular bone sample showing structures ablated using concentric circle scanning. (Top) 30 concentric circles with laser focal plane aligned with surface. (Middle) Two layers of 30 concentric circles separated by 200µm. (Bottom) Two layers of 40 concentric circles separated by 200µm. (Scale bar width is 2 mm)

Table 3: Approximate crater dimensions of concentric circle-scanned ablation patterns in porcine trabecular bone. The scanned layers were separated by 200µm.

		Depth (mm)[a]	Maximum width (mm)[a]
Structure #1	30 concentric circles (one layer)	1.0	0.5
Structure #2	30 concentric circles (two layers)	0.6	1.0
Structure #3	40 concentric circles (two layers)	0.8	1.1

[a] Depth and width measurements are only approximate due to the diffuse structure of the ablated material

From the crater dimensions, it can be seen that large-scale tissue removal is possible in trabecular bone with concentric circle scanning. However, the ablative precision is much less than that observed in cortical bone (Section 6.2). With the same number of concentric circles (30), Structures #1 and #2 had significantly different widths (0.5 mm and 1.0 mm, respectively). Both structures had maximum widths smaller than the scanned area - the width of a structure ablated with 30 concentric circles (with a 20 µm radial increase between passes) should be about 1.2 mm. As well, the final crater depths do not follow the same trend seen in Section 5.5 with lowered beam focuses. The final depth of Structure #1 is greater than Structures #2 and #3 even though these two craters each had a layer scanned 200 µm below the bone surface.

Observed differences in the ablative precision and volume of tissue removal between cortical and trabecular bone were not unexpected with regard to the dissimilarity of their composition, as well as their mechanical and thermophysical properties. The variation in trabecular bone crater depth and width between similar ablated structures was likely due to the diffuse nature of trabecular bone. With an porosity much greater than cortical bone, trabecular bone is much more susceptible to fracturing during ablation [55]. Individual trabeculae are usually on the order of 200 μm wide and 1 mm long [51] therefore, during large-scale scanning ablation, pulses incident on trabecular bone will either interact directly with a trabeculae or with the surrounding marrow – resulting in an ablation process that is in a state of constant change.

The final trabecular bone crater volumes were less than those observed in cortical bone (Section 6.2). This effect is most likely the result of the different pulse durations used between the two experiments. For the trabecular bone large-scale drilling, the pulse duration was 5.2 ps while 170 fs was used for cortical bone. As observed in Section 5.4, the tissue removal rate decreases as pulses get stretched from femtoseconds to 5-10 picoseconds. As well, due to the absorbing properties of the soft bone marrow present within the pores, trabecular bone is less susceptible to shockwave propagation during pulsed laser ablation [182].

To detect the occurrence of laser-induced damage in the trabeculae outside of the directly-scanned volume, future investigations should perform a full CT scan before laser irradiation of trabecular bone. By comparing structural information before and after irradiation, any peripheral damage to neighbouring trabeculae could be detected.

6.5. Large-scale tissue removal with mimicked Nd:YAG laser parameters

6.5.1. Introduction

Current picosecond Nd:YAG lasers are compact, turnkey, affordable, and allow for high peak pulse powers. As a result, they appear to be suitable for use in hard tissue ablation. In this investigation, the Ti:Sapphire laser system was configured to simulate the beam output of a commercially-available Nd:YAG laser (Compiler 1064, Passat). Using the same focusing and machining scheme, the mimicked Nd:YAG beam was used to ablate large-scale structures in bone.

The pulse duration, individual pulse energy, and repetition rate of the ultrafast laser system were adjusted to match the specifications of the Compiler 1064 laser Nd:YAG laser. The wavelength of the Ti:Sapphire laser was not adjusted to match that of the Nd:YAG laser (1064 nm) due to the weak dependence of incident wavelength on optical breakdown [11]. Previous studies in biological tissue ablation have found only slight increases in the threshold fluence as the wavelength increases from 800-1000 nm, followed by a plateau for longer wavelengths [183].

6.5.2. Methods

The pulse duration was stretched to 8 ps and the laser power was lowered to 32.5 mW. With a repetition rate of 200 Hz, the individual pulse energy out of the amplifier was 162.5 μJ. After passing through the focusing objective and the drilling chamber window, the pulse energy was measured to be 130 μJ.

Concentric circle scanning was performed to create three separate large-scale cylindrical structures in the surface of a porcine cortical bone sample. All three patterns were ablated using 30 concentric circles with a radial increase of 20 μm per pass. The scanning speed was 250 μm/s. Only a single layer of concentric circles was scanned at the surface of the bone for the first structure while the second structure consisted of two layers of 30 circles and the third structure consisted of three layers. The layer separation was 500 μm. After drilling, the bone sample was scanned in the micro-CT and a 3D volume rendering was produced.

6.5.3. Results & Discussion

A top-view screen-capture of the 3D rendered bone sample is shown in Fig. 35. The three-layered (right-most) and two-layered (second-from-right) cylindrical structures can be seen easily. However, the single-layered structure (left) can only be faintly discerned from the CT images. In general, the edges of the structures appear to be well-defined and devoid of significant surface fractures.

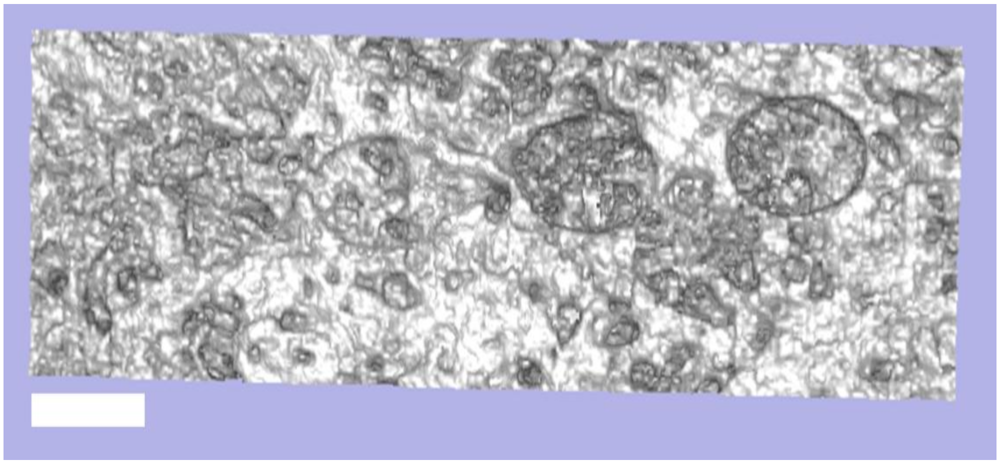

Fig. 35: Top-view of cortical bone sample ablated with mimicked Nd:YAG laser parameters. Three cylindrical structures can be seen: (R to L) three layered cylinder, two layered cylinder and (faint) single-layer cylinder. (Scale bar = 1mm)

A cross-sectional image showing the side-profiles of the 2 and 3 layered structures is shown in Fig. 36. The most notable feature of these structures is their shallow final depths. In the scanning of these two structures, the lower layers were located at a depth of 500 μm and 1000 μm for the 2- and 3-layer structures, respectively, yet both crater depths are <200 μm deep.

With a pulse repetition rate of 200 Hz and scanning speed of 250 μm/s, the number of pulses per incident spot during scanning was calculated to be 24 – five times fewer incident pulses than used to reach ablation depths of 2 mm in Section 6.2. To achieve larger-scale crater depths (>1 mm) with a Nd:YAG laser and concentric circle ablation, the scanning speed will need to be reduced. This would increase the processing time for each layer; which currently stands at approximately 2 minutes per layer.

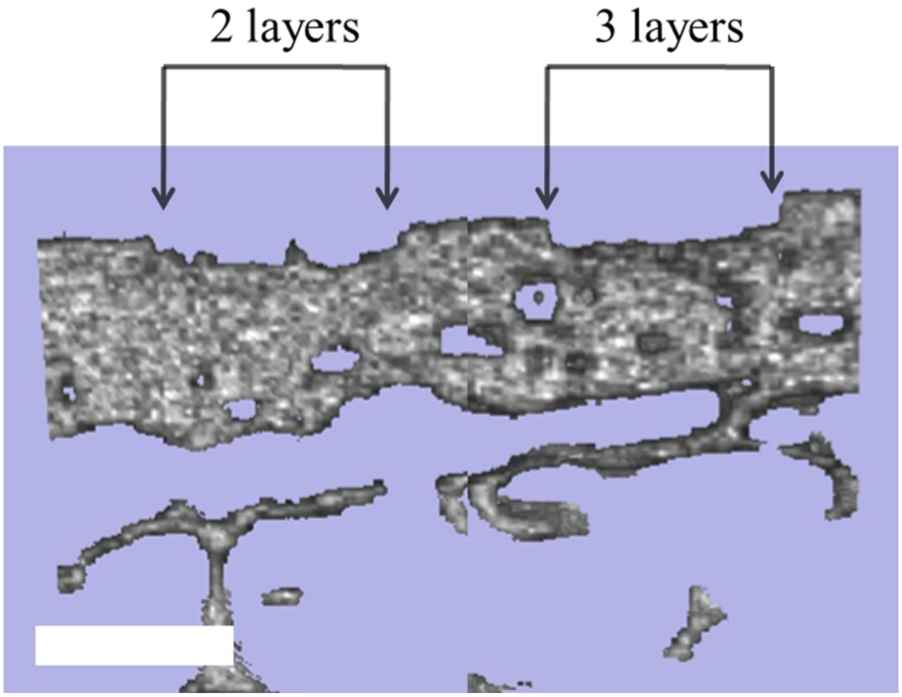

Fig. 36: Screen-capture of cross-sectional profile of the 2-layered (left) and 3-layered (right) cylindrical structures. The single-layer profile could not be discerned from the surface roughness of the bone. The dense upper layer is cortical bone while the sporadic structures in the lower region of the image are individual bone trabeculae. (Scale bar width is 1 mm)

Even though the beam focal plane was lowered 500 μm and 1000 μm the two- and three-layered structures, respectively, there did not appear to be any evidence of laser-induced damage at those tissue depths (Fig. 36). Since the scanning of the initial layer (aligned with the bone surface) was unable to remove tissue up to the desired depth of 500 μm, the incident beam then had to pass through intact bone before reaching the second and third scanning layers. The resulting beam attenuation would have considerably reduced the laser intensity at these greater depths.

7. CONCLUSIONS

Mechanical cutting tools, such as saws and drills, can cause significant damage to bone tissue when used in orthopaedic surgical procedures. The friction between the cutting interface and bone can create temperatures sufficiently high to denature or char tissue, and the cutting precision is limited by the thickness of the blade or drill bit. Ultrashort pulsed lasers have shown promise as an eventual replacement for the mechanical bone cutting tools currently used in clinical practice. Ultrashort laser pulses have been shown to produce highly efficient tissue removal while resulting in only minimal thermal damage to the surrounding regions. As well, laser ablation also has the added benefits of: (i) minimal mechanical vibration, (ii) non-contact intervention, and (iii) ability to focus to very small ablative regions. To incorporate laser technology into orthopaedic surgical suites, a number of multi-disciplinary tasks will need to be accomplished; such as the development of a robotic delivery arm or real-time feedback sensors. The specific task undertaken in this thesis was the characterization of laser-specific parameters and drilling protocols for the purpose of bone ablation.

Unaltered porcine bone samples were used during the course of this study. Laser ablation strongly depends on the material composition and properties of the sample – a polished bone surface and natural bone surface could produce considerably different ablative results. For example, sanding the bone surface can increase specular reflection, which could result in removal rates or depths different than that in surgical scenarios, where smoothing the bone would be unfeasible.

The ablation threshold is the minimum energy fluence required to initiate material removal from a surface. To prevent excess energy deposition and resultant collateral damage during laser bone ablation, it was important to determine the tissue-specific threshold. Using the D^2 technique, the ablation threshold was found to vary slightly depending on the incident pulse number. This indicated the presence of a damage accumulation effect referred to as incubation. Using a power law model, the material-specific incubation coefficient – which characterizes the degree of incubation – was determined.

A characterization of specific drilling parameters was performed to investigate their effect on the ablation of hard tissue. The ablation rate was evaluated at various laser pulse energies and pulse durations. The influence of incident pulse number and beam focus position on final ablated depth was also investigated. With an understanding of the relation between different laser and drilling parameters and the final tissue state, we can devise specific laser configurations and drilling strategies to optimize drilling efficiency and reduce procedural times.

To successfully replace mechanical cutting and drilling tools in orthopaedic surgery, ultrashort pulsed lasers will require the ability to remove relatively large volumes of bone tissue in appropriate operating times. An investigation into large-scale drilling procedures was performed using micro-CT to characterize ablated volumes. Concentric circle scanned ablation was evaluated in combination with re-focusing of the beam on different z-planes; in both cortical and trabecular bone samples. A helical spiral drilling strategy could significantly lower machining times; however, was found not to produce significant material removal. Although large-scale scanning ablation with a mimicked Nd:YAG laser was found to remove only a modest volume of tissue (compared to the typical Ti:Sapphire configuration), the benefits of 5-10 ps laser ablation (i.e affordability, compactness, fibre-coupling) make the ultrafast Nd:YAG laser an intriguing possibility for future applications.

8. REFERENCES

1. L. R. Solon, R. Aronson, and G. Gordon, "Physiological implications of laser beams," Science **134**, 1506-1508 (1961).
2. T. H. Maiman, "Stimulated optical radiation in ruby," Nature **187**, 493-494 (1960).
3. C. J. Campbell, K. S. Noyori, M. C. Rittler, and C. J. Koester, "Intraocular temperature changes produced by laser coagulation," Acta Ophthalmol **41**, 22-31 (1963).
4. R. H. Stern and R. F. Sognnaes, "Laser beam effect on dental hard tissues," J Dent Res **43**, 873 (1964).
5. L. Goldman, P. Hornby, P. Meyer, and B. Goldman, "Impact of the laser on dental caries," Nature **203**, 417 (1964).
6. U. Kroitzsch, G. Laufer, E. Egkher, G. Wollenek, and R. Horwarth, "Experimental photoablation of meniscus cartilage by excimer laser energy: a new aspect of meniscus surgery," Arch Orthop Trauma Surg **108**, 44-48 (1989).
7. R. J. Schultz, S. Krishnamurthy, W. Thelmo, J. E. Rodriguez, and G. Harvey, "Effects of varying intensities of laser energy on articular cartilage: a preliminary study," Lasers Surg Med **5**, 577-588 (1985).
8. T. A. Evans, T. F. Winters, N. A. Palmeri, and A. E. Joiner, "Laser-assisted arthroscopic meniscal repair," South Med J **80**, N9 (1987).
9. G. R. Gropper, J. H. Robertson, and G. McClellan, "Comparative histological and radiographic effects of CO2 laser versus standard surgical anerior cervical discectomy in the dog," Neurosurgery **14**, 42-47 (1984).
10. R. C. Perkins, "Laser stapedotomy for otosclerosis," Laryngoscope **90**, 228-241 (1980).
11. A. Vogel and V. Venugoplan, "Mechanisms of Pulsed Laser Ablation of Biological Tissues," Chem Rev **103**, 577-644 (2003).
12. R. S. Hodgson and D. F. Wilson, "Argon laser stapedotomy," Laryngoscope **101**, 230-233 (1991).
13. S. G. Lesinski and J. A. Stein, "CO2 laser stapedotomy," Laryngoscope **99**, 20-24 (1989).
14. R. C. Nuss, R. L. Fabian, R. Sarkar, and C. A. Puliafito, "Infrared laser bone ablation," Lasers Surg Med **8**, 381-391 (1988).
15. M. Niemz, *Laser-tissue interactions: Fundamentals and applications* (Springer-Verlag Berlin and Heidelberg GmbH & Co., 1996).
16. R. L. Fork, I. Greene, and C. V. Shank, "Generation of optical pulses shorter than 0.1 ps by colliding pulse mode locking," Appl Phys Lett **38**, 671-672 (1991).
17. C. Rulliere, *Femtosecond laser pulses - principles and experiments* (Springer-Verlag Inc., New York, 1998).
18. P. D. Byers, "Solitary benign osteoblastic lesions of bone," Cancer **22**, 43-57 (1968).
19. W. G. Ward, J. J. Eckardt, S. Shayestehfar, J. Mirra, T. Grogan, and W. Oppenheim, "Osteoid osteoma diagnosis and management with low morbidity," Clin Orthop Relat Res **291**, 229-235 (1993).
20. R. Roy-Camille, G. Saillant, and C. Mazel, "Internal fixation of the lumbar spine with pedicle screw plating," Clin Orthop Relat Res **203**, 7-17 (1986).
21. A. P. Amar, D. Larsen, and G. Teitalbaum, "Percutaneous spinal interventions," Neurosurg Clin N Am **16**, 561-568 (2005).
22. S. Erkan, B. Hsu, C. Wu, A. A. Mehbod, J. Perl, and E. E. Transfeldt, "Alignment of pedicle screws with pilot holes: can tapping improve screw trajectory in thoracic spines?," Eur Spine J **19**, 71-77 (2010).
23. S. A. Rath, S. Moszko, P. M. Schaffner, G. Cantone, V. Braun, H. P. Richter, and G. Antoniadis, "Accuracy of pedicle screw insertion in the cervical spine for internal fixation using frameless stereotactic guidance," J Neurosurg Spine **8**, 237-245 (2008).
24. S. C. Ludwig, D. L. Kramer, R. A. Balderston, A. R. Vaccaro, K. F. Foley, and T. J. Albert, "Placement of pedicle crews in the human cadaveric cervical spine," Spine (Phila Pa 1976) **25**, 1655-1667 (2000).
25. D. Zumofen, L. Regli, M. Levivier, and N. Krayenbuhl, "Chronic subdural hematomas treated by burr hole trepanation and a subperiostal drainage system," Neurosurgery **64**, 1116-1121 (2009).
26. M. Sanna, H. Sunose, F. Mancini, A. Russo, and A. Taibah, *Middle ear and mastoid microsurgery* (Thieme, 2003).
27. P. Kylen, J. E. Stjernvall, and S. Arlinger, "Variables affecting the drill-generated noise levels in ear surgery," Acta Otolaryngol **84**, 252-259 (1977).

28. B. Girard, D. Yu, M. R. Armstrong, B. C. Wilson, C. M. Clokie, and R. J. Miller, "Effects of femtosecond laser irradiation on osseous tissues," Laser Surg Med **39**, 273-285 (2007).
29. K. Firoozbakhsh, M. S. Moneim, E. Mikola, and S. Haltom, "Heat generation during ulnar osteotomy with microsagittal saw blades," Iowo Orthop J **23**, 46-50 (2003).
30. S. Sevitt, "Early and delayed oedema and increase in capillary permeability after burns of the skin," J Pathol Bacteriol **75**, 27-37 (1958).
31. F. Hoegel, M. C.A., R. Peter, U. Pfister, and N. P. Suedkamp, "Bone debris: dead matter or vital osteoblasts," J Trauma **56**, 363-367 (2004).
32. A. R. Eriksson and T. Albertktsson, "The effect of heat on bone regeneration: an experimental study in the rabbit using the bone growth chamber," J Oral Maxillofac Surg **42**, 705-711 (1984).
33. C. Scholz and M. Grothves-Spork, Angewandte Laseredizin IIII (Ecomed, Landsberg, Lech, 1992).
34. J. Christie, "Surgical heat injury of bone," Injury **13**, 188-190 (1981).
35. H. W. Wevers, E. Espin, and T. D. V. Cooke, "Orthopaedic saw blades: A case study," J Arthroplasty **2**, 43-46 (1987).
36. S. Stubinger, "Advances in bon surgery: the Er:YAG laser in oral surgery and implant dentistry," Clin Cosmet Investig Dent **2**, 47-62 (2010).
37. M. Stanislawki, J. Meister, T. Mitra, M. M. Ivanenko, K. Zanger, and P. Hering, "Hard tissue ablation with a free running Er:YAG and a Q-switched CO2 laser: a comparative study," Appl Phys B **72**, 1-6 (2000).
38. K. L. Wiggins and S. Malkin, "Drilling of bone," J Biomech **9**, 553-559 (1976).
39. J. M. Hicks, A. Singla, F. H. Shen, and V. Arlet, "Complications of pedicle screw fixation in scoliosis surgery: a systematic review," Spine (Phila Pa 1976) **35**, E465-E470 (2010).
40. T. Laine, T. Lund, M. Ylikoski, J. Lohikoski, and D. Schlenzka, "Accuracy of pedicle screw insertion with and without computer assistance: a randomised controlled clinical study in 100 consecutive patients," Eur Spine J **9**, 235-240 (2000).
41. K. Takamori, H. Furukawa, Y. Morikawa, T. Katayama, and S. Watanabe, "Basic study on vibrations during tooth preparations caused by high-speed drilling and Er:YAG laser irradiation," Laser Surg Med **32**, 25-31 (2003).
42. I. Anic, I. Miletic, S. J. Krmek, J. Borcic, and S. P. Pezelj-Ribaric, "Vibrations during erbium:yttrium-aluminum-garnet laser irradiation," Lasers Med Sci **24**, 697-701 (2009).
43. J. Neev, L. B. Da Silva, M. D. Feit, M. D. Perry, A. M. Rubenchik, and B. C. Stuart, "Ultrashort pulse lasers for hard tissue ablation," IEEE J Sel Top Quant **2**, 790-800 (1996).
44. Y. Liu and M. Niemz, "Ablation of femural bone with femtosecond laser pulses - a feasibility study," Lasers Med Sci **22**, 171-174 (2007).
45. S. Hall, *Basic Biomechanics*, 5th ed. (McGraw-Hill Humanities/Social Sciences/Languages, 2007).
46. Courseweb, "Histology of cartilage and bone", retrieved 2011, http://www.courseweb.uottawa.ca/medicine-histoloy/english/muscuoloskeletal/default.htm#Bone.
47. H. Gray, *Anatomy of the human body*, 20th ed. (Lea & Febiger, Philadelphia, 1918).
48. J. Currey, *The mechanical adaptations of bones* (Princeton Univ Pres, 1984).
49. N. M. Hancox, *Biology of bone* (Cambridge Univ Pr, New York, 1972).
50. A. Ascenzi and E. Bonucci, "The mechanical properties of the osteon in relation to its structural organisation," in *Chemistry and molecular biology of the intercellular matrix*, E. D. Balazs, ed. (Academic Press, New York, 1970).
51. J. Krapstrup, F. Melsen, and L. Mosekilde, "Thickness of lamellae in normal iliac trabecular bone," Metab Bone Dis Rel Res **4**, 291-295 (1983).
52. P. Augat and S. Schorlemmer, "The role of cortical bone and its microstructure in bone strength," Age and Ageing **35-S2**, ii27-ii31 (2006).
53. C. H. Turner, A. Chandran, and R. M. V. Pidaparti, "The anisotropy of osteonal bone and its ultrastructural implications," Bone **17**, 85-89 (1995).
54. C. A. Cefalu, "Is bone mineral density predictive of fracture risk reduction?," Clin Med Res Opin **20**, 341-349 (2004).
55. Y. N. Yeni, C. U. Brown, Z. Wang, and T. L. Norman, "The influence of bone morphology on fracture toughness of the human femur and tibia," Bone **21**, 453-459 (1997).
56. P. Zioupos, "Accumulation of in-vivo fatigue microdamage and its relation to biomechanical properties in ageing human cortical bone," J Microsc **201**, 270-278 (2001).
57. B. Martin, "Aging and strength of bone as a structural material," Calcif Tissue Int **53**, S34-S40 (1993).
58. J. Currey, *Bone: structure and mechanics* (Princeton Univ Pres, 2006).

59. X. Wang, R. A. Bank, J. M. TeKoppele, and C. M. Agrawal, "The role of collagen in determining bone mechanical properties," J Orthop Res **19**, 1021-1026 (2001).
60. A. H. Burstein, D. T. Reilly, and M. Martens, "Aging of bone tissue: mechanical properties," J Bone Joint Surg **58**, 82-86 (1976).
61. M. Ivanenko, M. Werner, S. Afilal, M. Klasing, and P. Hering, "Ablation of hard bone tissue with pulsed CO2 lasers," Med Laser Appl **20**, 13-23 (2005).
62. G. C. Willenborg, "Dental laser applications: emerging to maturity," Lasers Surg Med **9**, 309-313 (1989).
63. J. Neev, L. L. Liaw, D. V. Raney, J. T. Fujishige, P. D. Ho, and M. W. Berns, "Selectivity, efficiency, and surface characteristics of hard dental tissues ablated with ArF pulsed excimer lasers," Lasers Surg Med **11**, 499-510 (1991).
64. E. Quintana, F. Marques, I. Roca, V. Torres, and J. Salgado, "Some morphologic changes induced by Nd:YAA laser on the noncoated enamel surface: a scanning electron microscopy study," Lasers Surg Med **12**, 131-136 (1992).
65. Y. H. Moore, "Laser energy in orthopaedic surgery," in *Int Congr Orthopaedic Surgeons*, 1973), 1077.
66. L. Clayman, T. Fuller, and H. Beckham, "Healing of continuous-wave and rapid superpulsed, carbon dioxide, laser-induced bone defects," J Oral Surg **36**, 932-937 (1978).
67. I. A. Small, T. P. Osborn, T. Fuller, M. Hussain, and S. Kobernick, "Observations of carbon dioxide laser and bone nur in the osteotomy of the rabbit tibia," J Oral Surg **37**, 159-166 (1979).
68. J. S. Nelson, A. Orenstein, L. H. Liaw, R. B. Zavar, S. Gianchandani, and M. W. Berns, "Ultraviolet 308-nm eximer laser ablation of bone: An acute and chronic study," Appl Opt **28**, 2350-2357 (1989).
69. C. Gonzalez, W. P. Van De Merwe, M. Smith, and L. Reinisch, "Comparison of the Erbium-Yttrium Aluminum Garnet and Carbon Dioxide Lasers for In Vitro Bone and Cartilage Ablation," Laryngoscope **100**, 14-17 (1990).
70. J. Lustmann, M. Ulmansky, A. Fuxbrunner, and A. Lewis, "193-nm excimer laser ablation of bone," Laser Surg Med **11**, 51-57 (1991).
71. M. Forrer, M. Frenz, V. Romano, H. J. Altermatt, H. P. Weber, A. Silenok, M. Istomyn, and V. I. Konov, "Bone-ablation mechanism using CO2 lasers of different pulse duration and wavelength," Appl Phys B **56**, 104-112 (1993).
72. G. M. Peavy, L. Reinisch, J. T. Payne, and V. Venugopalan, "Comparison of cortical bone ablations by using infrared laser wavelengths 2.9 to 9.2 um," Lasers Surg Med **25**, 421-434 (1999).
73. M. M. Ivanenko and P. Hering, "Wet bone ablation with mechanically Q-switched high-repetition-rate CO2 laser," Appl Phys B **67**, 395-397 (1998).
74. G. M. Hale and M. R. Querry, "Optical constants of water in the 200-nm to 200-um wavelength region," Appl Opt **12**, 555-563 (1973).
75. I. V. Yannas, "Collagen and gelatin in the solid state," J Macromol Sci-Revs Macromol Chem **C7**, 49-104 (1972).
76. E. P. Paschalis, E. DiCarlo, F. Betts, P. Serman, R. Mendelsohn, and A. L. Boskey, "FTIR microspectroscopic analysis of human osteonal bone," Calcif Tissue Int **59**, 480-487 (1996).
77. F. A. Miller and C. H. Wilkins, "Infrared spectra and characteristic frequencies of inorganic ions," Anal CHem **24**, 1253-1254 (1952).
78. B. O. Fowler, "Infrared studies of apaties. I. Vibrational assignments for calcium, strontium, and barium hydroxyapatites utilizing isotopic substitution," Inorgan Chem **13**, 194-207 (1974).
79. P. N. Prasad, *Introduction to biophotonics* (Wiley-Interscience, New York, 2003).
80. F. Bevilacqua, D. Piguet, P. Marquet, J. D. Gross, B. J. Tromberg, and C. Depeursinge, "In vivo local determination of tissue optical properties: applications to human brain," Appl Opt **38**, 4939-4950 (1999).
81. W. C. Lin, M. Motamedi, and A. J. Welch, "Dynamics of tissue optics during laser heating of turbid media," Appl Opt **35**, 3413-3420 (1996).
82. J. P. Ritz, A. Roggan, C. T. Germer, C. Isbert, G. Muller, and H. J. Buhr, "Continuous changes in the optical properties of liver tissue during laser-induced interstitial thermotherapy," Lasers Surg Med **28**, 307-312 (2001).
83. J. T. Walsh and J. P. Cummings, "Effect of the dynamic optical properties of water on midinfrared laser ablation," Laser Surg Med **15**, 295-305 (1994).
84. I. F. Cilesiz and A. J. Welch, "Light dosimetry - Effects of dehydration and thermal-dmage on the optical properties of the human aorta," Appl Opt **32**, 477-487 (1993).
85. A. M. Weiner, *Utrafast optics* (John Wiley & Sons, Inc., 2009).

86. R. Srinivasan, "Ablation of polymers and biological tissue by ultraviolet lasers," Science **234**, 559 (1986).
87. H. H. G. Jellinek and R. Srinivasan, "Theory of etching of polymers by far-ultraviolet high-intensity pulsed laser- and long-term irradiation," J Phys Chem **88**, 3048-3051 (1984).
88. A. Scheinin and S. Kantola, "Laser-induced effects on tooth structure. I. Crater production with a CO2 laser," Acta Odontol Scand **27**, 173-179 (1969).
89. R. Boehm, J. Rich, J. Webster, and S. Janke, "Thermal-stress effects and surface cracking associated with laser use on human teeth," Mech Eng **100**, 100 (1977).
90. B. O. Fowler and S. Kuroda, "Changes in heated and in laser-irradiated human tooth enamel and their probable effects in solubility," Calcif Tissue Int **38**, 197-208 (1986).
91. A. Charlton, M. R. Dickinson, T. A. King, and A. J. Freemont, "Erbium-YAG and holmium-YAG laser ablation of bone," Laser Med Sci **5**, 365-373 (1990).
92. R. Srinivasan and V. Mayne-Baton, "Self developing photoetching of poly(ethylene terephthalate) films by far ultraviolet excimer laser radiation," Appl Phys Lett **41**, 576-577 (1982).
93. E. Reichel, H. Schmidt-Kloiber, H. Schoffmannm, G. Dohr, and A. Eherer, "Interaction of short laser pulses with biological structures," Opt Laser Technol **19**, 37-41 (1987).
94. R. Jahn, A. Bleckmann, E. Duczynski, G. Huber, W. Kierse, B. Struve, and K. H. Jungbluth, "Thermal side effects after use of the pulsed IR laser on mensicus and bone tissue," Unfallchirurg **20**, 1-10 (1994).
95. C. Haffner, M. Folwaczny, R. Hickel, and H. H. Horch, "Ablation of temporomandibular joint structures of a pig with fibre-guided 308 nm excimer laser light - an in vitro investigation," J Cranio Maxill Surgery **32**, 360-364 (2004).
96. G. A. Peyman, J. R. Kuszak, K. Weckstrom, I. Mannonen, E. Viherkoski, and L. Auterinen, "Effects of XeCl excimer laser on the eyelid and anterior segment structures," Arch Ophthalmol **104**, 118-122 (1986).
97. K. Mitsudo and H. Yamamoto, "Laser coronary angioplasty," Nippon Rinsho **61**, 540-548 (2003).
98. B. Choi and A. J. Welch, "Analysis of thermal relaxation during laser irradiation of tissue," Laser Surg Med **29**, 351-359 (2001).
99. J. R. Hayes and M. L. Wolbarsht, "Thermal model for retinal damage induced by pulsed lasers," Aerospace Med **39**, 474-480 (1968).
100. M. J. C. van Gemert and A. J. Welch, "Time constants in thermal laser medicine," Laser Surg Med **9**, 405-421 (1989).
101. R. R. Gattass, L. R. Cerami, and E. Mazur, "Micromachining of bulk glass with bursts of femtosecond laser pulses at variable repetition rates," Opt Express **14**, 5279-5284 (2006).
102. A. Aoki, I. Ishikawa, T. Yamada, M. Otsuki, H. Watanabe, J. Tagami, and H. Yamamoto, "Comparison between Er:YAG laser and conventional technique for root caries treatement in vitro," J Dent Res **77**, 1404-1414 (1998).
103. R. Hibst and U. Keller, "Experimental studies of the application of Er:YAG laser on dental hard substances: I. Measurement of the ablation rate," Lasers Surg Med **9**, 338-344 (1989).
104. H. W. Kang, J. Oh, and A. J. Welch, "Investigations on laser hard tissue ablation under various environments," Phys Med Biol **53**, 3381-3390 (2008).
105. M. Abu-Serriah, H. Critchlow, C. J. Whitters, and A. Ayoub, "Removal of partially erupted third molars using an erbium (Er):YAG laser: A randomized controlled clinical trial," Br J Oral Maxillofac Surg **42**, 203-208 (2004).
106. N. M. Fried and D. Fried, "Comparison of Er:YAG and 9.6-um TE CO2 lasrs for ablation of skull tissue," Lasers Surg Med **28**, 335-343 (2001).
107. K. U. Lewandroski, C. Lorente, K. T. Schomacker, T. J. Flotte, J. W. Wilkes, and T. F. Deutsch, "Use of the Er:YAG laser for improved plating in maxillofacial surgery: Comparison of bone healing in laser and drill osteotomies," Lasers Surg Med **19**, 40-45 (1996).
108. J. S. Nelson, L. Yow, and L. H. Liaw, "Ablation of bone and methacrylte by a prototype mid-infrared erbium-YAG laser," Lasers Surg Med **8**, 494-500 (1988).
109. K. M. Sasaki, A. Aoki, S. Ichinose, and I. Ishikawa, "Ultrastructural analysis of bone tissue irradiated by Er:YAG laser," Lasers Surg Med **31**, 322-332 (2002).
110. M. D. McKee, "Effects of CO2 laser irradiation in vivo on rat alveolar bone and incisor enamel, dentin, and pulp," J Dent Res **72**, 1406-1417 (1993).
111. M. Frentzen, W. Gotz, M. Ivanenko, S. Afilal, M. Werner, and P. Hering, "Osteotomy with 80-mu s CO2 laser pulses - Histological results," Lasers Med Sci **18**, 119-124 (2003).

112. J. Siegel, D. Puerto, W. Gawelda, G. Bachelier, J. Solis, L. Ehrentraut, and J. Bonse, "Plasma formation and structural modification below the visble ablation threshold in fused silica upon femtosecond laser irradiation," Appl Phys Lett **91**, 082902 (2007).
113. A. Vogel, J. Noack, K. Nahen, D. Theisen, S. Busch, U. Parlitz, D. X. Hammer, G. D. Noojin, B. A. Rockwell, and R. Birngruber, "Energy balance of optical breakdown in water at nanosecond to femtosecond time scales," Appl. Phys. B-Lasers Opt. **68**, 271-280 (1999).
114. V. Margetic, T. Ban, E. Leis, K. Niemax, and R. Hergenroder, "Hydrodynamic expansion of a femtosecond laser produced plasma," Spectroc. Acta Pt. B-Atom. Spectr. **58**, 415-425 (2003).
115. A. Vogel, *Optical breakdown in water and ocular media, and its use for intraocular photodisruption* (Shaker, Aachen, 2001).
116. D. Stern, R. W. Schoelein, C. A. Puliafito, E. T. Dobi, R. Birngruber, and J. G. Fujimoto, "Corneal ablation by nanosecond, picosecond, and femtosecond lasers at 532 and 625 nm," Arch Ophthalmol **107**, 587-592 (1989).
117. Y. R. Shen, *The principles of nonlinear optics* (Wiley, New York, 1984).
118. A. A. Oraevsky, L. B. Da Silva, A. M. Rubenchik, M. D. Feit, M. E. Glinsky, M. D. Perry, B. M. Mammini, W. Small, and B. C. Stuart, "Plasma mediated ablation of biological tissue with nanosecond-to-femtosecond laser pulses: relative role of linear and nonlinear absorption," IEEE J Sel Top Quant **2**, 801-809 (1996).
119. W. B. Armstrong, J. A. Neev, L. B. Da Silva, A. M. Rubenchik, and B. C. Stuart, "Ultrashort pulse laser ossicular ablation and stapedotomy in cadaveric bone," Laser Surg Med **30**, 216-220 (2002).
120. J. Ilgner, M. Wehner, J. Lorenzen, M. Bovi, and M. Westhofen, "Morphological effects of nanosecond- and femto-second pulsed laser ablation of human middle ear ossicles," J Biomed Opt **11**, 014004 (2006).
121. B. M. Kim, M. D. Feit, A. M. Rubenchik, E. J. Joslin, P. M. Celliers, J. Eichler, and L. B. Da Silva, "Influence of pulse duration on ultrashort laser pulse ablation of biological tissues," J Biomed Opt **6**, 332-338 (2001).
122. B. M. Kim, M. D. Feit, A. M. Rubenchik, E. J. Joslin, J. Eichler, P. C. Stoller, and L. B. Da Silva, "Effects of high repetition rate and beam size on hard tissue damage due to subpicosecond laser pulses," Appl Phys Lett **76**, 4001-4003 (2000).
123. J. Kruger, W. Kautek, and H. Newesely, "Femtosecond-pulse laser ablation of dental hydroxyapatite and single-crystalline fluoroapatite," Appl Phys A **69**, S403-S407 (1999).
124. M. Braun, P. Gilch, and W. Zinth, *Ultrashort laser pulses in biology and medicine* (Springer-Verlag Berlin Heidelberg, 2008).
125. F. J. McClung and R. W. Hellwarth, "Giant optical pulsations from ruby," J Appl Phys **33**, 828-829 (1962).
126. L. E. Hargrove, R. L. Fork, and M. A. Pollack, "Locking of He-Ne aser modes induced by synchronous intracavity modulation," Appl Phys Lett **5**, 4-5 (1964).
127. C. V. Shank and E. P. Ippen, "Subpicosecond kilowatt pulses from a mode-locked cw dye laser," Appl Phys Lett **24**, 373-375 (1974).
128. J. C. Diels, E. Van Stryland, and G. Benedict, "Generation and measurement of 200 femtosecond optical pulses," Opt Commun **25**, 93-96 (1978).
129. R. L. Fork, C. H. B. Cruz, P. C. Becker, and C. V. Shank, "Compression of optical pulses to six femtoseconds by using cubic phase compensation," Opt Lett **12**, 483-485 (1987).
130. T. Brabec, C. Spielmann, P. F. Curley, and F. Krausz, "Kerr lens mode locking," Opt Lett **17**, 1292-1294 (1992).
131. D. E. Spence, P. N. Kean, and W. Sibbett, "60-fsec pulse generation from a self-mode-locked Ti:sapphire laser," Opt Lett **16**, 42-44 (1991).
132. U. Keller, "Ultrafast all-solid-state laser technology," Appl Phys B **58**, 347-363 (1994).
133. Y. L. Yao, H. Chen, and W. Zhang, "Time scale effects in laser material removal: a review," Int J Ad Manuf Technol **26**, 598-608 (2005).
134. W. S. Fann, R. Storz, H. W. K. Tom, and J. Bokor, "Direct measurement of nonequilibrium electron-energy distributions in subpicosecond laser-heated gold films," Phys Rev Lett **68**, 2834-2837 (1992).
135. M. H. Niemz, T. P. Hoppeler, T. Juhasz, and J. F. Bille, "Intrastromal ablations for refractive corneal surgery using picosecond infrared laser pulses," Lasers Light Ophthalmol **5**, 149-155 (1993).
136. A. Vogel, P. Schweiger, A. Frieser, M. N. Asiyo, and R. Birngruber, "Intraocular Nd:YAG laser surgery: light-tissue interaction, damage range, and the reduction of collateral effects," IEEE J Sel Top Quant **26**, 2240-2260 (1990).

137. Y. M. Lee, R. Y. Tu, A. C. Chiang, and Y. C. Huang, "Average-power mediated ultrafast laser osteotomy using a mode-locked Nd:YVO4 laser oscillator," J Biomed Opt **12**, 060505 (2007).
138. K. Ozono and M. Obara, "Tailored ablation processing of advanced biomedical hydroxyapatite," Appl Phys A **77**, 303-306 (2003).
139. M. Strassl, V. Weiger, D. Brodoceanu, F. Beer, A. Moritz, and E. Wintner, "Ultra-Short Pulse Laser Ablation of Biological Hard Tissues and Biocompatibles," J Laser Micro/Nanoengineering **3**, 30-40 (2008).
140. R. G. McCaughey, H. Sun, V. S. Rothholtz, T. Juhasz, and B. J. F. Wong, "Femtosecond laser ablation of the stapes," J Biomed Opt **14**, 024040 (2009).
141. Y. C. Lim, K. J. Altman, D. F. Farson, and K. M. Flores, "Micropillar fabrication on bovine cortical bone by direct-write femtosecond laser ablation," J Biomed Opt **14**, 064021 (2009).
142. M. Obara, K. Ozono, M. Kanai, H. Sekita, and P. A. Atanasov, "Femtosecond laser processing tailored for biomedical materials and laser power delivery through optical fibers," SPIE Proc Ser **4977**, 123-135 (2003).
143. H. Chen, B. Soom, S. Yaakobi, S. Uchida, and D. D. Meyerhofer, "Hot-electron characterization from *K*α measurements in high-contrast, *p*-polarized, picosecond laser-plasma interactions," Phys Rev Lett **70**, 3431-3434 (1993).
144. H. Devlin, M. Dickinson, A. J. Freemont, T. King, and R. Lloyd, "Healing of bone defects prepared using the erbium-YAG laser," Laser Med Sci **9**, 239-242 (1994).
145. J. R. Farley, S. L. Hall, D. Ilacas, C. Orcutt, B. E. Miller, C. S. Hill, and D. J. Baylink, "Quantification of skeletal alkaline-phosphatase in osteoporotic serum by wheat-germ-agglutinin precipitation, heat inactiviation, and a 2-site immunoradiometric assay," Clin Chem **40**, 1749-1756 (1994).
146. J. Pekar, "Multispectral bioluminescence tomography with x-ray CT spatial priors," (McMaster University Library, 2011).
147. D. C. Smith and A. F. Haught, "Energy-loss processes in optical-frequency gas breakdown," Phys Rev Lett **16**, 1085-1088 (1966).
148. A. Ben-Yakar and R. L. Byer, "Femtosecond laser ablation properties of borosilicate glass," J Appl Phys **96**, 5316-5323 (2004).
149. S. R. Farrar, D. C. Attril, M. R. Dickenson, T. A. King, and A. S. Blinkhorn, "Etch rate and spectroscopic ablation studies of Er:YAG laser-irradiated dentine," Appl Opt **36**, 5641-5646 (1997).
150. B. Majaron and M. Lukac, "Calculation of crater shape in pulsed laser ablation of hard tissues," Laser Surg Med **24**, 55-60 (1999).
151. H. W. Kang, H. Lee, S. C. Chen, and A. J. Welch, "Enhancement of bovine bone ablation assisted by a transparent liquid layer on a target surface," IEEE J Sel Top Quant **42**, 633-642 (2006).
152. J. Serbin, T. Bauer, C. Fallnich, A. Kasenbacher, and W. H. Arnold, "Femtosecond lasers as novel tools in dental surgery," Appl Surf Sci **197**, 737-740 (2002).
153. J. M. Liu, "Simple technique for measurements of pulsed Gaussian-beam spot sizes," Opt Lett **7**, 196-198 (1982).
154. X. Liu, D. Du, and G. Mourou, "Laser ablation and micromachining with ultrashort laser pulses," IEEE J Sel Top Quant **33**, 1706-1716 (1997).
155. D. Ashkenasi, A. Rosenfeld, H. Varel, M. Wahmer, and E. E. B. Campbell, "Laser processing of sapphire with picosecond and sub-picosecond pulses," Appl Surf Sci **120**, 65-80 (1997).
156. P. T. Mannion, J. Magee, E. Coyne, G. M. O'Connor, and T. J. Glynn, "The effect of damage accumulation behavior on ablation thresholds and damage morphology in ultrashort laser micro-machining of common metals in air," Appl Surf Sci **233**, 275-287 (2004).
157. J. Byskov-Neilsen and J.-M. Savolainen, "Ultra-short pulse laser ablation of metals: threshold fluence, incubation coefficient and ablation rates," Appl Phys A **101**, 97-101 (2010).
158. J. Bonse, J. M. Wrobel, J. Kruger, and W. Kautek, "Ultrashort-pulse laser ablation of indium phosphide in air," Appl Phys A **72**, 89-94 (2001).
159. D. Gomez and I. Goenaga, "On the incubation effet on two thermoplastics when irradiated with ultrashort laser pulses: broadening effects when machining microchannels," Appl Surf Sci **253**, 2230-2236 (2006).
160. Y. Jee, M. F. Becker, and R. M. Walser, "Laser-induced damage on single-crystal metal surfaces," J Opt Soc Am B **5**, 648-659 (1988).
161. C. S. Lee, N. Koumvakalis, and M. Bass, "Spot-size dependence of laser-induced damage to diamond-turned Cu mirrors," Appl Phys Lett **41**, 625-627 (1982).

162. A. Rosenfeld, M. Lorenz, and D. Ashkenasi, "Ultrashort-laser-pulse damage threshold of transparent materials and the role of incubation," Appl Phys A **69**, S373-S376 (1999).
163. A. K. Murray and M. R. Dickenson, "Tissue ablation-rate measurements with a long-pulsed, fibre-deliverable 308 nm excimer laser," Lasers Med Sci **19**, 127-138 (2004).
164. J. Aerssens, S. Boonen, G. Lowet, and J. Dequeker, "Interspecies differences in bone composition, density, and quality: potential implications for in vivo bone research," Endocrinology **139**, 663-670 (1998).
165. M. Stafe, C. Negutu, and I. M. Popescu, "Combined experimental and theoretical investigation of multiple-nanosecond laser ablation of metals," J Optoelectron Adv M **8**, 1180-1186 (2006).
166. I. Vladoiu, M. Stafe, C. Negutu, and I. M. Popescu, "Influence of the pulse number and fluence of a nanosecond laser on the ablation rate of metals, semiconductors and dielectrics," Eur Phys J Apple Phys **47**, 30702 (2009).
167. M. Dutra-Correa, G. Nicolodelli, J. R. Rodrigues, C. Kurachi, and V. S. Bagnato, "Femtosecond laser ablation on dental hard tissues - analysis of ablated profile near an interface using local effective intensity," Laser Phys **21**, 965-971 (2011).
168. J. Zhang, Y. Wang, P. Cheng, and Y. L. Yao, "Effect of pulsing parameters on laser ablative cleaning of copper oxides," J Appl Phys **99**, 064902 (2006).
169. E. W. van Stryland, M. J. Soileau, A. L. Smirl, and W. E. Williams, "Pulse-width and focal-volume dependence of laser-induced breakdown," Phys Rev **B 23**, 2144-2151 (1981).
170. N. Bloembergen, "Laser-induced electric breakdown in solids," IEEE J Qu Electron **QE-10**, 375-386 (1974).
171. B. Le Drogoff, J. Margot, F. Vidal, S. Laville, M. Chaker, M. Sabsabi, T. Johnston, and O. Barthelemy, "Influence of the laser pulse duration on laser-produced plasma properties," Plasma Sources Sci Technol **13**, 223-230 (2004).
172. S. M. Eaton, H. Zhang, and P. R. Herman, "Heat accumulation effects in femtosecond laser-written waveguides with variable repetition rate," Opt Express **13**, 4708-4716 (2005).
173. D. N. Papadopoulos, F. Druon, J. Boudelle, I. Martial, M. Hanna, P. Georges, P. O. Petit, P. Goldner, and B. Viana, "Low-repetition-rate femtosecond operation in extended-cavity mode-locked Yb:CALGO laser," Opt Lett **34**, 196-198 (2009).
174. Newport, "Gaussian beam optics tutorial" (Newport Corporation, 2011), retrieved http://www.newport.com/servicesupport/Tutorials/default.aspx?id=112.
175. M. Di Silvestre, P. Parisini, F. Lolli, and G. Bakaloudis, "Complications of thoracic pedicle screws in scoliosis treatment," Spine (Phila Pa 1976) **32**, 1655-1661 (2007).
176. R. J. Minns, "Surgical instrument design for the accurate cutting of bone for implant fixation," Clin Mater **10**, 207-212 (1992).
177. Y. P. Raizer, "Breakdown and heating of gases under the infuence of a laser beam," Sov Phys Usp **8**, 650-673 (1966).
178. F. Docchio, P. Regondi, M. R. C. Capon, and J. Mellerio, "Study of the temporal and spatial dynamics of plasmas induced in liquids by nanosecond Nd:YAG laser pulses. 1: Analysis of the plasma starting times," J Appl Opt **27**, 3661-3668 (1988).
179. A. Michalowski, D. Walter, F. Dausinger, and T. Graf, "Melt dynamics and hole formation during drilling with ultrashort pulses," J Laser Micro/Nanoengineering **3**, 211-215 (2008).
180. M. Kraus, S. Collmer, S. Sommer, and F. Dausinger, "Microdrilling in steel with frequency-doubled ultrashort pulsed laser radiation," J Laser Micro/Nanoengineering **3**, 129-134 (2008).
181. J. Kaspar, A. Luft, S. Nolte, M. Will, and E. Beyer, "Laser helical drilling of silicon wafers with ns to fs pulses: Scanning electron microscopy and transmission electron microscopy characterization of drilled through-holes," J. Laser Appl. **18**, 85-92 (2006).
182. M. M. Ivanenko, G. Eyrich, E. Bruder, and P. Hering, "In vitro incision of bone tissue with a Q-switch CO2 laser. Histological examination," Lasers Life Sci **9**, 171-179 (2000).
183. G. Olivie, D. Giguere, F. Vidal, T. Ozaki, J. C. Kieffer, O. Nada, and I. Brunette, "Wavelength dependence of femtosecond laser ablation threshold of corneal stroma," Opt Express **16**, 4121-4129 (2008).

9. APPENDIX

Operating the micro-CT:

Micro-CT alignment:

The micro-CT alignment procedure is done to obtain the source-to-detector distance (SDD) and source-to-object distance (SOD). The alignment is performed with the ball-bearing apparatus inserted in the centre of the rotation stage. The detector should be adjusted to about 2” from the stage. Turn on the x-ray detector a few hours prior to scanning to allow it to warm up. This is done using the power bar located at the back of the experimental bench.

With the alignment apparatus in place, open ‘C:\labview_code\CT_alignment.vi’ in Labview® 6 using the micro-CT workstation. Turn the x-ray source on using the safety key. Set the tube voltage and current to 40 kV and 0.150 mA, respectively, using the Labview interface. Input a specified directory to save the alignment images. Click ‘Run’.

Open and run ‘C:\matlab\CT_align_easy’ in Matlab. Open all 12 images obtained. For each image, click on each ball bearing (top then bottom) and press enter. After the software has fit the data with an ellipse, click ‘Find Detector Yaw’ and ‘Find ellipse parameters’ to obtain the necessary alignment data. Save this data into a text file.

Sample imaging:

Attach the bone sample to the water-filled plastic canister using melted paraffin wax and hot-glue the canister to the centre of the scanning stage. Use ‘Single x-ray exposure.vi’ to experiment with slightly different tube voltages and currents and obtain the desired contrast. Set the ‘Pixel number’ drag bar on the right to its maximum value of 4095.

Using ‘Stationary_CBCT_scan.vi’, input the voltage and current values previously chosen and select a rotation speed of 1° per second. Click ‘Save images’ and specify a folder in which the raw data will be saved in. Click ‘Run’. Scanning typically takes ~10 minutes.

Gain correction:

After completing the sample scanning, remove it from the stage and run ‘Gain_correction.vi’. Move the pixels bar to maximum (4095) and specify the name of the folder for the corrections to be saved. Add 0’s to the boxes under Gain #2, Gain #3 and Gain #4. Under Gain #1, input the tube current used divided by 2 (in units of μA) (i.e. input 80 if 0.160 mA was used during scanning). Click ‘Set’ to update filenames. Set the tube voltage, frame-time used during the scanning process and change the number of projections to ten. Click the ‘Save images’ box and run.

Image analysis:

CT image conversion:

Run 'CBCT_image_conversion_utility.m' in Matlab (found in the folder 'C:\Matlabcode\CT_programs\CBCT_conversion'). Open all offset images by highlighting all ten. Open all ten Gain## images (## being the current/2 value used during the gain correction procedure). Save the data as dBL and click 'Cobra'. Run the image conversion process.

Image reconstruction:

Open Cobra Exxim® reconstruction software on the micro-CT workstation. Copy a previously used Source Data file and alter the appropriate parameters for the current job. Parameters that will need to be changed are:

- Source of data
- Destination folder
- SOD & SDD (obtained from alignment procedure)
- u-offset (*u*o) & v-offset (*v*o) (obtained from alignment procedure)
    - Note that the inputted *u*o and *v*o will need to be taken as the difference between the *u*o and *v*o obtained previously and 512.5 and 1024.5 pixels (centre of the detector), respectively.

The rest of the parameters can be adjusted to if needed. The cube pitch and size will alter the reconstructed resolution. Pitch is the pixel size in mm. Cube origin is the 3D central location at which reconstruction occurs. After adjusted, click “Reconstruct” to obtain images in .slice form.

Surface rendering:

After reconstructed, transfer the images via USB to a workstation with both ImageJ and 3D Slicer. Use ImageJ to convert the 384 images into an image stack and crop as necessary to reduce the processing time during surface rendering. Save the cropped stack.

In 3D Slicer, open the previous stack as a ‘volume’. After loading, the original stack should appear as a sequence of three stacks that can be scanned in the sagittal, coronal and trans-axial directions. Open the ‘Volume rendering’ tab and select the bone stack under the ‘Source data’ drop-down. After a few moments of processing, the rendered stack will appear. Use the thresholding feature to reduce the grey-scale in the background and leave the bone sample.